THE ANALYSIS OF ULTRASONIC IMAGING TECHNIQUES OF MULTILAYERED REVERBERANT TARGETS

BY

DANIEL TELL NAGLE

Submitted in partial fulfillment of the
requirements of the degree of
Master of Science in Electrical Engineering
in the School of Advanced Studies of
Illinois Institute of Technology

Approved _____
Advisor

Chicago, Illinois
December, 1987

ACKNOWLEDGEMENT

The author wishes to express his sincere gratitude and appreciation to his major professor, Dr. J. Saniie, for his guidence and assistance through all phases of this research. The author also would like to thank Dr. Dreizen and Dr. Atkin for serving on his thesis committee.

The financial support from the Electric Power Research Institute under grants RP 2687-3 and RP 2673-5 through Illinois Institute of Technology is greatly appreciated.

The author expresses his special appreciation to Kevin and Sharon Donohue for their assistance with illustrations, proof reading, etc. The author would like to thank most of all his aunt, Lorraine Nagle for her continual encouragment and support during his graduate studies.

D.T.N.

TABLE OF CONTENTS

LIST OF FIGURES

ABSTRACT

The ultrasonic imaging, using pulse-echo scanning mode, of a multilayered target results in reverberations which complicate the direct characterization of each layer. Through earlier investigations, a theoretical model has been developed to analytically describe the reverberation phenomenon caused by the presence of each layer. This research focusses on the practical problem of imaging tube/support plate structures used in nuclear power plant steam generators. The nondestructive evaluation of these structures is an important problem since the presence of corrosion and flaws can impede normal plant operations. The imaging of tube/support plate structures is difficult, if not impossible, because the experimental measurements have far less resolution and lower signal to noise ratio (SNR) than expected theoretically. The degradation of experimental measurements can be attributed to the existence of corrosion, inhomogeneities in the layers, suboptimal reflecting surfaces, and/or inherent noise in the measurement system. The proper selection of measurement systems and post-measurement signal processing techniques, analog and/or digital, can provide enhancement in the resolution of the information-bearing backscattered signal and, consequently, improve the classification of deteriorated multilayered structure. Included in this paper is the analysis of the different measurement and processing techniques and the evaluation of experimental results to determine the optimal classification procedure in the imaging of multilayered targets.

CHAPTER I

INTRODUCTION

Ultrasonic Imaging

Ultrasonic pulse-echo imaging provides characterization of changes in the homogeneity of a substance which can indicate boundaries between two different materials or internal discontinuities within the same material. In the pulse-echo mode, a short pulse of ultrasonic energy is transmitted into the target and then the returning echoes are observed. The time of flight of the reflected echoes indicates the depth of the reflector and the amplitude provides information corresponding to characteristics of the material (in terms of the material's acoustical impedances) or information depicting the size and orientation of the reflector. In the ultrasonic examination of highly reverberant multilayered structures, the received signal is comprised of multiple echoes which complicate the characterization of the layers of the target. In the nondestructive evaluation of materials, the problem of reverberating patterns arises frequently. In fact, some structures by their very nature are so reverberant that the reverberating echoes comprise the entire signal. Reverberating patterns can occur in the measurements of thin planar defects in metal, in lamination of composite bonds, in gap thickness measurements of adhesively-bonded metal systems, oil film measurements, fatigue crack analysis, etc. [Cha80,Kra75,Lee71,Ros74].

The pulse-echo imaging of reverberant targets consisting of an isolated single layer has been analyzed to some extent in the past [Lee71,Ros74,Maz86]. Reverberations were studied for the case in which the incident sound pulse is of approximately the same or of a longer duration as the traveling time within the thin layer. It has been found that a moderately accurate thickness measurement may be obtained by examining the ratio of the first pronounced peak to the following peak of the backscattered signal [Lee71]. Although this pattern recognition technique is useful for measuring the thickness of a single thin film, it cannot be

extended to a structure composed of multiple layers in which each layer causes reverberations.

The mathematical analysis of continuous wave propagation in layered media is known explicitly [Bre80]. However, the use of continuous excitation to characterize a multiple layered structure requires that the wave must be of a long enough duration to reach a steady state value. This constraint introduces range ambiguity in the imaging of the target, and the steady state value represents only the overall characteristics of the multilayered structure. Consequently, the continuous mode of testing lacks the capability of displaying local information and the characterization of each subsequent layer becomes virtually impossible.

Of particular interest to present research is characterizing the multilayered reverberant environment that exists in the detection of corrosion or volatile changes in the steam generator tubing system used in nuclear power plants. Steam generators currently in use contain inconel tubing that fits loosely through holes drilled in a carbon steel support structure, as can be seen in Figure 1-1a. Nonprotective magnetite can accumulate on the inner surface of the support plate holes, and, if allowed to continued unchecked, will fill the gap and eventually dent or fracture the tube wall. Therefore, the periodic inspection of the tube/support structure is needed to assess the degree of corrosion protruding into the water gap and possible deterioration in the tube wall. In examining such structures, it is noted that a variety of reverberant patterns can be expected due to the geometry of the layer or, more importantly, the random nature of corrosion growth. These patterns can be recognized and classified for the evaluation of tube/support structures. Through earlier studies [San81,San82], a theoretical model describing the reverberation phenomenon for multilayered structures has been developed which provides critical insight into the characterization of boundaries of multilayered structures.

The tube/support structure is inspected by transmitting an ultrasonic pulse through the tube wall, as shown in Figure 1-1b, which results in two dominant sets of reverberating echoes corresponding to the tube wall (tube echoes) and the support plate (support plate echoes). These sets of multiple echoes must be decomposed and separated in order to evaluate the tube/support structure effectively.

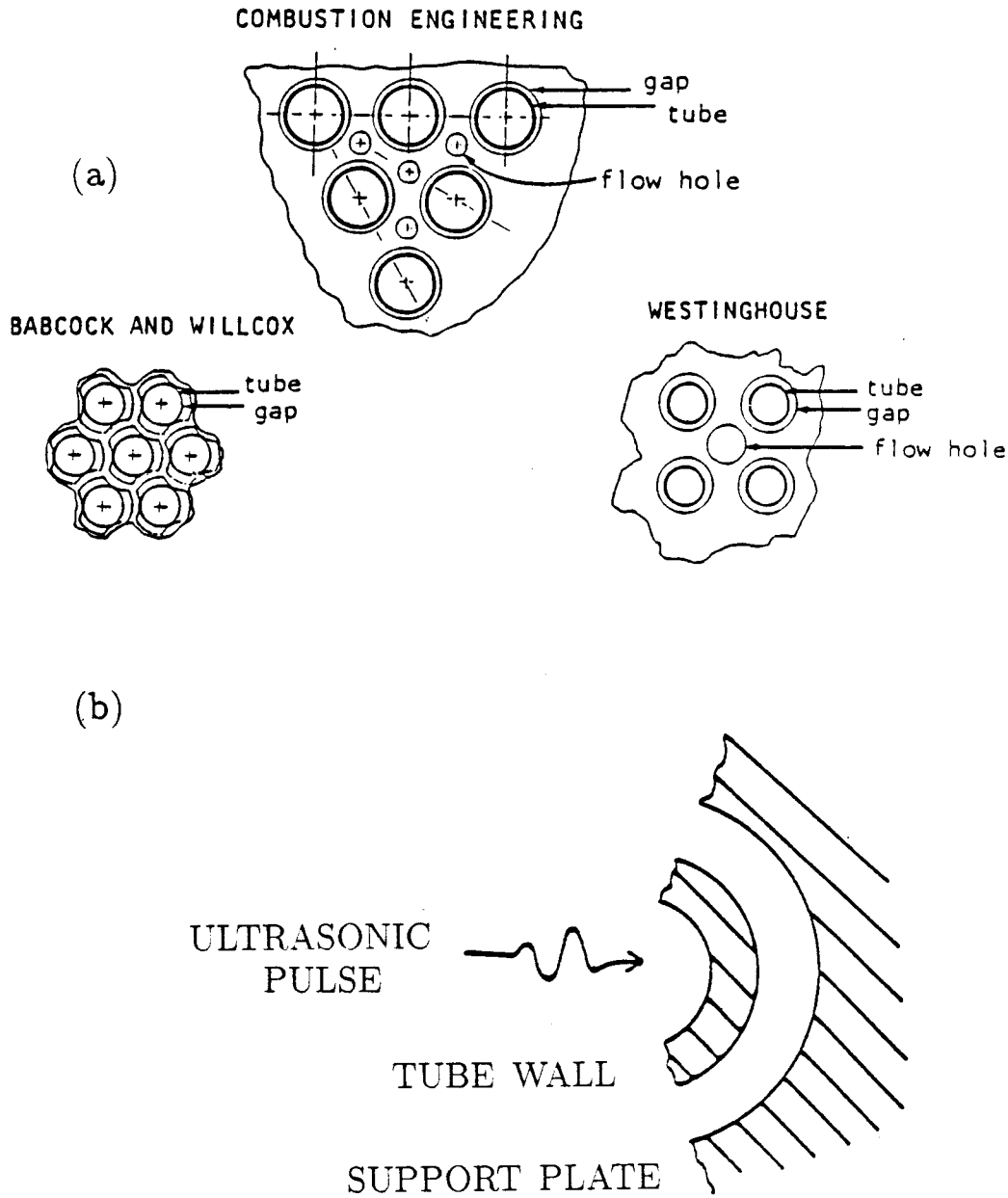

Figure 1-1. Typical configurations of the tube/support structure

This thesis concentrates on the analytic modeling of these reverberant echoes, and determining the optimal measurement environment and correspondingly effective signal processing techniques, analog and digital, to enhance resolution of information-bearing backscattered echoes.

NDE of Steam Generator Tube/Support Structures

The nondestructive testing of nuclear power plant steam generator tubing is very important in terms of the safe and economical operation of the plant. Nondestructive testing can identify corrosion and flaws early on, before they become critical to the plant's operation. The denting or leaking of steam generator tubing will necessitate the shutting down of the plant until the tubing can be repaired. This repair time could be costly, given that a medium size nuclear power plant earns approximately a half a million dollars each day [Dav78]. There are chemical treatments to counteract the growth of corrosion in the tube/support structure, such as amonia or hydrazine [Eco84]; however, these techniques are only useful when corrosion is detected early on in the corrosion process. Thus, there has been much attention given to this problem of corrosion classification and evaluation.

As the steel support plate corrodes, nonprotective magnetite protrudes from the surface of the support plate due to the fact that steel increases almost twice in volume after the corrosion process has occurred [deS84]. If left unchecked, the corrosion will fill up the gap, eventually denting or fracturing the tube walls. Therefore, periodic inspection can be valuable in characterizing corrosion and can also be used in evaluating the effectiveness of chemical treatments used to control or reduce corrosion.

The two most popular measurement techniques of corrosion in steam generator tube/support structures are eddy-current measurements and ultrasonic measurements. The study of eddy current provides sensitivity to changes in impedance of the inconel tube wall in the vicinity of the support plate. Corrosion can then be

detected, although the degree and amount of corrosion can not be accurately determined through present studies [Jon83]. The accuracy of measuring the depth of corrosion using eddy current measurements has been highly limited and ineffective.

Unlike eddy-current testing, there is more inherent information provided with pulse-echo scanning due to the ability to characterize the position and material from the reflected echoes. This research analyzes the problem of evaluating denting and corrosion in steam generator tube/support plate structures by using ultrasonic imaging techniques. Ultrasonic testing is a popular method of examining these structures due to its nondestructive nature and its practicality in terms of implementation and cost.

Since the growth and nature of corrosion itself has some random properties, it can not be readily characterized. The best indication of corrosion in the ultrasonic measurement of tube/support structures is the identification of altered or corroded boundaries in the target. Since the corrosion stems from the support plate, the imaging of the support plate is necessary for early detection. Thus, decomposition of the echoes backscattered from the support plate and the tube wall are of great value in the detection of corrosion and denting.

Summary of Chapters II-VII

Chapter II contains the theoretical derivation of a model of reverberant echoes created through the ultrasonic examination of a multilayered target. The model [San81] decomposes the signal by breaking the signal up into sets of multiple echoes that are related to the different physical boundaries in the layered target. Thus, information about the status of all the boundaries can be inferred from the corresponding set of multiple echoes. It will be shown in Chapter II that the reflected signal from the steam generator tube/support structure is composed of two dominant sets of multiple echoes, in which one corresponds to the tube wall characteristics (referred to as class 'a' echoes) and the other corresponds to the support plate characteristics (referred to as class 'b' echoes). A complete mathematical derivation and analytical evaluation of the model is presented.

Chapter III develops the criteria for an optimal measurement system, which consists of a transducer and reflector apparatus (which may or may not provide focusing). In order to achieve higher resolution of the multiple echoes corresponding to the support plate, the transducer frequency must be increased at the expense of increased signal-to-noise ratio due to the attenuation characteristics of the medium. This can be partially compensated for by improving the focusing of the beam on the target (tube wall). Consequently, the energy per unit area entering the target will increase and will improve the signal-to-noise ratio of the system as a whole. The object of the chapter is to analyze several different focusing schemes and find the optimal measuring system for imaging of tube/support structures.

Oblique angle scanning is analytically evaluated and implemented experimentally in Chapter IV. The process of oblique angle scanning utilizes the geometry of the tube wall to reflect the 'a' echoes (tube echoes) away from the detectable beam field of the transducer. The 'b' echoes (support plate echoes) are unaltered by this change in the orientation of the tube wall as long as the support plate is near-normal to the beam path. In general, using oblique angle scanning will complicate the reverberent echoes in the tube wall due to mode conversion, where there are two transmitted waves, referred to as longitudinal and shear waves, produced at the tube wall boundaries. Computer simulation is used to characterize the different types of reflections at each boundary. This simulation can aid in finding the optimal reflection angle and corresponding transmission coefficients for imaging of 'b' echoes. The goal of Chapter IV is to provide automatic tube echo rejection, with the optimal angle being as small as possible, while minimizing the interference caused by mode conversion.

The digital echo cancellation is presented in Chapter V. Digital echo cancellation involves using a reference signal, consisting of only 'a' echoes, matched to the measure signal, containing 'a' and 'b' echoes, which when subtracted results in improved visibility of 'b' echoes. The difficulty in implementing this process lies in matching the 'a' echoes of both signals in terms of shape and timing. Proper matching can be obtained with the use of digital signal processing techniques. However, additional computational constraints may cause the system to be impractical for routine testing or real time applications. The goal of the chapter is

to analyze different processing techniques and demonstrate their effectiveness with experimental results. Analog echo cancellation is another possible alternative for resolving 'b' echoes which is also described in Chapter V. This process involves the subtraction of the reference signal and measured tube/support signal in real time. Analog echo cancellation technique requires two ultrasonic measuring systems that are very similar in terms of components and the systems' overall impulse response. Variations in the two systems will give rise to sets of 'a' echoes that are out of sync or not of the same signal intensity or shape. These variations can be reduced using adjustable delays and impedance matching transducer dampeners to make the systems more symmetrical. These controls can either be adjusted manually or through automatic adaptive matching techniques. The control used for feedback in the adaptive technique is the output power of the system which, when minimized, maximizes the cancellation of the 'a' echoes.

Chapter VI presents experimental results and techniques of identifying corrosion. Experimental procedure involves vertical and radial scanning of the tube wall. After extensive experimental measurements, many characteristics of signal were correlated with the different physical aspects of corrosion. Using experimental results, a hierarchical classification procedure is presented. This classification procedure also employs statistical pattern recognition techniques to account for the random parameters that exist in the tube/support structure. Thus, this classification procedure will give the best results, in a probablistic sense, of the status of the tube/support structure.

Chapter VII contains conclusions about experimental results and discussion of promising techniques of image classification for continued research.

CHAPTER II

MODELING OF REVERBERANT ECHOES

Single Thin Layer

For the sake of developing a theoretical base for analyzing the backscattered echoes from a highly reverberant discrete structure, we will first focus our attention on the simple case of examining a single thin layer. Illustrated in Figure 2-1 is an outline of the reverberation process which shows the normal incident beam and the corresponding transmitted and reflected beams as a function of time, where Region I, Region II, and Region III are defined by their density, ρ_i, and the velocity of sound in that media, denoted by v_i. These two quantities define the acoustic impedance, Z_i, of a given region i:

$$Z_i = \frac{1}{\rho_i v_i} \qquad (2-1)$$

The incident ultrasonic beam impinging the thin layer is partially reflected and transmitted at each boundary, as seen in Figure 2-1. Using the characteristic impedances, the reflection and transmission coefficients of each boundary can be calculated using the following equations:

$$\alpha_{ij} = \frac{Z_i - Z_j}{Z_i + Z_j} \quad ; \quad \beta_{ij} = \frac{2Z_i}{Z_i + Z_j} \qquad (2-2)$$

where α_{ij} and β_{ij} are the reflection and transmission coefficients of adjacent regions i and j, respectively.

In the development of this model, the incident beam is assumed to be normal for the sake of mathematical simplicity. Using this assumption, it can be inferred that all reflections and transmissions will also be normal to the incident boundaries of the target due to Snell's Law, which states:

$$\frac{sin(\theta)}{C} = \frac{sin(\phi)}{B} \qquad (2-3)$$

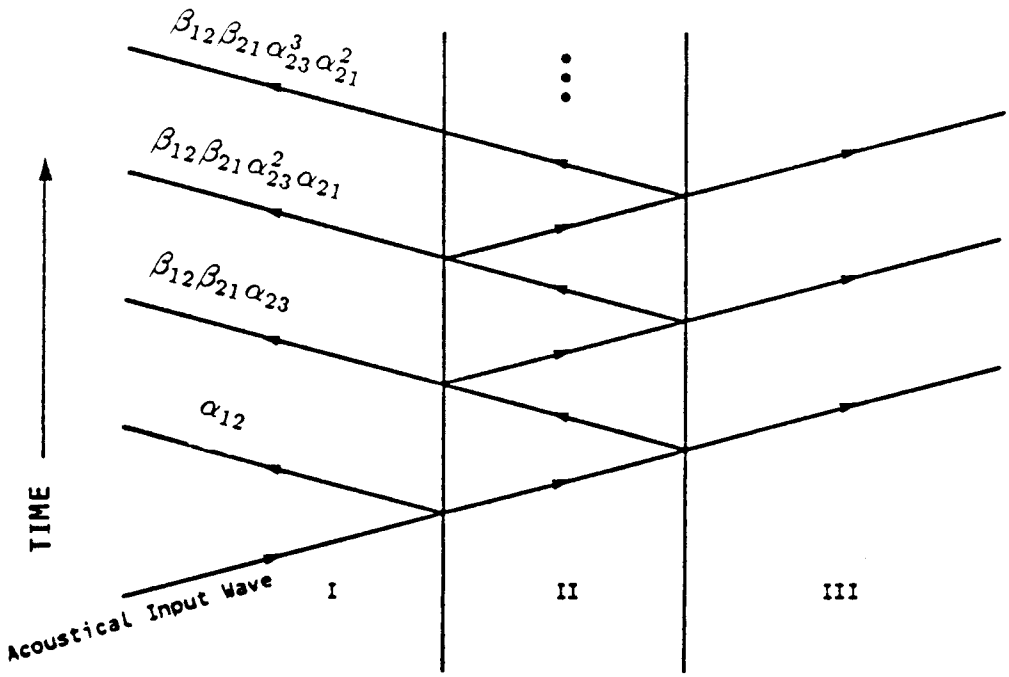

Figure 2-1. Reverberation path in a single thin layer

where θ is the incident angle (measured with respect to the norm), γ is the angle of the transmitted beam, and C and B are the velocities of the echoes in their respective mediums. When θ equals zero, the transmission angle, γ, will also be zero, thus supporting the statement above. The case in which the incident angle is not normal is discussed in Chapter IV.

The successive reflections and transmissions within a single layer result in multiple received echoes which can be modeled as

$$r(t) = \alpha_{12}u(t) + \sum_{k=1}^{\infty} a_k u(t - 2kT_2) \qquad (2-4)$$

where

$$a_k = \beta_{12}\beta_{21}{\alpha_{23}}^k{\alpha_{21}}^{k-1} \qquad (2-5)$$

$r(t)$ is the received signal, T_i is the time it takes the echo to travel the ith region, and $u(t)$ is the impulse response of the measuring system. The received signal can be thought of as a set of multiple echoes spaced evenly apart in time, separated by a time $2T_2$. The effect of grain noise and system noise are considered negligible in this derivation and are not included in the above equation.

The reverberant pattern can be seen from the examination of a thin steel plate shown in Figure 2-2. From the measured signal, the thickness of the plate can be determined. The time between echoes is $2T_2$, and then can be used to calculate the thickness of region i, d_i, since,

$$d_i = v_i T_i \qquad (2-6)$$

where v_i is the velocity of sound (longitudinal) in the ith region. In addition, the amplitude of sequential echoes decreases by a factor $\alpha_{23}\alpha_{21}$. This phenomenon, for the case where $\alpha_{23} = \alpha_{21} = \alpha$, is demonstrated for different reflection coefficients α in Figure 2-3. The least reverberant case is shown in Graph I, where most of the energy arrives within the first few echoes. This is due to the low impedance of the thin layer which allows much energy to escape within the initial reverberations.

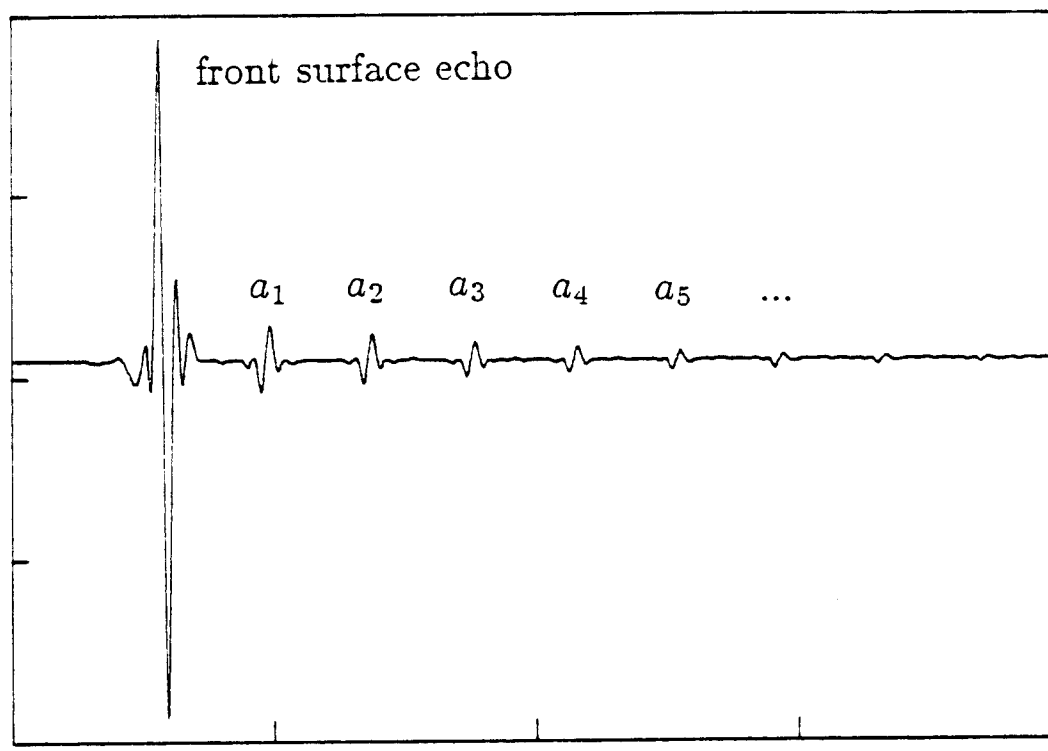

Figure 2-2. The backscattered signal from an A-scan of a thin steel layer

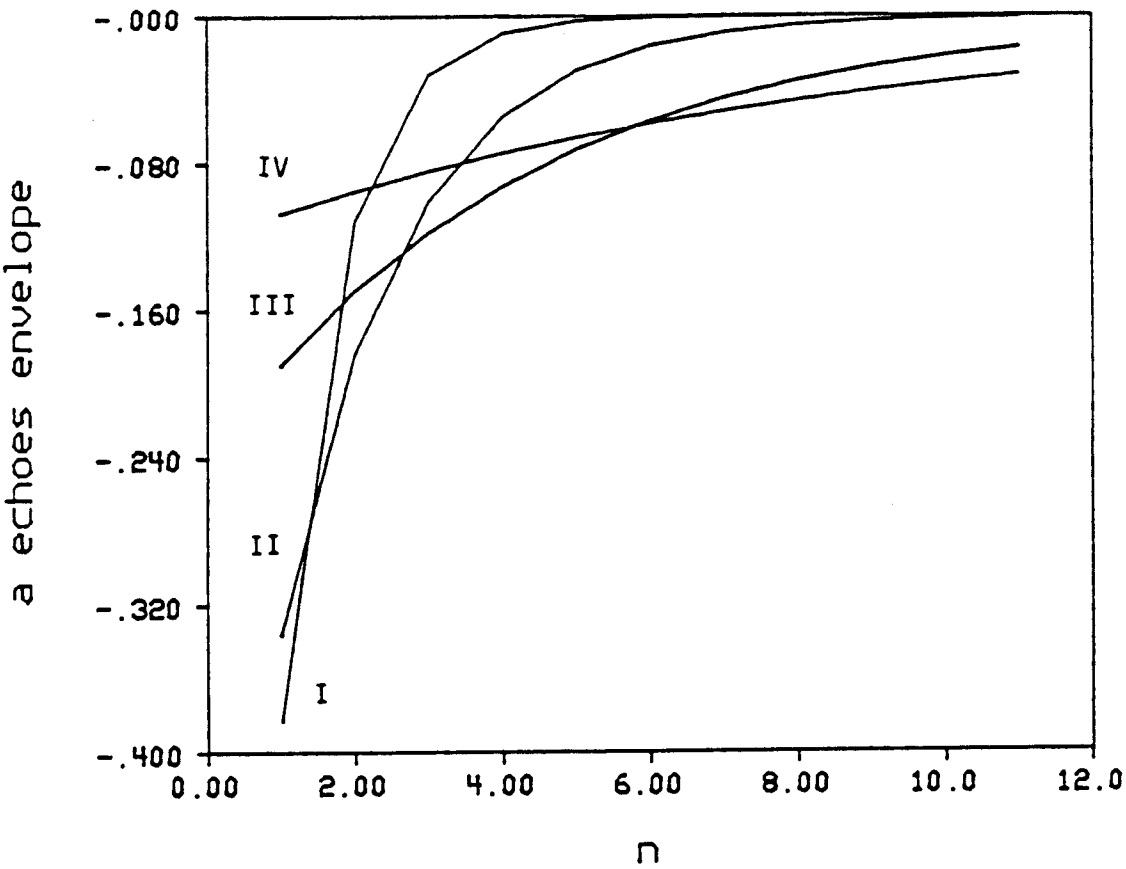

Figure 2-3. Envelope of the reverberation echoes from a thin layer for different values of α: I) $\alpha = 0.54$. II) $\alpha = 0.74$. III) $\alpha = 0.88$. and IV) $\alpha = 0.94$

Although as the thin layer becomes more mismatched with its surroundings, as shown progressively in Graphs II-IV, later echoes increase in energy, resulting in prolonged reverberations. Increasing in acoustical mismatch of the interface of the layer makes the signal more reverberant, since less energy is allowed to leak out of the layer at each reverberation. The inconel tube of the tube/support structure can be characterized by the highly reverberant case shown in Graph IV, where a drop of 20dB can be expected from the first reverberation in comparison to the first received echo. Generally, highly reverberant layers let very little energy penetrate and, therefore, make imaging through the layer more difficult. The envelopes of reverberant echoes provide information that leads to estimates of α_{ij} or β_{ij} and results in estimates of Z_i and Z_j which can be used to evaluate the layer.

Multilayered Target

With multilayered structures, the recognition of reverberant patterns is more complex due to multiple interfering echoes produced at each interface. The tube/support structure can be represented by a model shown in Figure 2-4, where Region I is inside the tube, Region II is the inconel 600 tube wall, Region III is the water gap, and Region IV is the steel support plate. In the pulse-echo examination of the tube/support structure, the received signal is comprised of multiple echoes detected after traveling k times in Region II and l times in Region III:

$$r(t) = \sum_{k=0}^{\infty} \sum_{l=0}^{\infty} \gamma_{kl} u(t - 2kT_2 - 2lT_3) \qquad (2-7)$$

where the term γ_{kl} is the received echo amplitude related to the reflection coefficients, α_{ij}, or the transmission coefficient, β_{ij}. (Note: i and j indicate which regions constitute the interface.) The term γ_{kl} can not be expressed explicitly in terms of α_{ij}, l, and k, since there are many echoes of different intensities and paths traversed which have equivalent travel times. These echoes are then summed together to form a composite amplitude, γ_{kl}. A simple example of this for the case where $k = 2$ and $l = 2$ is shown in Figure 2-5. in which there are three unique

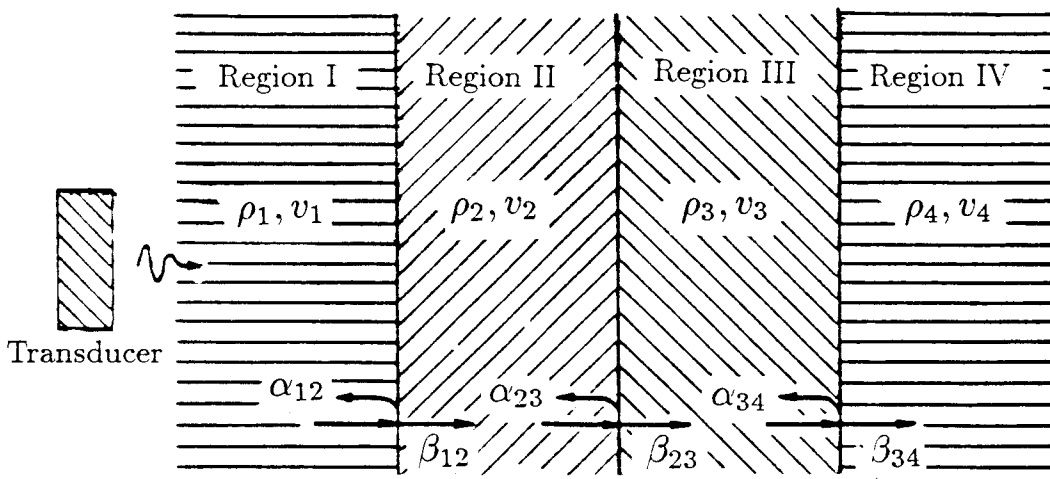

Figure 2-4. Multilayer model consisting of four regions

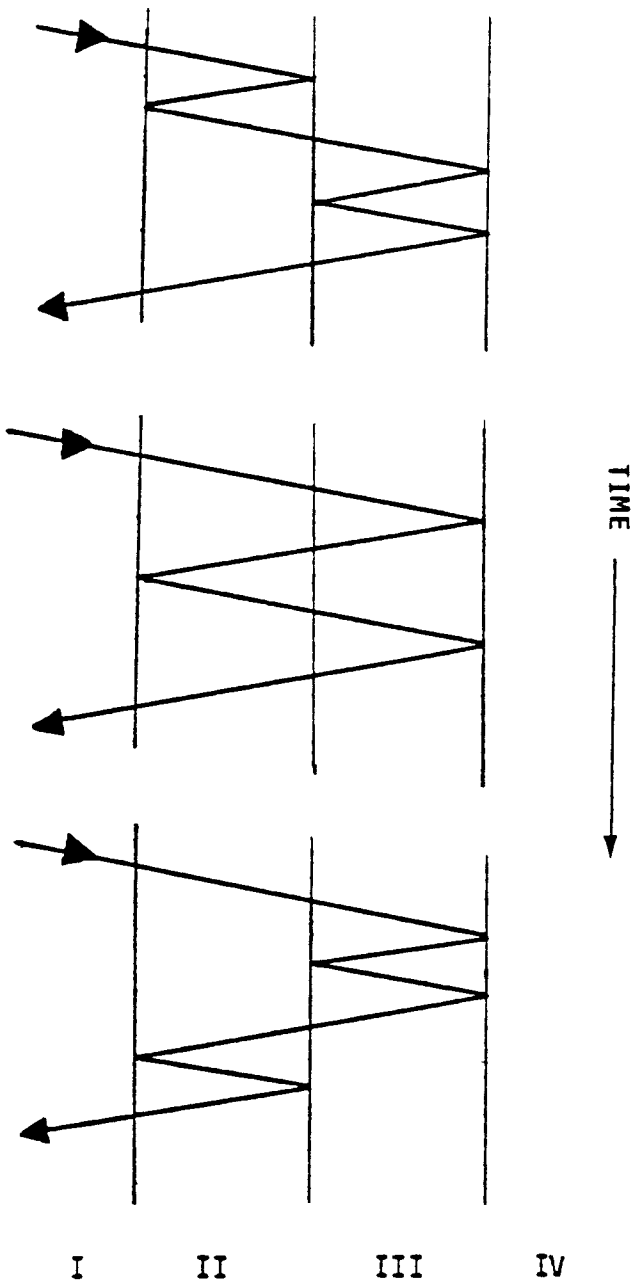

Figure 2-5. Variations of waves paths with equivalent traveling time for the case where $k = 2$ and $l = 2$

paths that comprise γ_{22}. For large values of k and l, the number of paths will increase tremendously.

Through extensive experimentation and computer simulation, an appropriate identification and classification technique was developed which allowed characterization of the layered structure of those detected echoes of significant intensities [San81]. As a result of classification, the generalized model for the received echoes given in Equation 2-7 can be presented differently.

$$r(t) = \alpha_{12}u(t) + \sum_{k=1}^{\infty} a_k u(t - 2kT_2) + \sum_{k=1}^{\infty} b_k u(t - 2T_3 - 2kT_2) +$$

$$\sum_{k=1}^{\infty} c_k u(t - 4T_3 - 2kT_2) + \sum_{k=1}^{\infty} d_k u(t - 6T_3 - 2kT_2) + \ldots\ldots \qquad (2-8)$$

where a_k is the amplitude of the class 'a' echoes that reverberate in Region II only; b_k is the amplitude of the class 'b' echoes that reverberate continually in Region II, and once in Region III; c_k is the amplitude of the class 'c' echoes that reverberate continually in Region II, and twice in Region III; d_k is the amplitude of the 'd' echoes which reverberate continually in Region II and three times in Region III; etc.

The amplitudes of these classes of echoes are given [San81]

$$a_k = (\frac{\beta_{12}\beta_{21}}{\alpha_{21}}){A_0}^k; \quad for \quad k \geq 1 \qquad (2\text{-}9)$$

$$b_k = k(\frac{\beta_{12}\beta_{21}}{\alpha_{21}})A_1{A_0}^{k-1}; \quad for \quad k \geq 1 \qquad (2\text{-}10)$$

$$c_1 = \frac{\beta_{12}\beta_{21}}{\alpha_{21}}A_2 \qquad (2\text{-}11)$$

$$c_k = (\frac{\beta_{12}\beta_{21}}{\alpha_{21}})k[A_2{A_0}^{k-1} + \frac{k-1}{2}{A_1}^2{A_0}^{k-2}] \; ; \; for \quad k > 1 \qquad (2\text{-}12)$$

$$d_1 = (\frac{\beta_{12}\beta_{21}}{\alpha_{21}})A_3 \qquad (2\text{-}13)$$

$$d_2 = (\frac{\beta_{12}\beta_{21}}{\alpha_{21}})[A_3A_0 + A_2A_1] \qquad (2\text{-}14)$$

$$d_k = (\frac{\beta_{12}\beta_{21}}{\alpha_{21}})[A_3{A_0}^{k-1} + (k-1)A_2A_1{A_0}^{k-2} + \frac{(k-1)(k-2)}{6}{A_1}^3{A_0}^{k-3}] \; ;$$

$$for \; k > 2 \qquad (2-15)$$

where

$$A_n = \beta_{23}\beta_{32}\alpha_{34}^{n}\alpha_{32}^{n-1}\alpha_{21} \qquad (2-16)$$

One of the major advantages of wave classification is that class 'b' echoes increase while class 'a' echoes decrease. This increase is true for several reverberations and depends solely on the characteristics of Region II (or the first thin layer). The effect of Region IV (support plate) changes the class 'b' linearly, as can be seen in Equation 2-10. As the impedance of Region IV increases, b_n increases, which is a highly desirable situation for detection.

The evaluation of the b_k in terms of k, and Regions I, II, III and IV is more involved than in the previous discussion of a_k for the analysis of a single layer. However, insight into the behavior of b_k can be found by examining the maximum of 'b' echoes in terms of the reverberation number k,

$$\frac{db_k}{dk} = 0 \qquad (2-17)$$

Hence the solution for k can be determined,

$$k = \frac{-1}{log\alpha_{21}\alpha_{23}} \quad \text{where } k \text{ is an integer} \qquad (2-18)$$

The maximum value of b_k varies according to the characteristic impedance of Region II relative to Region I and III. The reverberation is prolonged as the impedance of the thin layer increases. On the other hand, for a lower impedance of the thin layer, the strongest 'b' echoes are the first few. Graphical presentation of the maximum of class 'b' echoes as a function of $\sqrt{\alpha_{12}\alpha_{23}}$ is shown in Figure 2-6.

Envelopes of class 'b' echoes for various characteristic impedances of Region I-IV are shown in Figure 2-7a-d. Figure 2-7a-d shows instances of severe to mild reverberation in Region II. In each figure, Graphs I-IV represent insignificant to significant acoustical mismatch between Region III and IV. Figure 2-7a closely resembles the class 'b' echoes of the tube/support structure for various reflection

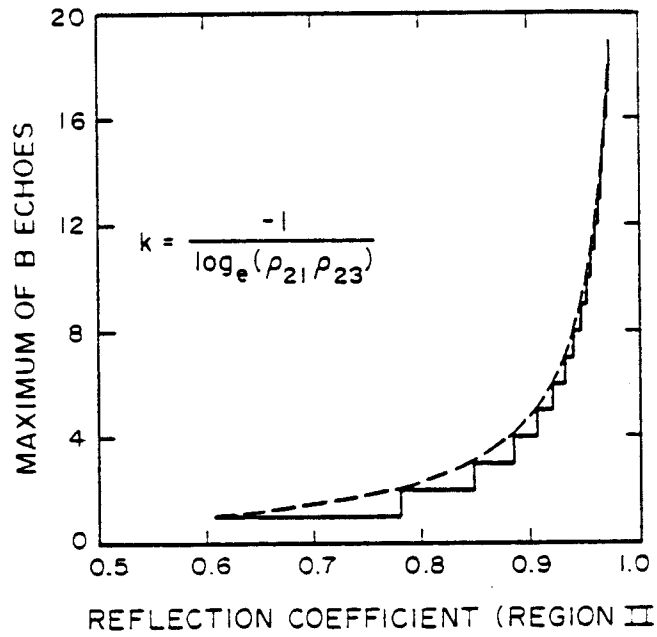

Figure 2-6. Graphical presentation of the maximum of b_n as a function of the composite reflection coefficient, $\sqrt{\alpha_{12}\alpha_{23}}$

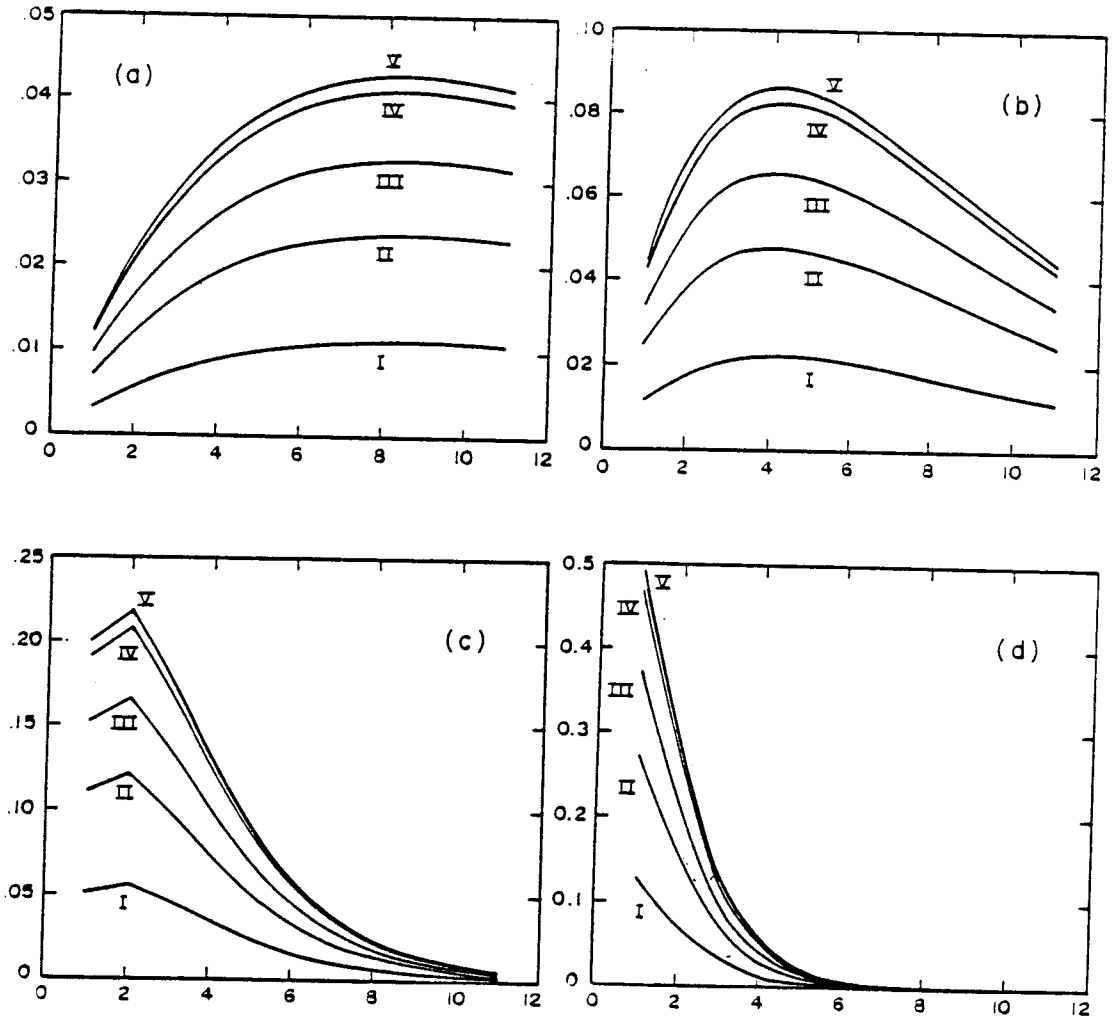

Figure 2-7. Envelope of 'b' echoes for various values of α_{34}: I) $\alpha_{34} = 0.25$, II) $\alpha_{34} = 0.54$, III) $\alpha_{34} = 0.74$, IV) $\alpha_{34} = 0.93$, and V) $\alpha_{34} = 0.97$. In each trace α ($\alpha = \alpha_{12} = \alpha_{32}$) is equivalent to; a) 0.94, b) 0.88, c) 0.74, and d) 0.54

coefficients of the support plate. This is beneficial in determining how deterioration of the support plate will affect the integrity of the signal. Furthermore, these graphical results are very useful in interpreting the received signal that leads to determining the best region in time for class 'b' echo evaluation. As shown in Figure 2-8 (this figure exhibits characteristics very similar to that of the tube/support structure), the comparison of the envelopes of the 'a' and 'b' echoes reveals that the best region for observing 'b' echoes is near b_8. A simulated backscattered signal (A-scan) of the tube/support structure where the water gap delay is smaller than the reverberation time in the tube wall can be seen in Figure 2-9. This plot gives a clear indication of the exact position of both the 'a' and 'b' echoes. The tube thickness (Region II) and gap size (Region III) can also be determined from this figure, where the tube thickness corresponds to the delay between the peaks of the echoes within each class, and the gap distance is given by the time delay between the 'a' and 'b' echoes. Similar discussions hold for class 'c', 'd', ... echoes, but their amplitudes are much smaller than class 'a' and 'b' echoes. In experimenatal data, detection of these echoes becomes very difficult. Futhermore, no additional information will be gained by their evaluation.

Experimental Results

In inspection of steam generator tube/support structures, the characterization of the inconel tube and steel support plate is pertinent in the detection of corrosion and denting. Applying the given model to steam generator tube/support structure, Region IV corresponds to the support plate and Region II corresponds to the thin tube wall. The thickness of the tube wall is about $1.4mm$ and the gap size is about $250\mu m$. The carbon plate is much thicker than the tube wall and, therefore, its dimension does not affect outcome of the reverberant signal. The 'a' echoes characterize the tube wall and are referred to as tube echoes in this paper. Likewise, the 'b' echoes are dependent upon the characteristics of Region IV and are referred to as support plate echoes.

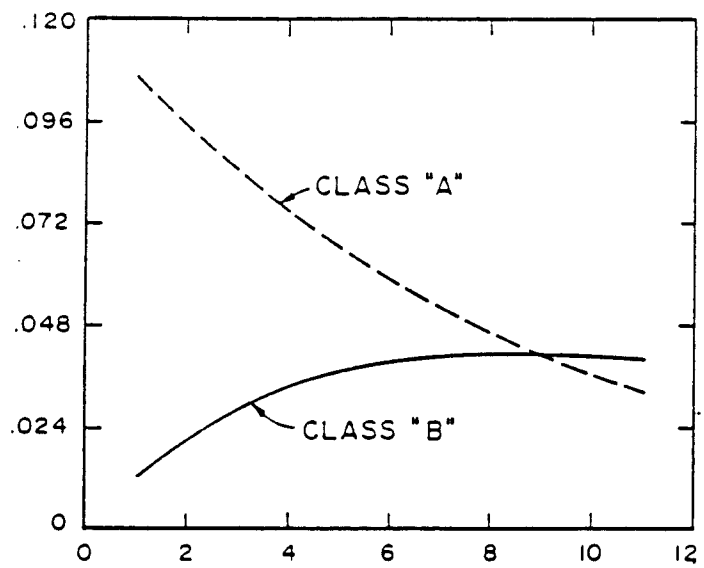

Figure 2-8. Comparison of the envelope of the class 'a' echoes (dashed line) with the envelope of the class 'b' echoes (solid line)

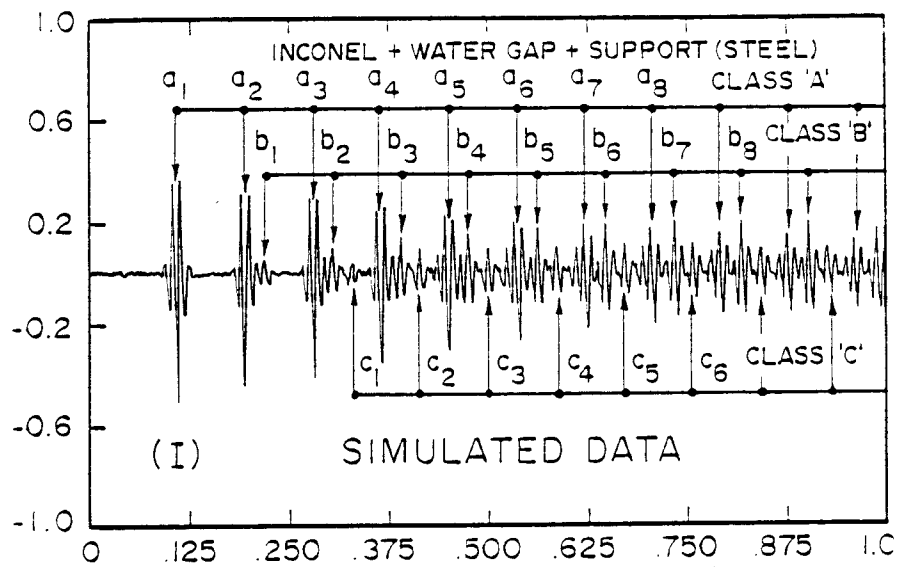

Figure 2-9. Simulated Results of the backscattered signal from the inspection of a tube/support structure

(a)

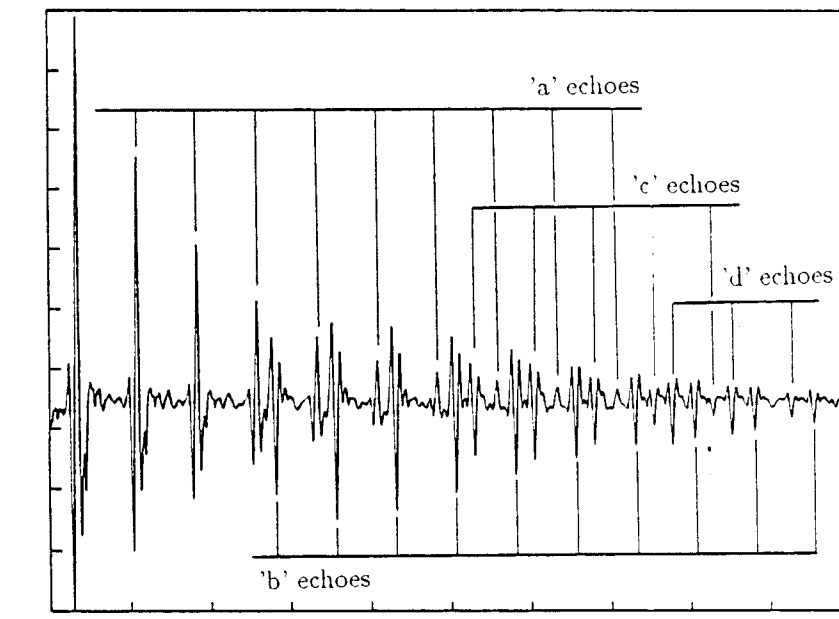

(b)

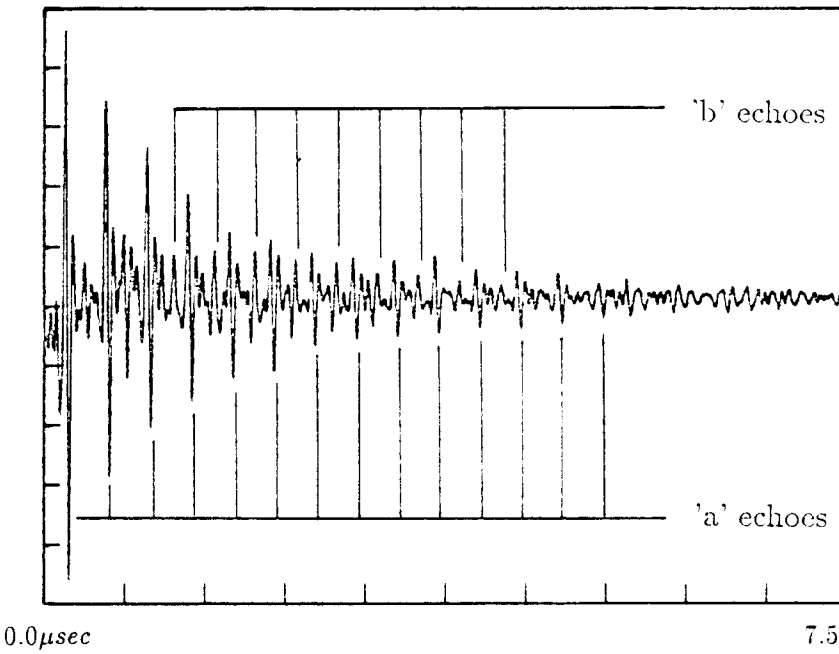

Figure 2-10. Experimental results depicting the reverberation process from the A-scan of a multilayered target consisting of four regions where; (a) is a planar model (water-aluminum-water-steel), and (b) is a tubular model (water-inconel-water-steel).

Using a transducer with a center frequency of 20MHz and a 10MHz bandwidth, experimental results (shown in Figure 2-10) confirm theoretical model predictions. Figure 2-10a shows the ultrasonic examination of a planar multilayered (consisting of four regions) structure where the reverberating thin layer is aluminum. Class 'a', 'b', 'c', and 'd' echoes exist for several reverberations. As expected, the 'a' echoes decrease with time and it is apparent that the intensity of 'b' echoes increases for a few reverberations which coincides with theoretical findings of the model.

Figure 2-10b displays the backscattered signal from an inconel tube/support structure, which is more reverberant than aluminum. The 'a' and 'b' echoes are clearly visible yet are not as pronounced as in the upper trace, and the presence of 'c' and 'd' echoes is negligible. Thus, the previous model can be simplified somewhat by focussing on the two dominant classes of echoes to give

$$r(t) = \alpha_{12}u(t) + \sum_{k=1}^{\infty} a_k u(t - 2kT_2) + \sum_{k=1}^{\infty} b_k u(t - 2T_3 - 2kT_2) + n(t) \quad (2-19)$$

where n(t) represents the error that includes all other low intensity reverberant echoes not considered and noise introduced by the measuring system. Furthermore, it should be noted that variations in the gap size (Region III) can situate the 'a' and 'b' echoes such that they become close enough to interfere with each other. Also, poor reflective surfaces (i.e. support plate) will cause deterioration in the signal in which the class 'b' echoes are severely affected. Thus, separation or decomposition would be advantageous in characterizing the tube and support plate echoes. This is especially true in experimental measurements where noise and poor signal quality create problems in detecting 'b' echoes. Therefore, additional signal processing of the backscattered signal will be neccessary to overcome some of these obstacles.

CHAPTER III

MEASUREMENT SYSTEM EVALUATION

Background

In the ultrasonic measurement of steam generator tube/support structures, there are several components that comprise the measuring system. These components include the pulser, transducer, reflector system, and the digitizer. The entire measurement system is shown in Figure 3-1. In this chapter, the basic operation of each component and its importance will be presented.

The pulser unit's main function is to generate a broadband pulse signal and, upon reflection of a pulse, receives a band-limited high frequency signal from the backscattered measurement of the transducer. The pulse generated is large in amplitude, ranging from 200 to 250 Volts. The unit used is a Panametric 5052 Pulser/Receiver. The pulser unit can manipulate the pulse with two controls; one varies the energy of the signal and the other adjusts the dampening in the signal. The energy dictates the degree of excitation the transducer is given in terms of electrical energy. The amount of excitation is usually limited by the transducer characteristics. When the transducer is overexcited, prolonged resonances occur, and the production of the transmitting echo will cause "ringing" in the signal which is not beneficial in terms of enhancing the imaging resolution of the system. In terms of the dampening controls, the main purpose is to match the impedance of the transducer piezoelectric element with the impedence of the excitation source. These topics will be discussed later on in Chapter V with experimental results showing their effects on the generated pulse.

Next in the sequence of Figure 3-1 is the transducer. Its role is to provide the transition of electrical energy into mechanical or acoustical energy. The transducer transfer function can be characterized by two parameters, the center (or resonant) frequency and the bandwidth of the transducer. It will be shown that these parameters determine the axial resolution and frequency content of the transmitted ultrasonic pulse.

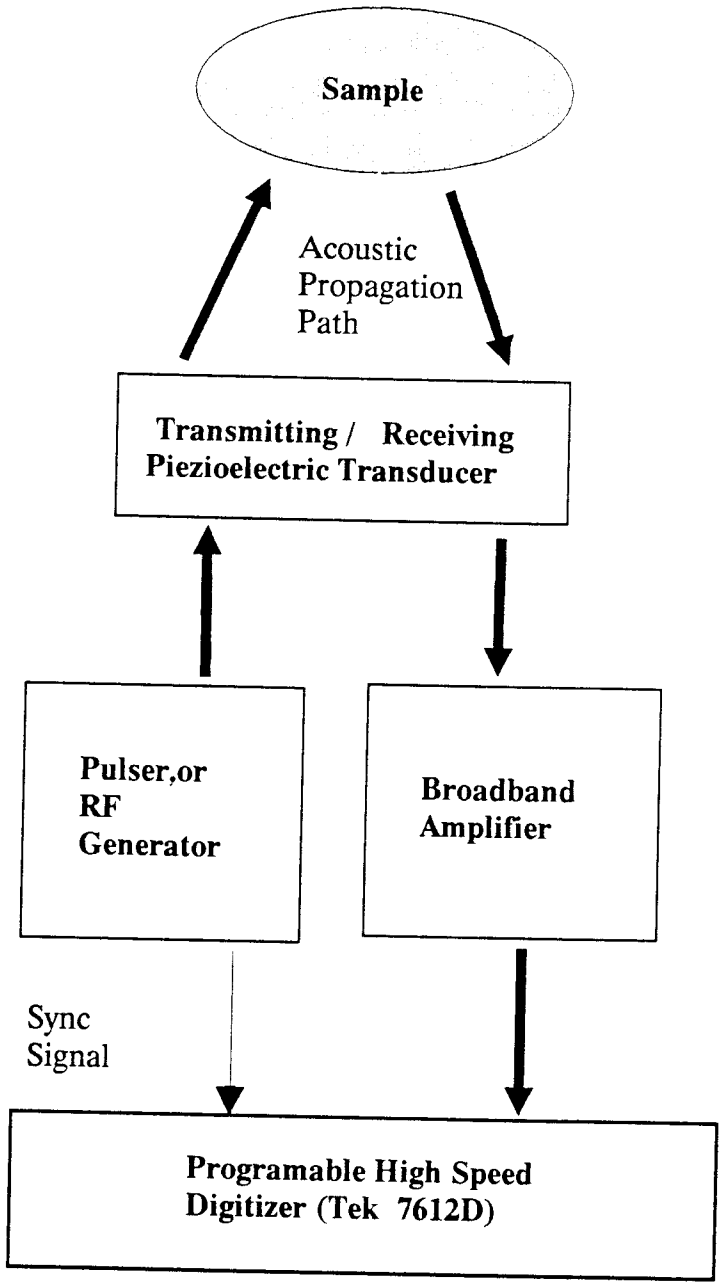

Figure 3-1. Ultrasonic data acquisition system

The 3-dB bandwidth of the transducer determines the resolution of the ultrasonic pulse. The resolution of the ultrasonic system is defined as the distance two targets must be separated in order for both targets to be detected. This is done by examining the corresponding peaks of the reflected echoes from both targets. The resolution of the system, ξ, is inversely proportional to the bandwidth and can be written as,

$$\xi = k(\frac{c}{2B}) \qquad (3-1)$$

where $1 \geq k \geq 0$, c is the speed of sound in the supporting medium, and B is the bandwidth of the signal. The variable k is a constant to compensate for the deviations in the impulse response of different transducers and the definition of echo separability in a particular measuring system. By using the following relationship, k can be found,

$$k = \Delta t B \qquad (3-2)$$

in which Δt is the duration of an observable echo of the transmitted signal.

The 3-dB bandwidth of the transducer is dependent upon the center frequency, the physical properties of the transducer, and the transmitting medium. For the case of broadband transducers, the bandwidth can be approximated as one-half the center frequency. Thus, to optimize the resolution of the transducer, the center frequency must be as high as possible. However, frequencies above 25MHz are highly attenuated due to the absorption characteristics of most materials. Also, the production of transducers with center frequencies above 25MHz is expensive and, as stated before, will produce suboptimal results in terms of received signal energy.

The impulse response, $u(t)$, of the transducer used in this research can be modeled as an echo with a normalized Gaussian envelope, given by the following equation:

$$u(t) = e^{-t^2/2\sigma^2} cos(\omega_c t) \qquad (3-3)$$

where σ^2 is the variance of the Gaussian envelope of the echo and ω_c is the center frequency of the transducer. The variance, σ^2, can be given in terms of the 3-dB bandwidth of the transducer by the following relationship

$$\sigma^2 = (\frac{B}{2})^{-2} ln2 = \frac{4ln2}{B^2} = \frac{2.77}{B^2} \qquad (3-4)$$

As discussed above, the 3-dB bandwidth, B, is related directly to the center frequency of the transducer and in turn determines the resolution of the transducer and the amount of attenuation due to absorption.

In this particular study, the transducer used has a center frequency of 20 MHz and has a 3-dB bandwidth of 10 MHz. This will provide resolution with the magnitude of a few mils in water, which corresponds to a resolution in the order of 5 mils in inconel (that comprises the steam generator tube composition). The tube walls examined are approximately 56 mils thick, which is much greater than the resolution of the transducer.

Evaluation of Different Focussing Techniques

The purpose of focussing in reference to pulse-echo examination is to concentrate the transmitted signal energy onto a smaller region of the material. This will improve the lateral resolution and allow more energy to penetrate, providing information with higher signal-to-noise ratio about the subsequent boundaries of the material. In the examination of steam generator support plate/tubing, focussing would be helpful in increasing the energy of the "b" echoes of the received signal, which describe the degree of corrosion present in the gap. There are several focussing mechanisms corresponding to either focussed or unfocussed transducers that may be employed in a focussing system, although some may be more optimal than others in terms of implementation and desired results. This section discusses three types of focussing systems and the optimality of each system in examining steam generator tubing.

Parabolic Reflectors Using Unfocused Incident Beams. The reflector corresponding to the case where the transducer used is a flat unfocused disk takes the

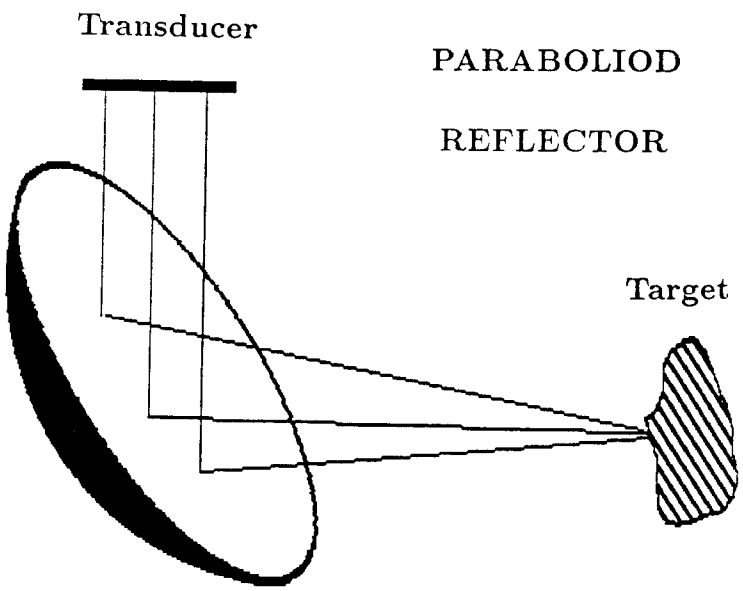

Figure 3-2. Parabolic reflector focussing system

form of a partial paraboliod (see Figure 3-2). Here the pressure wave is considered to be uniformly distributed and propagates in a parallel fashion. The parabolic reflector is used because the broad beam must be focussed onto a small region of the target (ideally a point) and yet keep the same travel time to prevent distortion caused by receiving echoes out of phase. For the derivation of the locus of points for the two-dimensional, let us assume

$$C_1 + C_2 = k, \tag{3-5}$$

where k is an arbitrary constant, C_1 is the distance between the center of the transducer to the center of the reflector, and C_2 is the distance between the center of the reflector to the focal point of the target. The constraint on the all points constituting the reflector is

$$a_1 + a_2 = k \tag{3-6}$$

where a_1 and a_2 are the arbitrary paths between the transducer and reflector and the reflector and the target, respectively. The variables C_1,C_2,a_1, and a_2 are shown graphically in Figure 3-3. In designing the reflector, the values of C_1 and C_2 are chosen to accomodate the height of the transducer from the reflector and the inner radius of the tube under examination.

This locus of points can be found in an $x - y$ coordinate system (see Figure 3-3) by substituting

$$a_1 = (C_1 - y)\ ;\ a_2 = \sqrt{(C_2 - x)^2 + y^2} \tag{3-7}$$

into Equation (3-6), which gives

$$(C_1 - y) + \sqrt{(C_2 - x)^2 + y^2} = C_1 + C_2 \tag{3-8}$$

The above equation can be simplifed to:

$$y = \frac{1}{2C_2}(x^2 - 2C_2x) \tag{3-8}$$

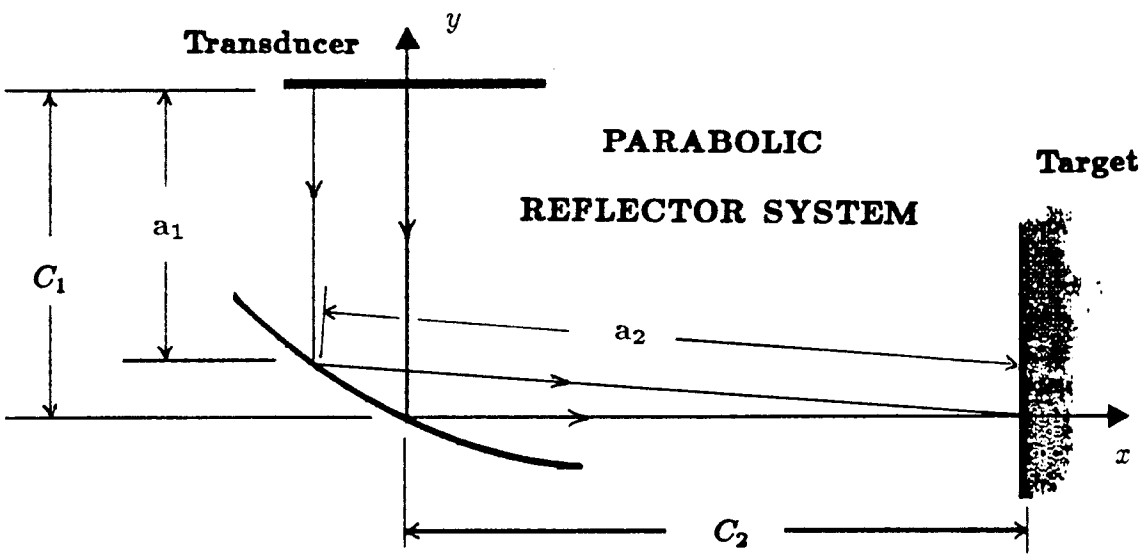

Figure 3-3. Locus of points corresponding to the parabolic reflector

for the 2-dimensional representation of the reflector. Equation (3-8) represents the curve of the the cross section through the center of a three-dimensional reflector.

The curve for the 3-dimensional reflector can be found by rotating the above equation radially about the line $x = C_2$, which is

$$z^2 + (x - C_2)^2 = 2C_2(y + \frac{C_2}{2}) \qquad (3-9)$$

where z is perpendicular to the $x - y$ plane. This insures that the distance from a given point on the reflector and the focal point of the target remain constant for any point on the reflector with the same corresponding ordinate or y value. The ordinate value of the points must be equal to include all points on the reflector that have the same travel time from the unfocused transducer.

Notice that the reflector shape is independent of the height at which the transducer is located, variable C_1. Thus, the position of the transducer is not that critical and makes implementation simpler, although the reflector shape is dependent on the distance from the center of the reflector to the focal point, C_2, which makes its application very specific in terms of tube sizes tested. There are several more drawbacks to this system, as discussed in the following paragraphs.

Even though the reflector is independent of C_1, the effect of beam spreading puts constraints on using this attractive feature of parabolic reflectors. In the farfeild region, an approximation of the beam spread angle is given [Wel69]:

$$A = 2sin^{-}1(.5\frac{\lambda}{D}) \qquad (3-10)$$

where A is the beam-spread angle, λ is the wavelength of the ultrasonic echo and D is the diameter of the transducer element. In our application, the center frequency of the transducer is 20MHz and has a diameter of 0.25", which will produce a beam spread angle of 2.67^o. Considering the fact that the ultrasonic beam will be confined by the transducer apparatus in measuring steam generator tubing, the beam will become distorted if the distance C_1 is too large.

The usage of an unfocused transducer using a parabolic reflector introduces several problems concerning the performance of the reflector and the construction of the reflector itself. In terms of the practical reflectors performance, the

travel time and focal point are designed to produce meaningful measurements, but noticing that the incident angle of the ultrasonic beam is not normal to the target. The greater the incident angle becomes, the more energy is reflected away from the detectable beam-feild of the transducer. This is shown graphically in Figure 3-4, where the dashed lines represent information that is reflected away from the receiving system. Thus, the entry angle must be as small as possible to produce a beam traveling in almost parallel lines of direction. In designing this system, the user can not vary the aperture at which the incident beam hits the target because this feature is governed solely by the reflector focal length, C_2, which is a fixed quantity when a specific tube size is chosen.

It should be noted that there is some interest in scanning at oblique angles with the intent of detecting edges or cracks in the material. The motivation behind using this scanning technique is to obtain a better vantage point of the flaw or edge when these discontinuities in the material are not prominent under normal angle scanning. This technique is presented in Chapter IV, where the physical principles behind transmission and reflection of an incident beam at an oblique angle are discussed in great detail, with corresponding experimental results.

In terms of constructing a parabolic mirror, the reflector should have the correct curvature and smoothness at every point on the reflector to produce the optimal results. To produce a mirror of such quality would be very expensive and, due to its limited applications, would be very impractical. In consulting a representative from the Harrisonic Laboratories, Inc., he conveyed that producing a mirror of such small size (approximately .5" in diameter) corresponding to the correct curvature and neccessary smoothness could not be reasonably constructed without great difficulty. Thus, the unfocused transducer is not recommended for tube measurements since it can not provide adaptive focussing without, distortion due to inherant constraints on the reflector and can not be readily obtained.

Reflector Systems Using Focussed Incident Beams. An effective focussing technique is using a spherically-focused transducer combined with two types of reflectors; one is a partial ellipsiod and the other is a flat plane surface. The schematic for the elliptical focussing system can be seen in Figure 3-5, where the

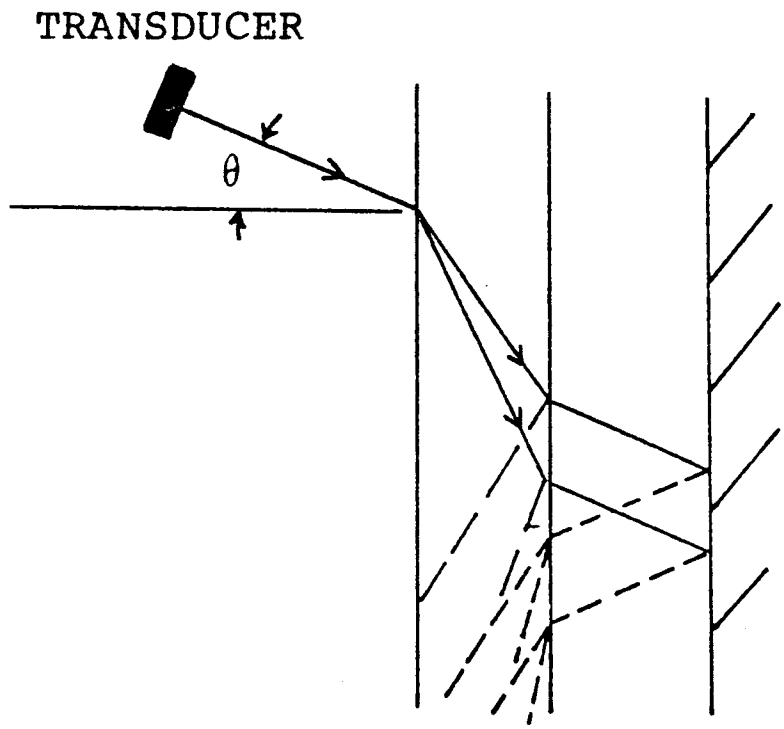

Figure 3-4. Propagation of an beam at an oblique angle

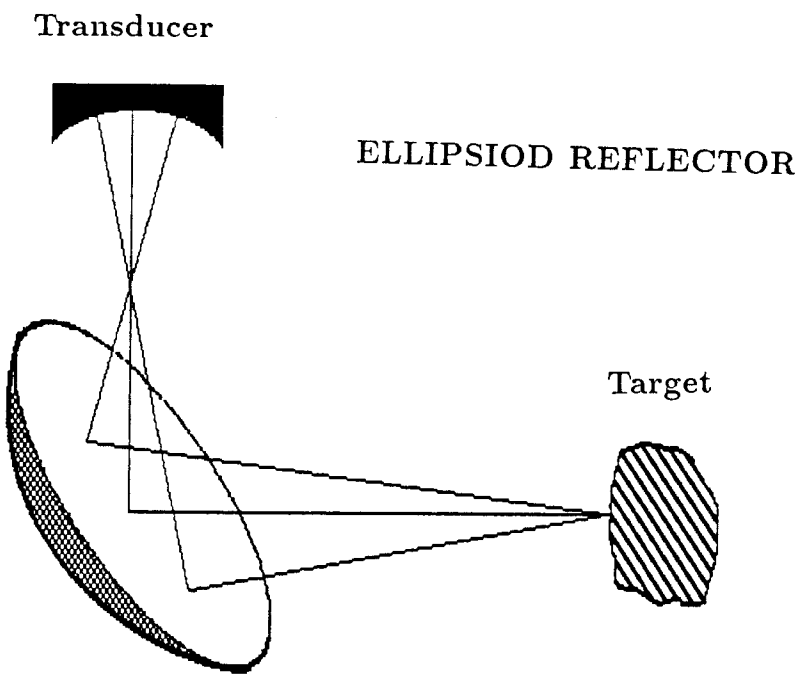

Figure 3-5. Elliptical focussing system

two focuss points of the ellipse correspond to the focal point of the transducer and the inspection point of the target. In developing this reflector, first the locus of points at the midsection of the reflector will be defined and then will be rotated to encompass the entire reflector. The variables used in the derivation of the mid-section ellipse are defined below and can be seen graphically in Figure 3-6:

C_1 = the distance from the focal point of transducer to the origin of the reflector.

C_2 = the distance from the origin of the reflector to the focal point of the target.

θ_0 = the angle rotation of the major axis of the ellipse with respect to the x axis.

y_0= displacement of ellipse from the origin in the y direction.

x_0= displacement of ellipse from the origin in the x direction.

x' = x-coordinate rotated an angle θ_0.

y' = y-coordinate rotated an angle θ_0.

x_0' = displacement x_0 rotated an angle θ_0.

y_0' = displacement y_0 rotated an angle θ_0.

The locus of points for this reflector must satisfy the below constraint:

$$a_1 + a_2 = 2a \qquad (3-11)$$

in order for the reflected beams to have uniform travel time from the radiating source located point $(0, C_1)$ to the focal point of the target located at $(C_2, 0)$. The variables a_1 and a_2 are arbitrary beam paths from the transducer to the reflector and from the reflector to the target, respectively, and $2a$ is the specified length of the major axis of the ellipse. If the center of the reflector corresponds to the center of the incident beam then the following relationship will hold:

$$C_1 + C_2 = 2a \qquad (3-12)$$

which is shown graphically in Figure 3-6. When the above constraint is not adhered to, then the traveling distance, $2a$, becomes a free variable in the system. This can be seen graphically in Figure 3-7, though the variation in the travel distance does not buy us anything in terms of reflector focusing performance, as is discussed later on.

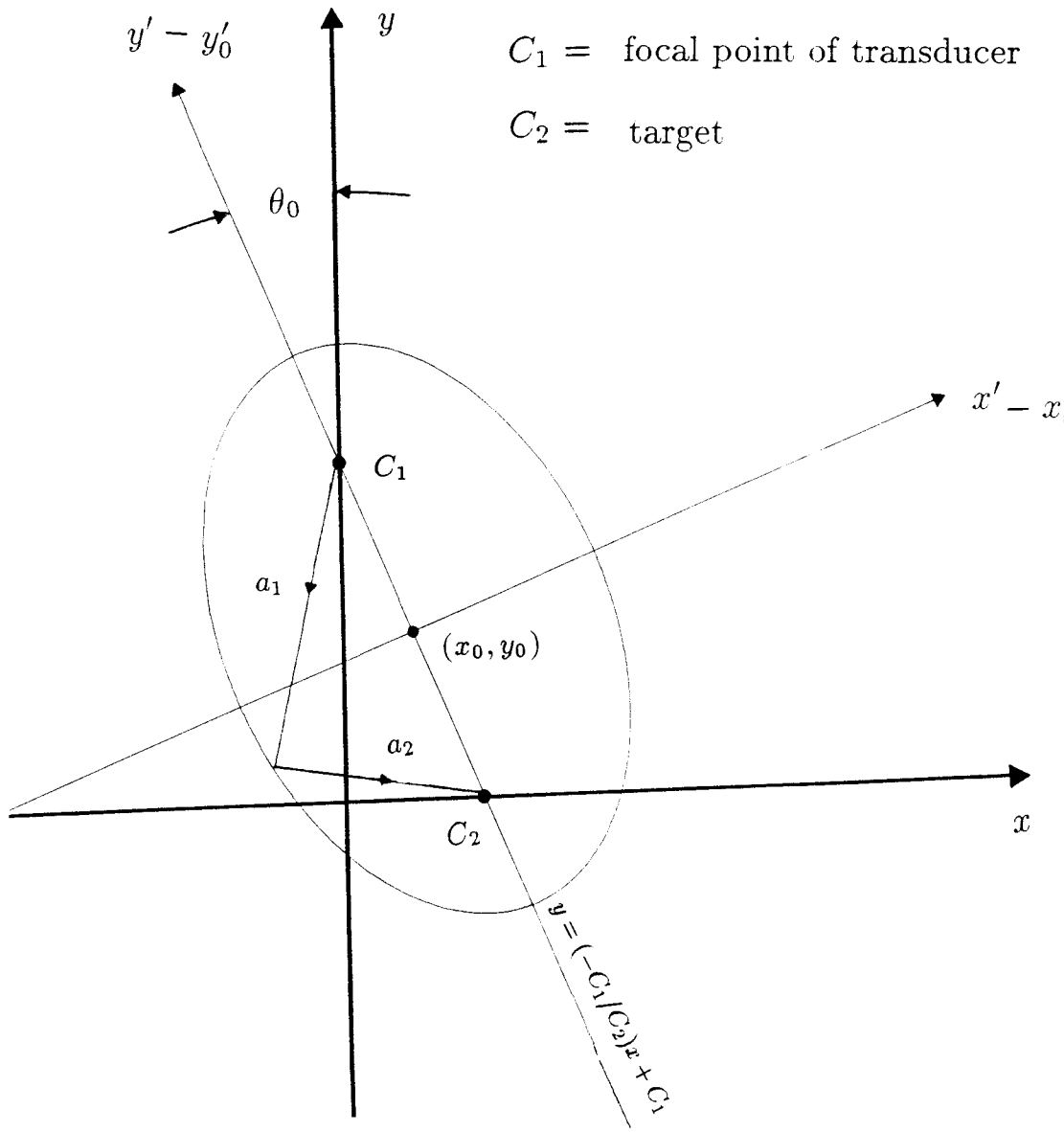

Figure 3-6. The locus of points [illegible] located on the midsection of the reflector

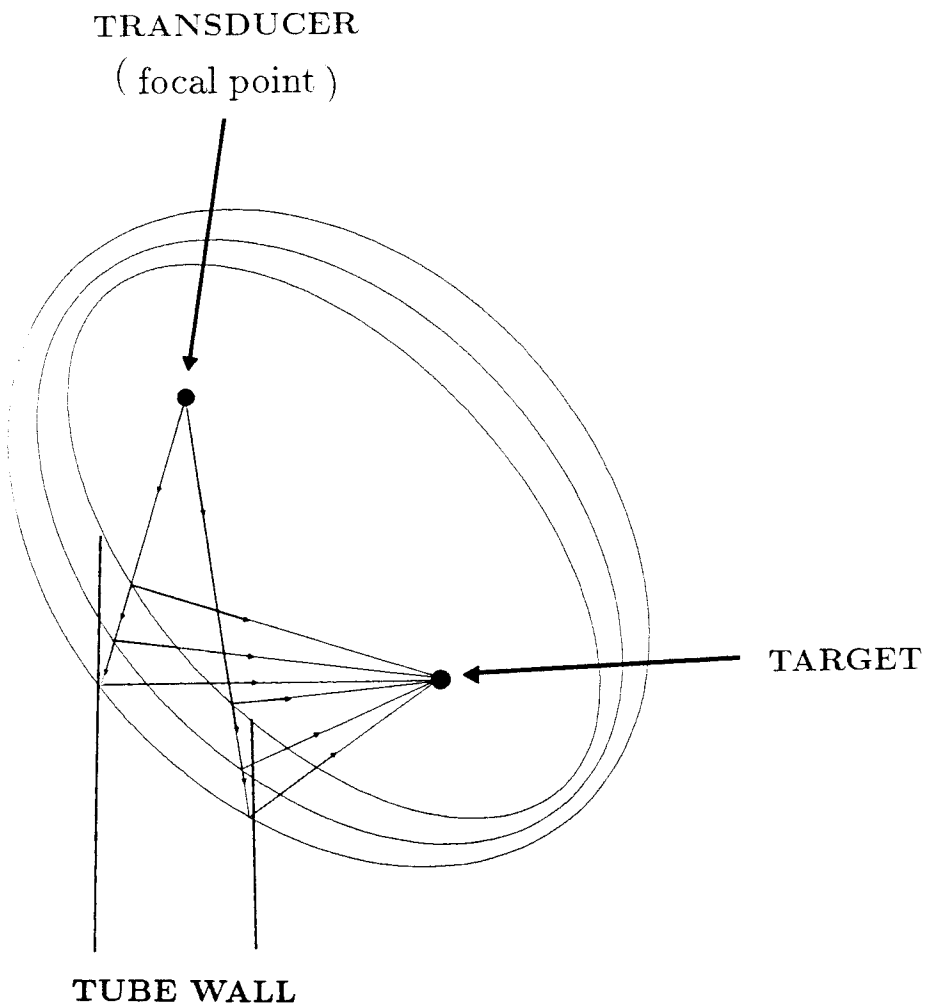

Figure 3-7. Various possible elliptical reflectors with identical focal points

The focal length, c, of the elliptical reflector (shown in Figure 3-6) is given by

$$c = \sqrt{{C_1}^2 + {C_2}^2} \qquad (3-13)$$

which is simply half the distance between the two foci of the ellipse. Since the focal points of the ellipse lie on the ordinate and abscissa respectively (see Figure 3-6), the major axis of the ellipse is a line intersecting both of these points which means the ellipse will be rotated by some angle, θ_0. This angle of rotation can be determined by the following relationship:

$$\theta_0 = sin^{-1}(\frac{C_1}{\sqrt{{C_1}^2 + {C_2}^2}}) \qquad (3-14)$$

The displacements from the origin in the x-y coordinate system can be determined by finding the center of the ellipse. The center of the ellipse can be found by taking the midpoint between the two focal points which corresponds to point (x_0, y_0). The value of x_0 and y_0 is given by

$$x_0 = \frac{C_2}{2} \;\; ; \;\; y_0 = \frac{C_1}{2} \qquad (3-15)$$

The equation of the ellipse can be simplified by expressing them in the rotated x'-y' coordinate system. The displacements from the origin in the x'-y' coordinate system, x_0' and y_0', are given by

$$x_0' = x_0 cos\theta_0 + y_0 sin\theta_0 = \frac{({C_2}^2 - {C_1}^2)}{2\sqrt{{C_1}^2 + {C_2}^2}} \qquad (3-16)$$

$$y_0' = -x_0 sin\theta_0 + y_0 cos\theta_0 = \frac{C_1 C_2}{2\sqrt{{C_1}^2 + {C_2}^2}} \qquad (3-17)$$

Using this information, the equation of the rotated ellipse can be written as

$$\frac{(y' - {y_0}')^2}{a^2} + \frac{(x' - {x_0}')^2}{b^2} = 1 \qquad (3-18)$$

where a is given, and c is known from Equation (3-12) and $b = \sqrt{a^2 - c^2}$.

The three-dimensional formulization of the ellipse is obtained by rotating the two-dimensional ellipse about the line $y = (-C_1/C_2)x + C_1$. This will give an equation of the form:

$$\frac{(x' - x'_0)^2}{a^2} + \frac{(y' - y'_0)^2}{b^2} + \frac{z^2}{b^2} = 1 \qquad (3-19)$$

in which z is perpendicular to x-y plane and has not been rotated like x' and y'. Equation (3-19) exists for the space concurring with the following constraints:

$$x^2 + y^2 \leq r^2 \quad and \quad y \leq \frac{-C_1}{C_2}x + C_1, \qquad (3-20)$$

where r is the defined by the inner radius of the reflector apparatus. In our present system, r corresponds to 0.383".

For the elliptical reflector, two focal points are used, one of which corresponds to the focal point of the transducer, while the other is maintained on the target surface. The focal point of the transducer acts like a point source such that the transducer height must be fixed and located a height equal to or greater than the focal length of the transducer. The other focal point on the target must also be a fixed quantity so as to describe the locus of point of the reflector. This suggests that both the system remains fixed for all measurements, which severely limits its flexibility.

Similar to the case of the parabolic reflector, the elliptical mirror is very difficult to manufacture such that the surface will accurately reflect beams emanating from a psuedo point source onto the specified focal point of the target. One of the problems of this reflector is that it is assuming that the incident beams are derived from a point source. A point source is impossible to emulate directly, because the pizioelectric device would not be sufficiently large enough to transmit the required energy to penetrate the material. The point source can be simulated by using a spherically focused transducer, where the focal point of the transducer is taken to be the point source of the reflector. The pseudo point source will also be subject to error due to the property of beam spreading. This spreading will hinder the

effectiveness of the mirrors capability to transfer all available acoustic energy onto the target.

Further detriments to the performance of the elliptical reflector are due to the fact that the incident beam will be askew to the normal of the target. In the previous derivation where a parabolic reflector was used, it was shown that this causes distortion in the measured signal. To minimize this error, the elliptical reflector can be designed (by choosing an appropiate value for a) so that a smaller portion of the mirror is used. This will tend to decrease the incident angle beam penetrating the target, and, consequently, the distortion in the signal is also reduced. There is a drawback to using a smaller reflector area, which is that the focused beam becomes more sensitive to surface imperfections. Another result of varying a, which can be observed from Figure 3-7, is the increase of the incident angle of the central portion of the beam. Since the majority of energy is contained near the center of the beam profile, the optimal reflector should direct the center of the beam towards the target in a normal fashion. This corresponds to the case where a is given by Equation 3-12. As stated earlier, the cost to produce a mirror of such quality containing inflexible focusing characteristics is impractical for our application.

The final reflector system (coupled with a focused transducer) considered is one which utilizes a flat surface orientated at a 45^o angle. The flat surface reflector translates the direction of the focused beam 90^o, as shown in Figure 3-8. It can be seen that for the beam to be focused to a point on the target, the total travel path (from transducer to target) is equivalent to the focal length of the transducer (see Figure 3-8). This constraint can be written as

$$C_1 + C_2 = f = \text{ focal length of transducer} \qquad (3-21)$$

where C_1 and C_2 are defined, as before, as the displacements of the transducer and target from the reflector. The only requirements in the implementation of this reflector system is that the height of the transducer must be mobile for different tube diameters, and that the distance from target to the reflector, C_2, is less than the focal length of the transducer. In our application, the tube/transducer

The three-dimensional formulization of the ellipse is obtained by rotating the two-dimensional ellipse about the line $y = (-C_1/C_2)x + C_1$. This will give an equation of the form:

$$\frac{(x' - x'_0)^2}{a^2} + \frac{(y' - y'_0)^2}{b^2} + \frac{z^2}{b^2} = 1 \qquad (3-19)$$

in which z is perpendicular to x-y plane and has not been rotated like x' and y'. Equation (3-19) exists for the space concurring with the following constraints:

$$x^2 + y^2 \leq r^2 \ \ and \ \ y \leq \frac{-C_1}{C_2}x + C_1, \qquad (3-20)$$

where r is the defined by the inner radius of the reflector apparatus. In our present system, r corresponds to 0.383".

For the elliptical reflector, two focal points are used, one of which corresponds to the focal point of the transducer, while the other is maintained on the target surface. The focal point of the transducer acts like a point source such that the transducer height must be fixed and located a height equal to or greater than the focal length of the transducer. The other focal point on the target must also be a fixed quantity so as to describe the locus of point of the reflector. This suggests that both the system remains fixed for all measurements, which severely limits its flexibility.

Similar to the case of the parabolic reflector, the elliptical mirror is very difficult to manufacture such that the surface will accurately reflect beams emanating from a psuedo point source onto the specified focal point of the target. One of the problems of this reflector is that it is assuming that the incident beams are derived from a point source. A point source is impossible to emulate directly, because the pizioelectric device would not be sufficiently large enough to transmit the required energy to penetrate the material. The point source can be simulated by using a spherically focused transducer. where the focal point of the transducer is taken to be the point source of the reflector. The psuedo-point source will also be subject to error due to the property of beam spreading. This spreading will hinder the

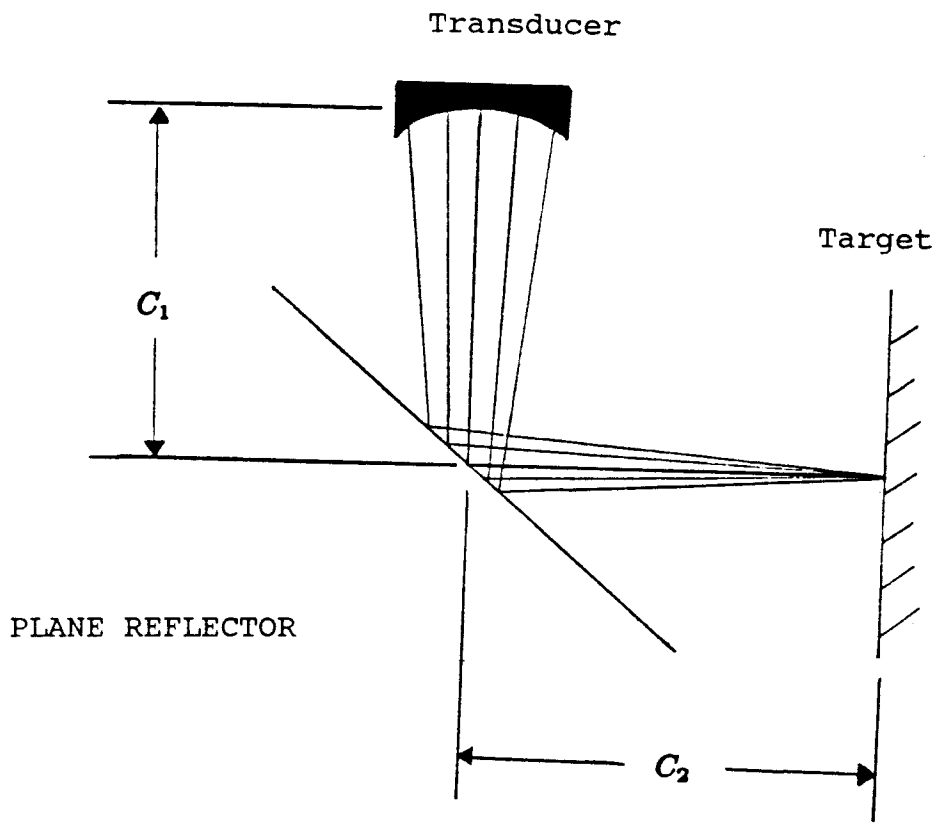

Figure 3-8. Plane surface reflector system

assembly can accomodate adjusting the transducer height. Also for the transducer used, the focal length is given as a 0.5" and the tubes that we are dealing with in the present investigations are 0.661" in diameter.

In the plane reflector system, the symmetry of the beam with respect to the normal of the incident plane is preserved after reflection. Thus, the beam penetrating the target is symmetric with respect to the normal of the target and eliminates this source of distortion. The entry angle is fixed in the case of the flat surface reflector because it is governed by the focusing characteristics of the transducer itself. So, it would be beneficial in the sense of mininizing the incident angle to have the longest possible focal length available, though often transducer focusing performance will deteriorate greatly when the focal length becomes too large. In choosing the optimal reflector system, the plane surface reflector seems to be the most simple and effective system to implement. In terms of manufacturing, one can obtain very high degrees of smoothness in a flat surface reflector at nonimal costs. Also, the plane reflector system allows for focal point to be adjustable and move as the transducer moves. Thus, this provides flexibility in the examination of different size tubes and includes the possibility of adjusting the focal point into a target for usage in other types of scanning techniques. The other reflectors described in this chapter provide the added feature of focussing enhancement, whereas there is none provided with the plane reflector, although inherent complexities exists in their production and implementation make them an unviable alternative to the plane reflector. Therefore, the plane reflector is best suited for tube/support plate measurements because it provides accurate focussing while remaining very simple and flexible to use.

The implementation of this reflector can be seen in Figure 3-9, where the transducer is fixed inside the reflector housing. The reflector housing has two rubber o-rings at each end to provide the ability to move axially and radially within the tube structure and yet sufficient stability during measurements. Also these o-rings provide a seal to hold the water in, which is neccessary for the transmission of sound. This reflector assembly provides a method of completely scanning the tube structure.

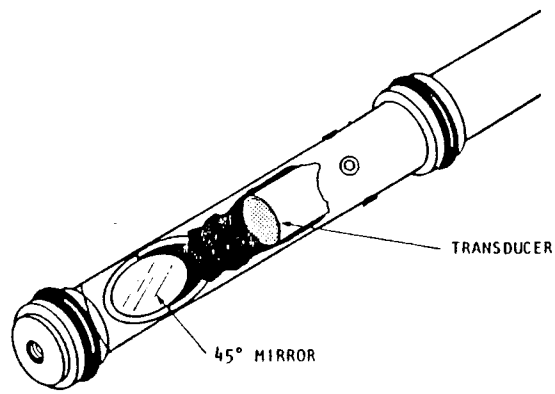

Figure 3-9. Reflector Assembly

CHAPTER IV

OBLIQUE ANGLE SCANNING

Introduction

Oblique angle scanning (OAS) provides the automatic rejection of 'a' echoes (tube echoes) while still preserving the information-bearing 'b' echoes (support plate echoes) in the backscattered signal [San87]. In general, as the scanning angle varies, the degree of refraction and reflection and energy transfer that occurs at each interface changes dramatically and complicates the evaluation of detected multiple echoes. Thus, for this technique to be most effective the choice of the oblique angle must be conducive to the optimality criterion, which means the scanning angle must be chosen to reject a sufficient amount of 'a' echoes and maximize the energy of 'b' echoes in the received signal. Besides satisfying the optimality criterion, the scanning angle is confined by system constraints such as the range of detection of the transducer or the physical dimensions of the tube/support structure. In this study, the relationship between the scanning angle and the beam interactions at each boundary are given explicitly and analyzed to satisfy the optimality criterion.

Theoretical Analysis

The effect of refraction and reflection in the oblique angle scanning of a simplified planar tube/support structure is illustrated in Figure 4-1. Mode conversion is evident at the liquid/solid interface, where the incident beam penetrates an elastic medium (solid) and creates two transmitted waves, one longitudinal and the other shear. The propagation of these two waves differs in intensity, direction, and velocity. However, liquids do not support the propagation of shear waves since they are inelastic by nature. The effect of mode conversion at the solid interface increases the number of reverberant echoes tremendously.

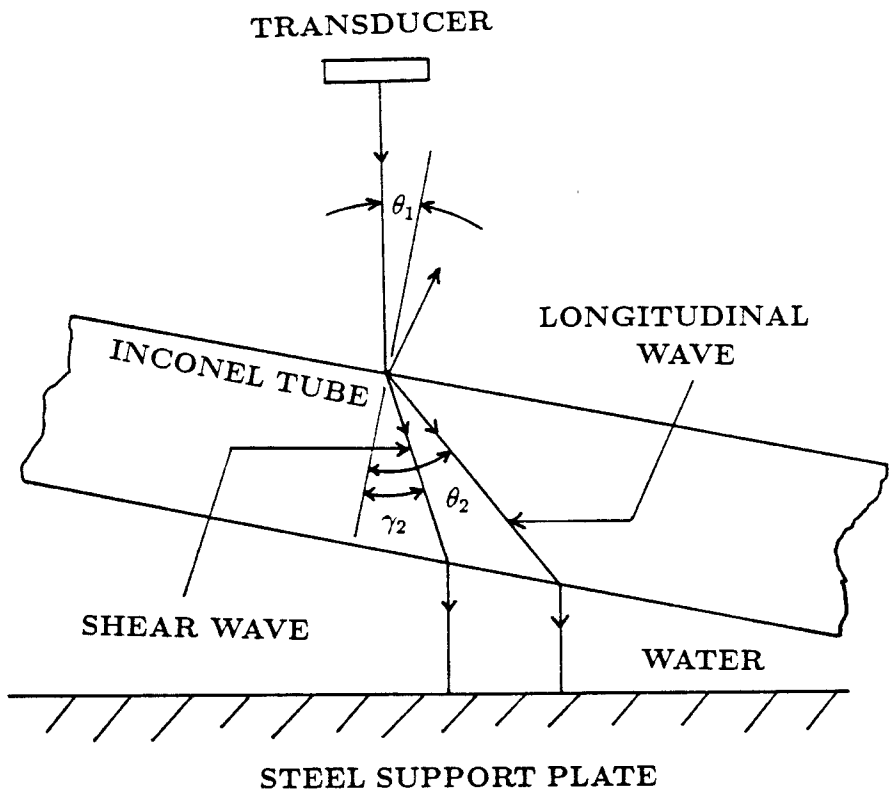

Figure 4-1. Planar model of oblique angle scanning of tube/support structure

The redirection of the incident energy is governed by Snell's Law:

$$\frac{sin\theta_1}{v_{l1}} = \frac{sin\theta_2}{v_{l2}} = \frac{sin\gamma_2}{v_{s2}} \qquad (4-1)$$

where θ_i and γ_i are the angles (measured with respect to the normal of the boundary) and v_{li} and v_{si} are the velocities of the longitudinal and shear waves, respectively, in the given medium i (where medium 1 is liquid and medium 2 is solid). As can be seen from the above equation, the velocities of the waves before and after impinging the boundary determine the degree of refraction or reflection. The velocity of the longitudinal wave is approximately twice that of the shear wave in most materials, which infers that the longitudinal wave will have greater refraction than the shear wave for oblique angles.

The reflections and refractions that take place in the tube structure eliminate the detection of 'a' echoes by directing the backscattered echoes away from the transducer. This can be seen in Figure 4-2 (only the longitudinal class 'a' echoes are shown for visual clarity). If the first reflected wave is out of the detection range, then all subsequent reverberations will not be detected since the returning echoes are shifted laterally as the reverberations progress. The composite effect of this shifting will result in a greater rate of decay of the 'a' echoes. It can be shown from Equation 19 that as the scanning angle is increased, the further the beams are reflected away from the transducer. Thus, a lower bound on the scanning angle can be constructed to eliminate a significant amount of 'a' echoes. This lower bound, θ_{1min}, can be derived from the geometry of Figure 4-2,

$$\theta_{1min} = \frac{1}{2}tan^{-1}(\frac{B}{2X_f}) \qquad (4-2)$$

where X_f is the path distance from the transducer to target and B is the beam field for class 'a' rejection criteria. For example, the 20 MHz transducer used to obtain experimental data has a detection beam field of approximately 2 mm and a target distance of 1.5 cm, which corresponds to a minimum angle of 1.9^o.

Unlike the 'a' echoes, the 'b' echoes are preserved since the angle of incidence of the returning echoes is equivalent to the initial incident beam. Figure 4-3

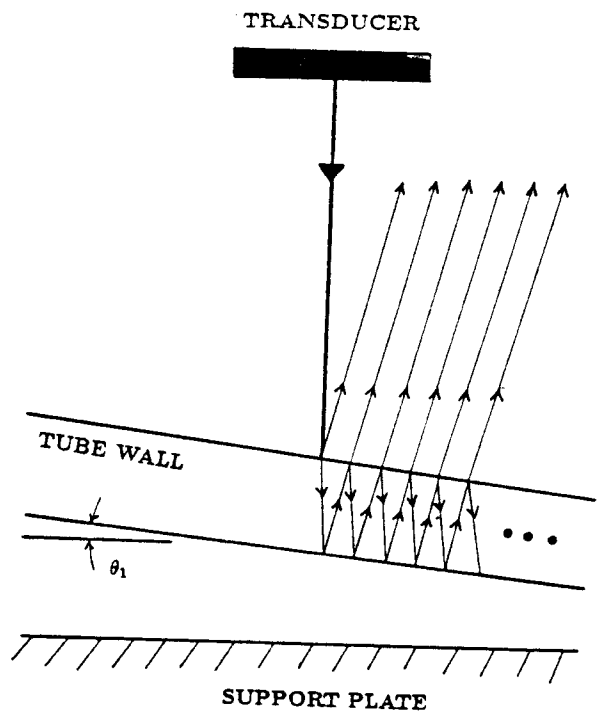

Figure 4-2. Progression of reverberations of 'a' echoes which are rejected using OAS

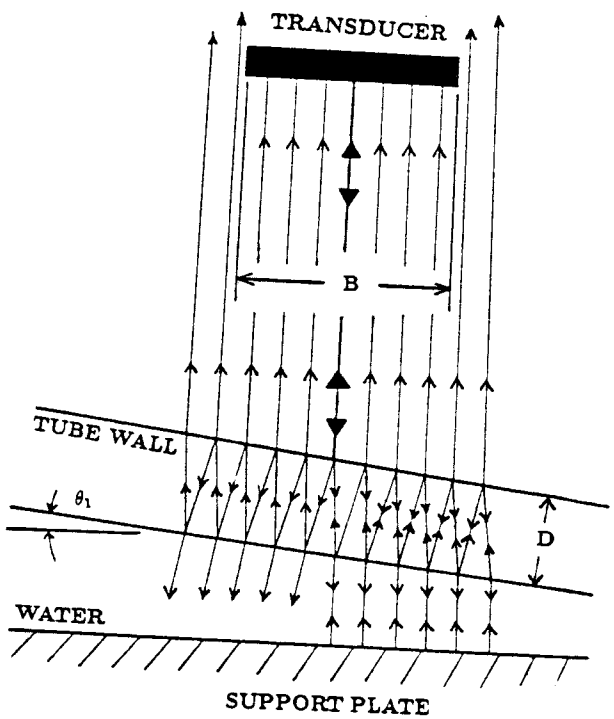

Figure 4-3. Progression of reverberations of 'b' echoes using OAS within the tube/support plate structure

illustrates the oblique angle scanning reverberation process for the 'b' echoes, not showing the shear waves or the 'a' echo patterns to simplify the figure. Although the returning 'b' echoes have been unaltered in terms of direction in the refraction process, the 'b' echoes have been shifted laterally similar to the 'a' echoes as previously discussed. As the scanning angle increases, the refracted angles increase and the lateral shifting becomes more dominant. Thus, to capture a mininum number of reverberations, an upper bound on the scanning angle, θ_{1max}, may be found by examining the geometry of Figure 4-3, which gives the following equation:

$$cos\theta_1 = \frac{B}{DNtan\theta_2} \qquad (4-3)$$

where θ_1 is the incident angle, θ_2 is the longitudinal refracted angle, D is the tube thickness, N is the minimum number of returning echo paths detected, and B is the known beam field. Using Snell's Law, Equation 21 can be solved to find θ_{1max}.

$$\theta_{1max} = sin^{-1}\sqrt{\frac{1}{2}[(1+\eta^2) - \sqrt{(1+\eta^2)^2 - 4\eta^2k^2}]} \qquad \text{for k} < 1 \qquad (4-4)$$

where

$$k = \frac{v_{l1}}{v_{l2}} \qquad and \qquad \eta = \frac{B}{2ND}$$

The above equation can be used to examine the number of possible 'b' echoes that can be detected. For example, using a tube thickness of 1 mm and requiring five reverberations to be within the detection field forces an upper bound on incident angle, $\theta_{1max} = 2.7^o$. In practice, the incident angle θ_1, must be bounded by θ_{1min} and θ_{1max}, i.e.,

$$\theta_{1min} \leq \theta_1 \leq \theta_{1max} \qquad (4-5)$$

In general, the above condition may not be satisfied if the value of N exceeds the physical limits of the system. If the above example is modified, so that there are ten required reverberations, the result is $\theta_{1max} = 1.4^o$, which is contradictory to the optimal criterion. Equation 4-5 simplifies the analysis of the energy transfer functions of the reverberant tube/support plate structure considerably.

During the reverberation process of oblique angle scanning, there are three types of mode-boundary wave interactions that occur. These are circled in Figure 4-4 and labeled case 1,2, and 3. All three have different energy transfer characteristics and contribute to the development of the 'b' echoes in some way. The longitudinal wave incident on a liquid/solid boundary is referred to as case 1, as shown in Figure 4-4. Case 1 interface determines how much energy is transmitted into the tube wall, which should be maximized to reduce the amount of energy that is lost on initial penetration of the tube wall. Case 2 corresponds to the situation where a longitudinal beam is incident on a solid/liquid boundary in which its energy transfer characteristics describe how much energy leaks out of the tube wall and the degree of mode conversion. In order to increase the energy of the 'b' echoes, transmission into the water gap should be maximized. Case 3 refers to a shear wave incident on a solid/liquid boundary and has optimal requirements similar to case 2. The explicit solutions for the energy transfer functions (i.e., shear and longitudinal) of these cases are known [Bre80,Ewi57], assuming that the incident beam is a plane harmonic wave and that the boundary is homogeneous (which means that energy is conserved).

Wave generation for case 1 consists of one reflected wave and two transmitted waves in which the energy relationships with respect to the incident beam are given below:

$$\left(\frac{\varphi_1'}{\varphi_1}\right)^2 = \left|\frac{-Z_1 G_{l2} G_{s2} + G_{s2} cos^2 2\gamma_2 + G_{l2} sin^2 2\gamma_2}{Z_1 G_{l2} G_{s2} + G_{s2} cos^2 2\gamma_2 + G_{l2} sin^2 2\gamma_2}\right|^2 \qquad (4-6)$$

$$\left(\frac{\varphi_2}{\varphi_1}\right)^2 = \frac{4\rho_1 tan\theta_1}{\rho_2 tan\theta_2}\left|\frac{G_{s2} cos 2\gamma_2}{Z_1 G_{l2} G_{s2} + G_{s2} cos^2 2\gamma_2 + G_{l2} sin^2 2\gamma_2}\right|^2 \qquad (4-7)$$

$$\left(\frac{\psi_2}{\varphi_1}\right)^2 = \frac{4\rho_1 tan\theta_1}{\rho_2 tan\gamma_2}\left|\frac{G_{l2} sin 2\gamma_1}{Z_1 G_{l2} G_{s2} + G_{s2} cos^2 2\gamma_2 + G_{l2} sin^2 2\gamma_2}\right|^2 \qquad (4-8)$$

where subscript 1 indicates the propagating medium is water, and subscript 2 indicates the propagating medium is inconel (hardened steel). The variables used in all three cases represent:

φ_i: The intensity of the longitudinal wave in region i

φ_i': The intensity of the reflected longitudinal wave in region i

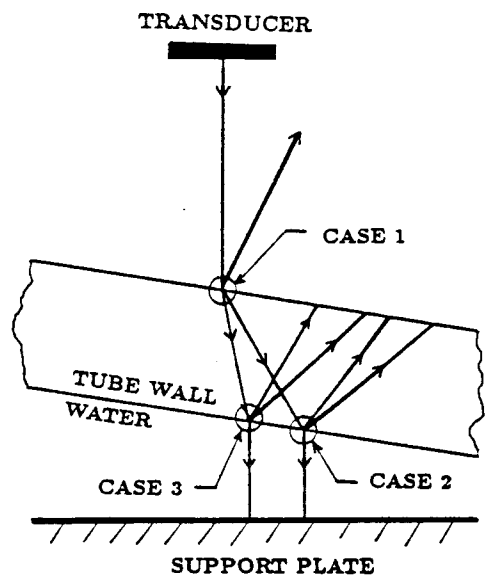

Figure 4-4. The three cases of refraction and reflection scenarios encountered during the reverberation process within the tube/ support plate structure

ψ_i: The intensity of the shear wave in region i

ψ_i': The intensity of the reflected shear wave in region i

θ_i: The angle of the longitudinal wave in region i

γ_i: The angle of the shear wave in region i

ρ_i: The density of the region i

v_{li}: The velocity of the longitudinal wave in region i

v_{si}: The velocity of the shear wave in region i

Also, in order to simplify the energy relationships, the acoustic impedance and admittance will be defined as follows:

$$Z_1 = \frac{\rho_1 v_{l1}}{cos\theta_1} \qquad Z_{l2} = \frac{\rho_2 v_{l2}}{cos\theta_2} \qquad Z_{s2} = \frac{\rho_2 v_{s2}}{cos\gamma_2} \tag{4-9}$$

$$G_{l2} = \frac{1}{Z_{l2}} \qquad G_{s2} = \frac{1}{Z_{s2}} \tag{4-10}$$

where subscripts l and s refer to the longitudinal and shear waves, respectively. The energy conversion characteristics of the reflected and refracted waves are examined using computer simulation, and the value of the parameters used in this simulation are

$$\rho_1 = 1.00(g/cm^3) \qquad v_{l1} = 1.483(km/sec) \qquad v_{s1} = 0.000(km/sec)$$

$$\rho_2 = 8.51(g/cm^3) \qquad v_{l2} = 5.476(km/sec) \qquad v_{s2} = 3.302(km/sec)$$

The intensity of the normalized waves versus the incident angle, θ_1, are shown in Figure 4-5. In keeping with the previous constraints of θ_1 being less than approximately 3^o, the amount of energy transmitted into the medium is relatively constant in this interval. This can be assessed by observing the reflected energy, $(\varphi_1'/\varphi_1)^2$, in this interval. As can be seen from Figure 4-5c and d, changing the incident angle would only transfer the energy from one mode to the other. It is important to point out that the amount of transmitted shear wave is significantly smaller than the longitudinal wave over the angles of interest.

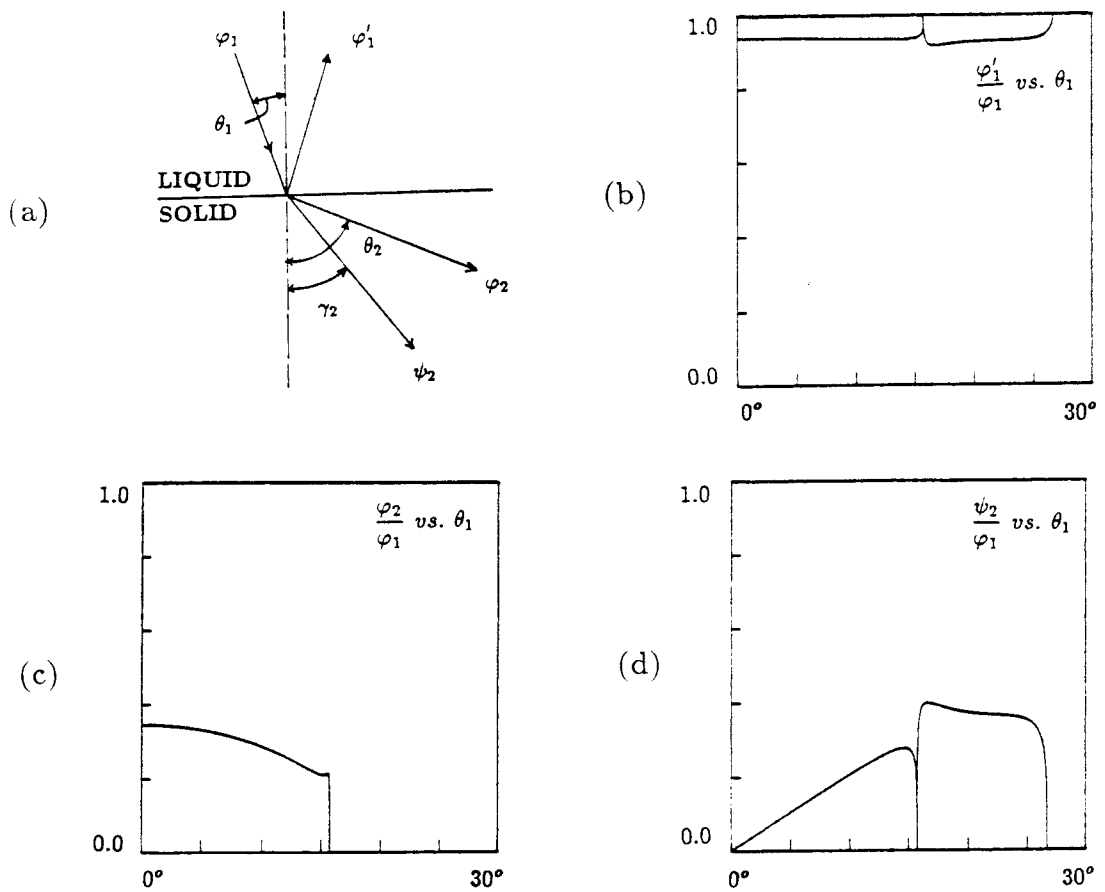

Figure 4-5. (a) A geometrical representation of refracted and reflected waves for case 1 where (b),(c) and (d) show the respective intensities of the refracted (φ_2, ψ_2) and reflected (φ_1') waves as a function of θ_1

The energy relationships between the transmitted and reflected waves with respect to the incident beam for case 2 are as follows:

$$(\frac{\varphi_2{}'}{\varphi_2})^2 = |\frac{Z_1 G_{l2} G_{s2} - G_{s2} cos^2 2\gamma_2 + G_{l2} sin^2 2\gamma_2}{Z_1 G_{l2} G_{s2} + G_{s2} cos^2 2\gamma_2 + G_{l2} sin^2 2\gamma_2}|^2 \qquad (4-11)$$

$$(\frac{\varphi_1}{\varphi_2})^2 = \frac{Z_1 G_{l2}}{cos^4 2\gamma_2} |1 - \frac{\varphi_2{}'}{\varphi_2}|^2 \qquad (4-12)$$

$$(\frac{\psi_2{}'}{\varphi_2})^2 = (\frac{v_{s2}}{v_{l2}})^4 \frac{tan\theta_2 sin^2 2\theta_2}{tan\gamma_2 cos^2 2\gamma_2} |1 - \frac{\varphi_2{}'}{\varphi_2}|^2 \qquad (4-13)$$

The plot of the intensity of normalized waves against the range of incident angles, θ_1, is shown in Figure 4-6. Figure 4-6b reveals that in the transmitted energy, $(\varphi_1/\varphi_2)^2$, maximization occurs when the scanning angle is minimized. This minimization also results in making the longitudinal waves more dominant, and mode conversion becomes negligible at this interface.

The energy relationship between the transmitted and reflected waves and the incident wave for case 3 are:

$$(\frac{\psi_2{}'}{\psi_2})^2 = |\frac{Z_1 G_{l2} G_{s2} + G_{s2} cos^2 2\gamma_2 - G_{l2} sin^2 2\gamma_2}{Z_1 G_{l2} G_{s2} + G_{s2} cos^2 2\gamma_2 + G_{l2} sin^2 2\gamma_2}|^2 \qquad (4-14)$$

$$(\frac{\varphi_2{}'}{\psi_2})^2 = (\frac{v_{l2}}{v_{s2}})^4 \frac{tan\gamma_2 cos^2 2\gamma_2}{tan\theta_2 sin^2 2\theta_2} |1 - \frac{\psi_2{}'}{\psi_2}|^2 \qquad (4-15)$$

$$(\frac{\varphi_1}{\psi_2})^2 = \frac{\rho_1 tan\theta_1}{2\rho_2 sin2\gamma_2 sin^2\gamma_2} |1 - \frac{\psi_2{}'}{\psi_2}|^2 \qquad (4-16)$$

The above energy relationships versus the incident angle, θ_1, can be seen in Figure 4-7. Figure 4-7b indicates that the transmitted energy, $(\varphi_1/\psi_2)^2$ into the water gap will increase by increasing the incident angle. This will also result in increasing mode conversion.

In consolidating the results of the three previous paragraphs, it becomes apparent that minimization of the shear waves and mode conversion would be concurrent with the optimality criteria. This is supported by the fact that cases 1 and 2 are not efficient in producing shear waves. Furthermore, in comparing cases 2 and 3 as far as effectiveness in transmitting energy into the water gap, case 2

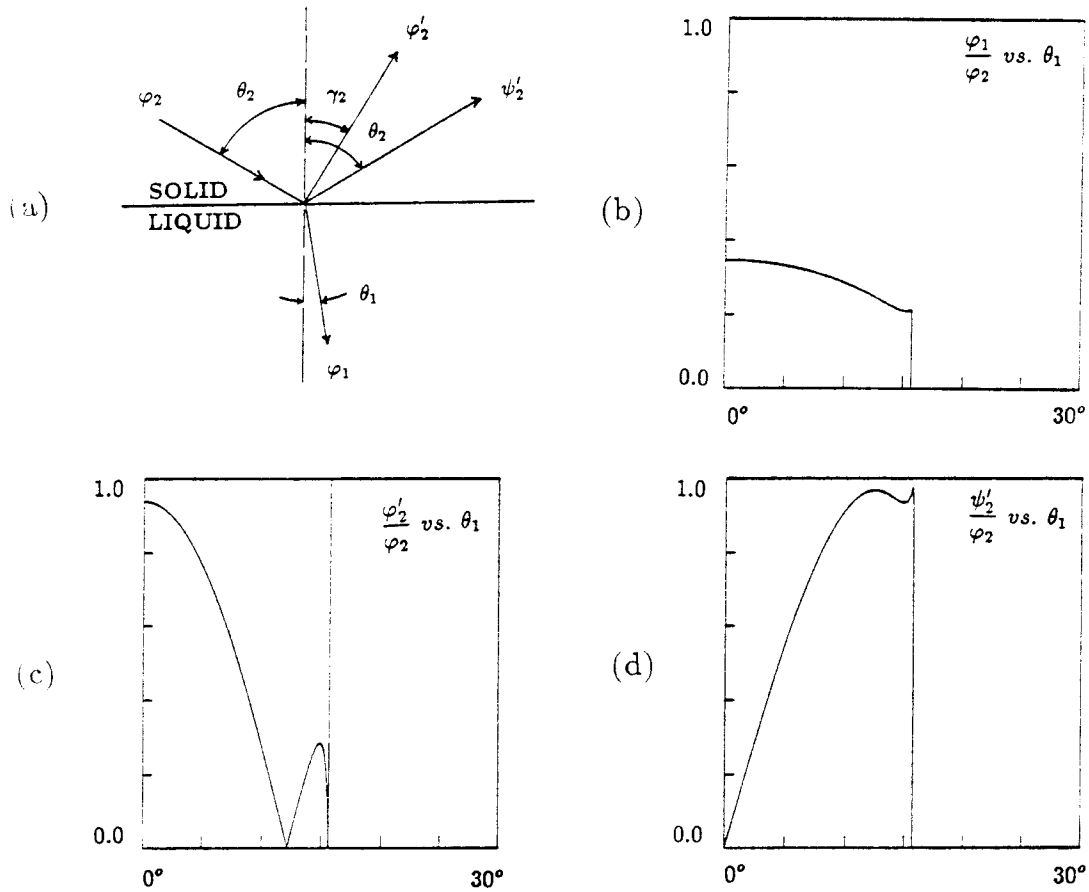

Figure 4-6. (a) A geometrical representation of refracted and reflected waves for case 2 where (b),(c) and (d) show the intensities of the refracted (φ_1) and reflected (φ_2', ψ_2') waves as a function of θ_1

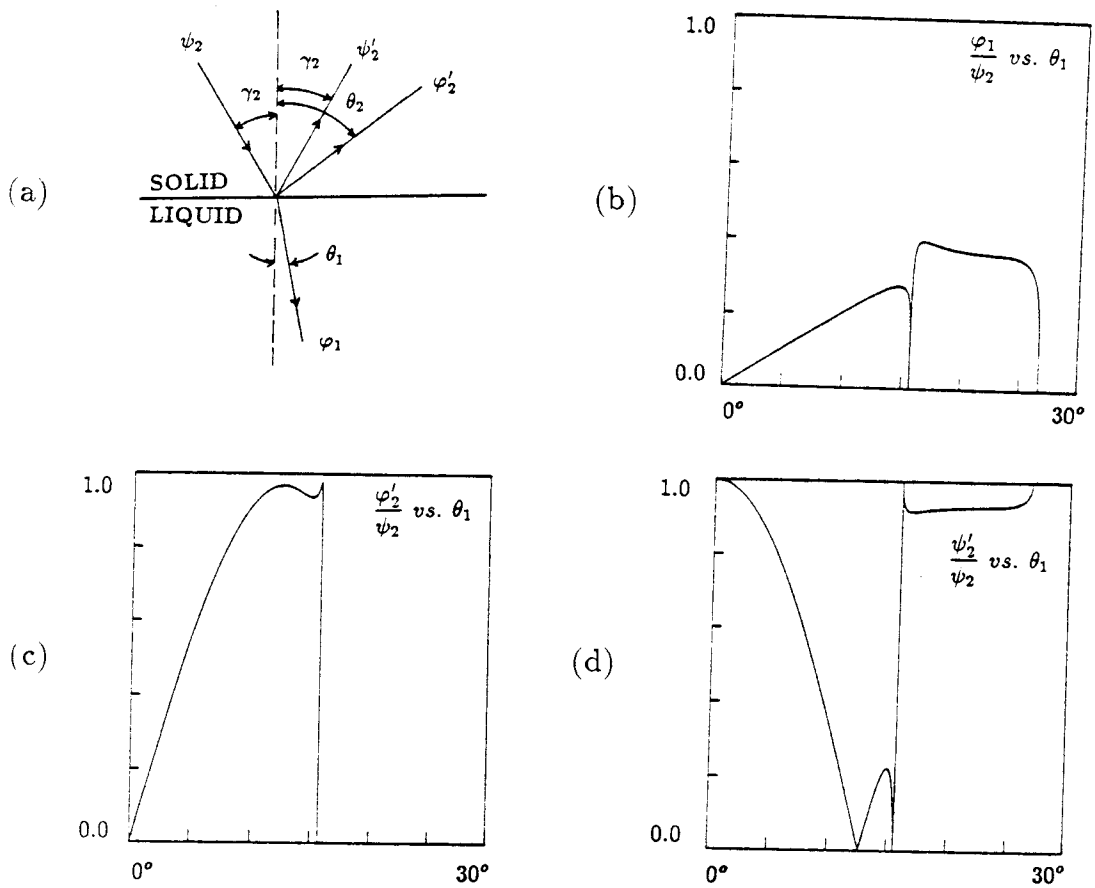

Figure 4-7. (a) A geometrical representation of refracted and reflected waves for case 3 where (b),(c) and (d) show the intensities of the refracted (φ_1) and reflected (φ_2', ψ_2') waves as a function of θ_1

transmits considerably more energy. Thus, the smallest scanning angle should be chosen in order to minimize the energy lost in mode conversion and to maximize the intensity of the 'b' echoes.

OAS Experimental Patterns

Oblique angle measurements were made using planar and tubular multilayered models. Within the permissable range of scanning angles given in Equation 4-5, experimental results have been found to be concurrent with theoretical predictions. Planar measurements were taken using several angles inside and outside the bounds described by Equation 4-5, showing how the characteristics of 'b' echoes are affected as a function of the incident angle. Similar results were observed using the tubular model. Both planar and tubular measurements demonstrated the effectiveness of OAS in recovering information from the target hidden by a highly reverberant thin layer.

The setup for the planar OAS measurements is similar to that shown in Figure 4-1. The front layer thickness is 2 mm, a target distance of 5 cm, and the 3-dB beam field of the transducer used is approximately 6 mm. The constraints on the incident angle are $1.74^o \leq \theta_1 \leq 4.15^o$ where at least five reverberations are within the 3-dB beam field. The three measurements are shown in Figure 4-8, where the scanning angles are 0.35^o,1.94^o, and 5.10^o. In Figure 4-8a, class 'a' echoes are interfering with 'b' echoes which makes direct evaluation difficult. As the angle is increased to 1.94^o (shown in Figure 4-8b), 'a' echoes are completely eliminated from the region of interest. The 'b' echoes are clearly visible bearing minimal distortion. If the angle is increased further to 5.1^o, then the 'b' echoes decrease in magnitude, as shown in Figure 4-8c, due to the lateral shifting of the echoes out of the detectable field of the transducer, as discussed earlier. In addition, spurious echoes are present due to the effect of mode conversion.

The tubular measurements using OAS are shown in Figure 4-9. These measurements follow the constraints calculated in the theoretical analysis, in which the scanning angle used was approximately 2^o. Figure 4-9a shows the results of the OAS of the tube structure without the support plate behind it, displaying

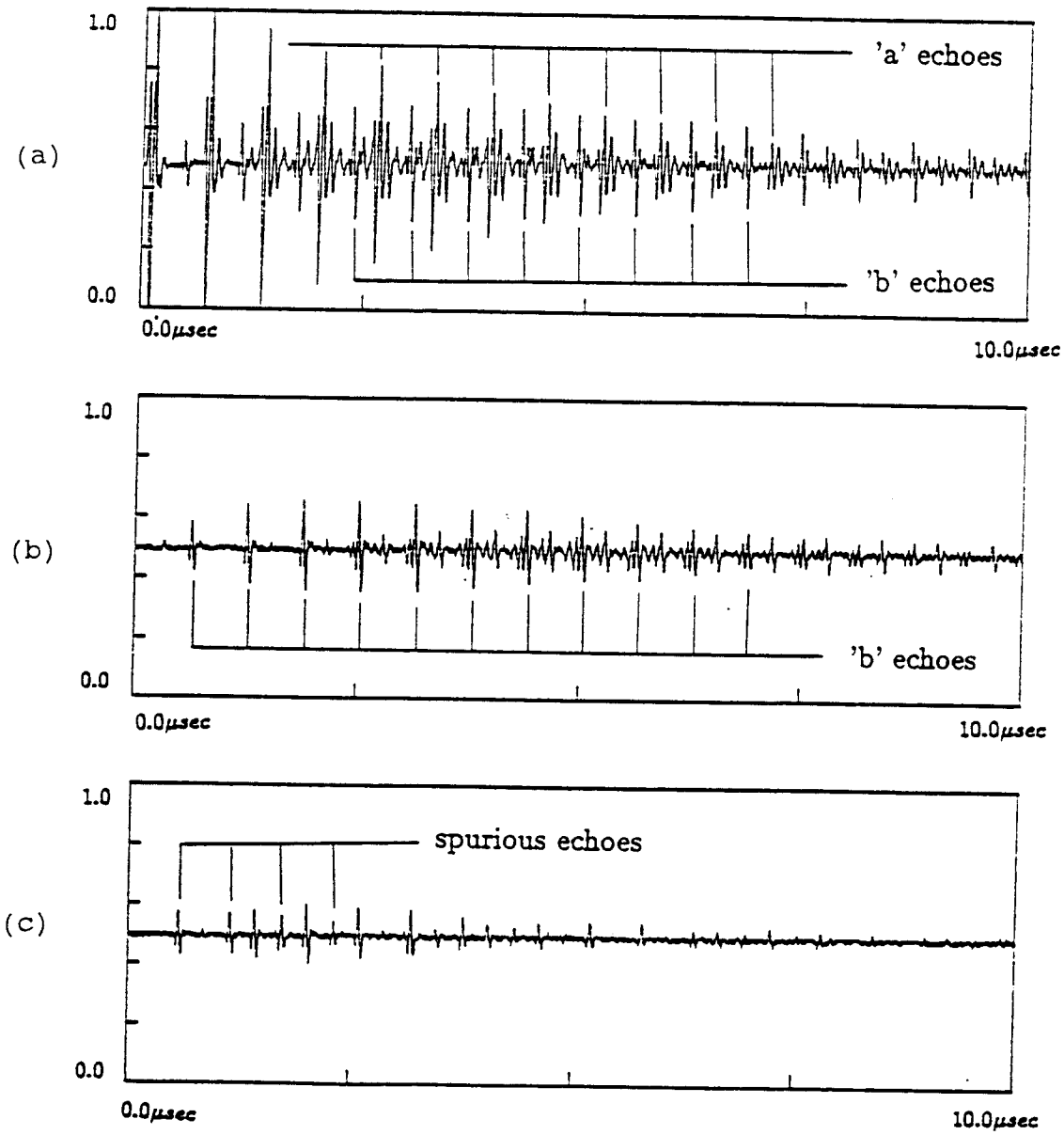

Figure 4-8. OAS experimental results from the planar model, where in (a) $\theta_1 = .35^o$; (b) $\theta_1 = 1.94^o$; and (c) $\theta_1 = 5.1^o$

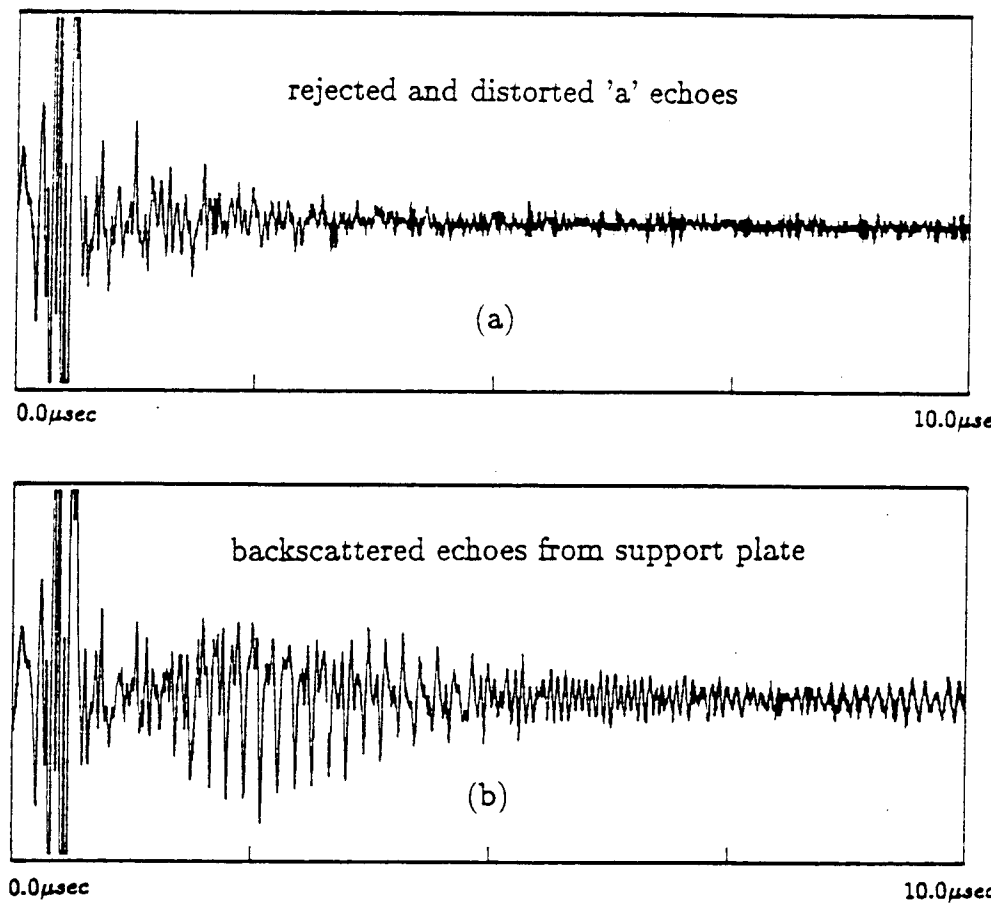

Figure 4-9. OAS experimental results from tubular models: (a) shows the A-scan of the tube wall, and (b) shows the A-scan of the tube wall with the support plate behind it

only 'a' echoes. The rejection of 'a' echoes is evident, although more noise is observed because the measurements are taken in an enclosed space and all the reverberant echoes are trapped within the structure. Figure 4-9b shows the OAS of the tube/support plate, in which the 'b' echoes are clearly visible and resolvable. These results can be beneficial in characterizing the support plate integrity . It is important to mention that the oblique angle scanning scheme performs well for the case where the target is orientated in such a manner to reflect a sufficient amount of energy towards the transducer [Kup82]. In general, OAS can be employed in examining multilayered structures where cracks or flaws are present and normal incident scanning proves ineffective.

CHAPTER V

ECHO CANCELLATION TECHNIQUES

Introduction

As shown in the previous chapter, the elimination of the 'a' echoes will improve the visibilty of the 'b' echoes significantly. Cancellation of 'a' echoes by means of signal processing techniques is more generally applicable than oblique angle scanning. This procedure involves obtaining a reference signal of a tube structure which is comprised of only 'a' echoes and subtracting it from the measured tube/suppport plate signal containing both 'a' and 'b' echoes. The effectiveness of this method depends primarily on how well the 'a' echoes of the reference signal are "matched" to those in the measured signal. Matching of the 'a' echoes is in turn dependent on how similar the measurement systems and targets are to one another. The implementation of echo cancellation can be done in the analog or digital domain in which each implementation has different echo matching capabilities. This chapter contains the analysis and physical considerations of the implementation of echo cancellation, analog and digital, and corresponding experimental performances.

Analog Echo Cancellation

The basic measurement system introduced in Chapter 3 has several parameters that can be adjusted to improve the matching characteristics of the analog echo cancellation system. The stages of the measurement system are shown in Figure 5-1 with an associated transfer function assigned to each stage. To implement analog echo cancellation, two very similar measuring systems are needed, one to produce the reference signal and the other to obtain the tube/support plate signal. The differences in the measurement systems can be compensated for using various controls involving the generation of the transmitted echo, synchronization of the

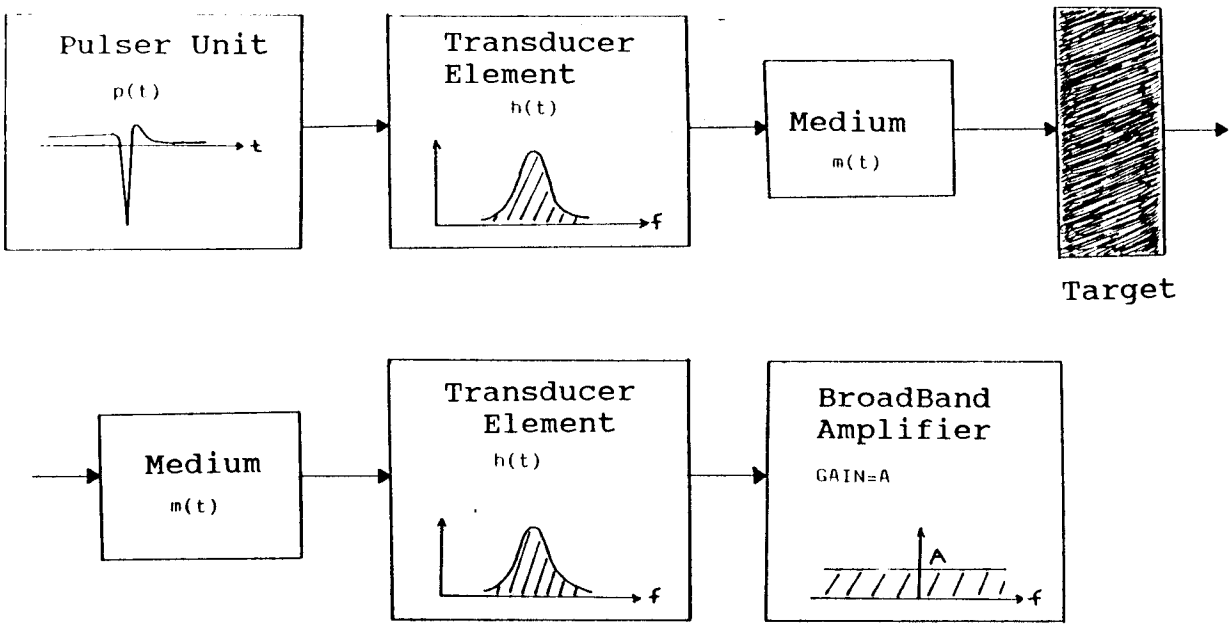

Figure 5-1. Stages associated with the ultrasonic data acquisition system

two signals. and appropriate matching of the gain of each system. The subtraction of the two signals will be optimized in a least mean squares (LMS) sense where the output energy of the signal will be minimized.

The initial pulser unit has a dampening control to determine the intensity and duration of the pulse that excites the piezioelectric element of the transducer. To see the effect of this on the generated echo, Figure 5-2 shows the generated echo and its spectral components for various degrees of dampening. As more dampening is applied, the more narrowband the echo becomes and therefore loses resolution. In addition the energy transmitted into the medium is much lower and will result in poor signal-to-noise ratio. The dampening is needed to prevent transducer overexcitation which results in a prolonged echo with many lower frequencies associated with it known as "ringing". Ringing in the signal will interfere with the resolving of primary echoes especially in a highly reverberant environment. In most instances, Trace 6 demonstrates optimal dampening producing an echo with minimal ringing. This dampening control can compensate for different pulser units and improve matching of the two piezioelectric elements.

The sychronization of the two signals can be accomplished by triggering both devices from the same source, except allowing for an adjustable delay on the reference signal. This adjustable delay will be determined by the minimization of the power of the subtracted result. The control system must be very sensitive since the subtraction of high frequencies signals out of phase will produce large errors. Other problems with the synchronization of 'a' echoes is that the distance between reverberent echoes may differ due to unequal tube thicknesses of the targets. One solution is to use a reference tube with slowly changing tube thickness to improve matching in the signal parameters. Thus, optimization would now have to occur in two dimensions, which will complicate the procedure tremendously.

Another dimension to echo matching is the gain of the two broadband amplifiers at the output of the measuring system of Figure 5-1. The optimization of the gain of the two systems is accomplished by matching the largest peaks of both signals. The complete optimization procedure of the entire system is shown in Figure 5-3. The dashed lines represent control features of this system.

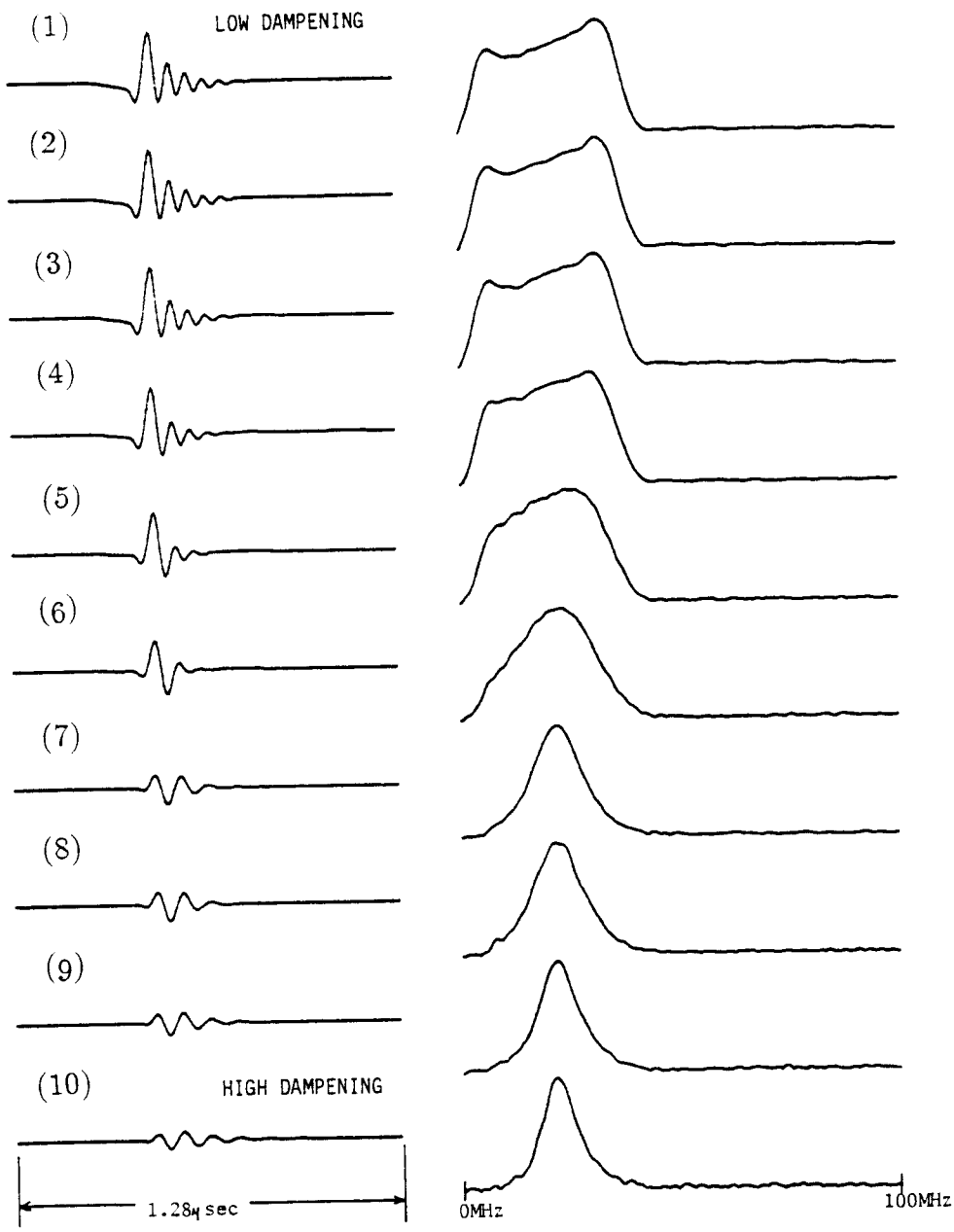

Figure 5-2. Various generated echoes and corresponding magnitude spectrum for different degrees of dampening

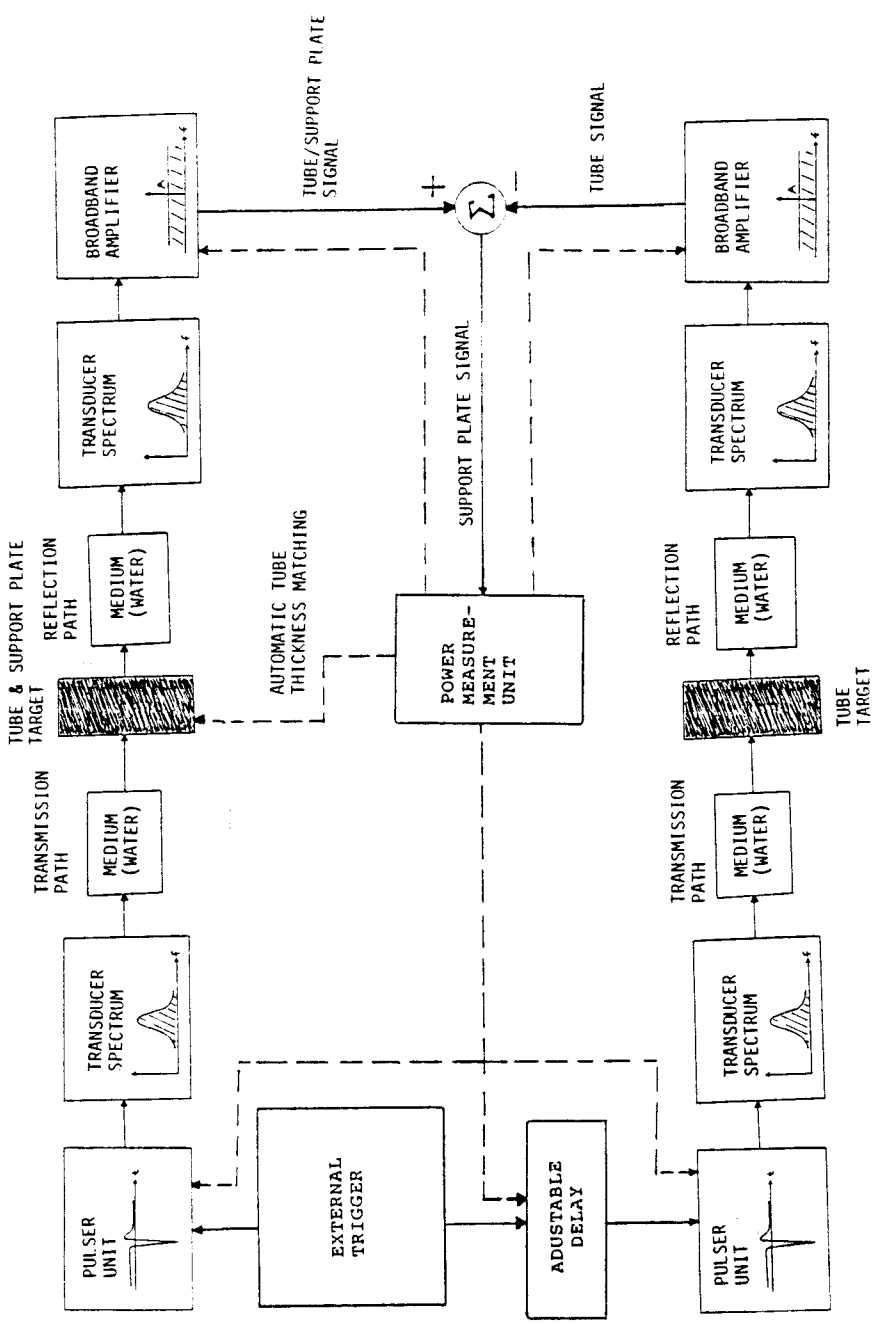

Figure 5-3. Analog Echo Cancellation System (dashed lines represent control parameters)

The physical realization of this automatic control system is not included in this report due to the complexity of the problem itself, although to determine the effectiveness of this system, the control parameters were adjusted manually. The experimental results for the cancellation of two isolated measurements of single echoes can be seen in Figure 5-4. The two measurements of Figure 5-4a and b were taken using two identical pulser units (Panametric 5052 PR) and two very similar 5MHz broadband transducers. The resulting cancellation shown in Figure 5-4c is 18dB down from the reference signal. This indicates that analog echo cancellation produces sufficient reduction with signals of very high frequencies. In the case of reverberant echoes, similar results can be seen in Figure 5-5, where Figure 5-5c shows conducsive echo cancellation performance, as in the previous illustration. These experimental results suggest that analog echo cancellation is a viable technique to improve the visibility of the 'b' echoes.

Digital Echo Cancellation

The digital implementation of the echo cancellation technique consists of a single measuring system, described earlier, in which the output signal is sampled using a high speed digitizer. Since only one measuring system is utilized, measurements are better matched than in the analog case. Also, this implementation allows for greater flexibility in terms of post-measurement processing techniques to improve cancellation. A problem inherent in digitizing the signal is the noise introduced in the cancellation signal caused by jitter in the digitized signals and quantization error.

Large errors can be expected from the subtraction of two sparsely sampled signals that are out of phase by small delays. This is the case for the present digitizer system, where the sampling rate is 200 MHz and the ultrasonic backscattered signals are centered approximately at 20 MHz, which corresponds to 10 samples per period. One can expect errors as large as 30% of the reference signal for this system. An example of this is shown in Figure 5-6, where (a) is a single echo with 10 samples per period, (b) is the same as (a) except delayed one-half the sampling period, and (c) is the resultant subtraction of (a) and (b). Thus, sychronization of

(a) single echo of pulser I

(b) inverted single echo of pulser II

(c) results of analog addition of the above signals

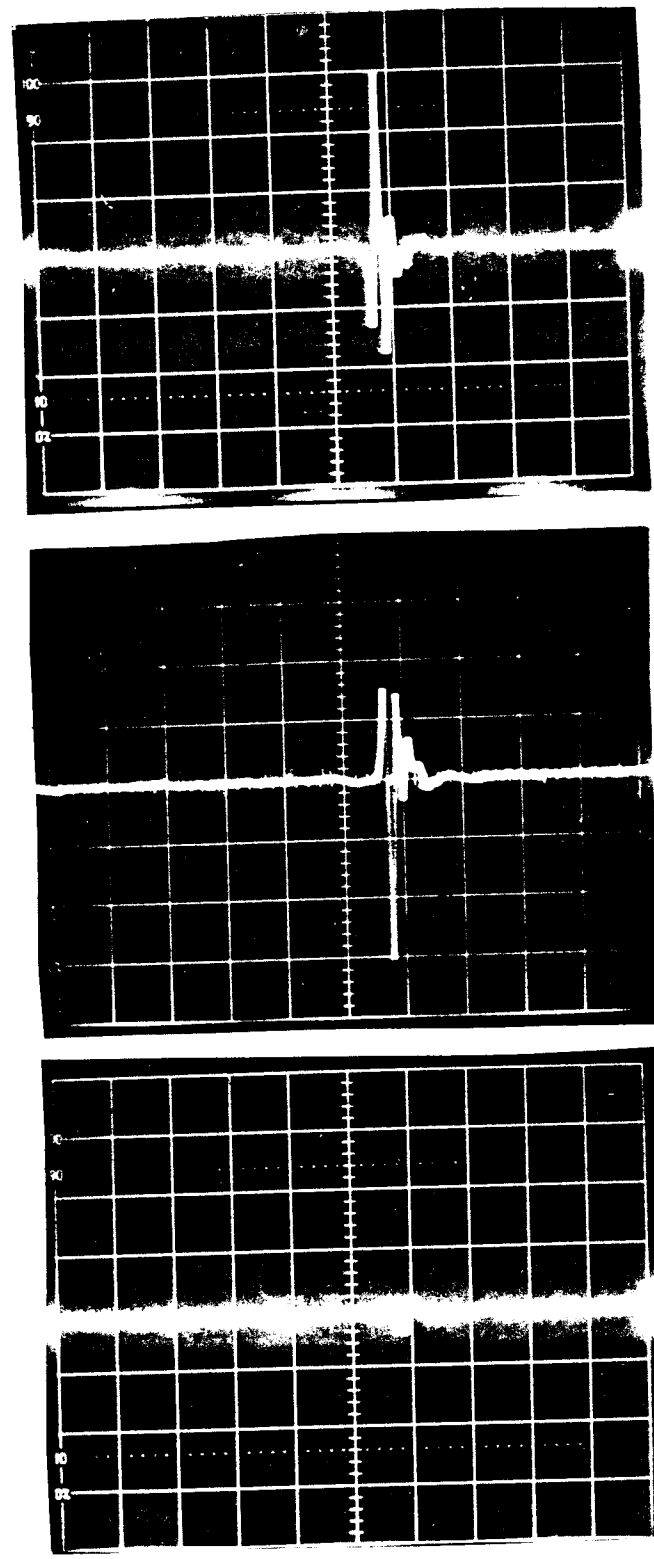

Figure 5-4. Analog cancellation of two separately generated single echoes

(a) signal generated by pulser I

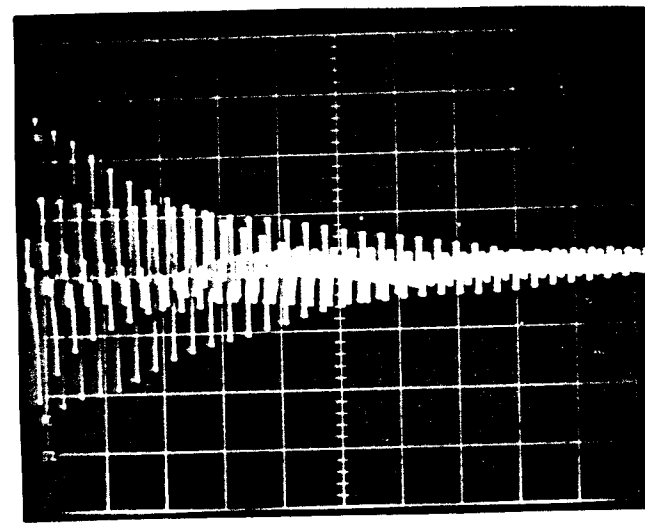

(b) inverted signal generated by pulser II

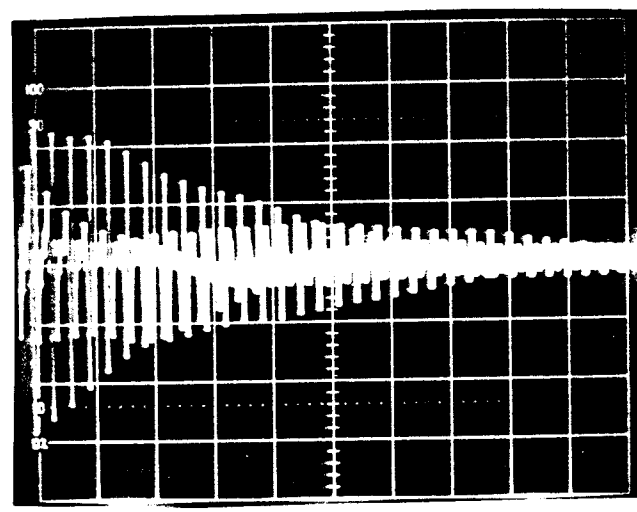

(c) results of analog addition of the above signals

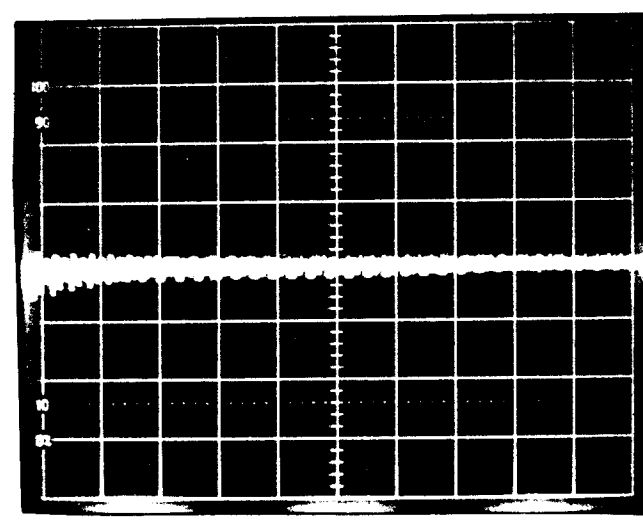

Figure 5-5. Analog cancellation of two thin layer measurements

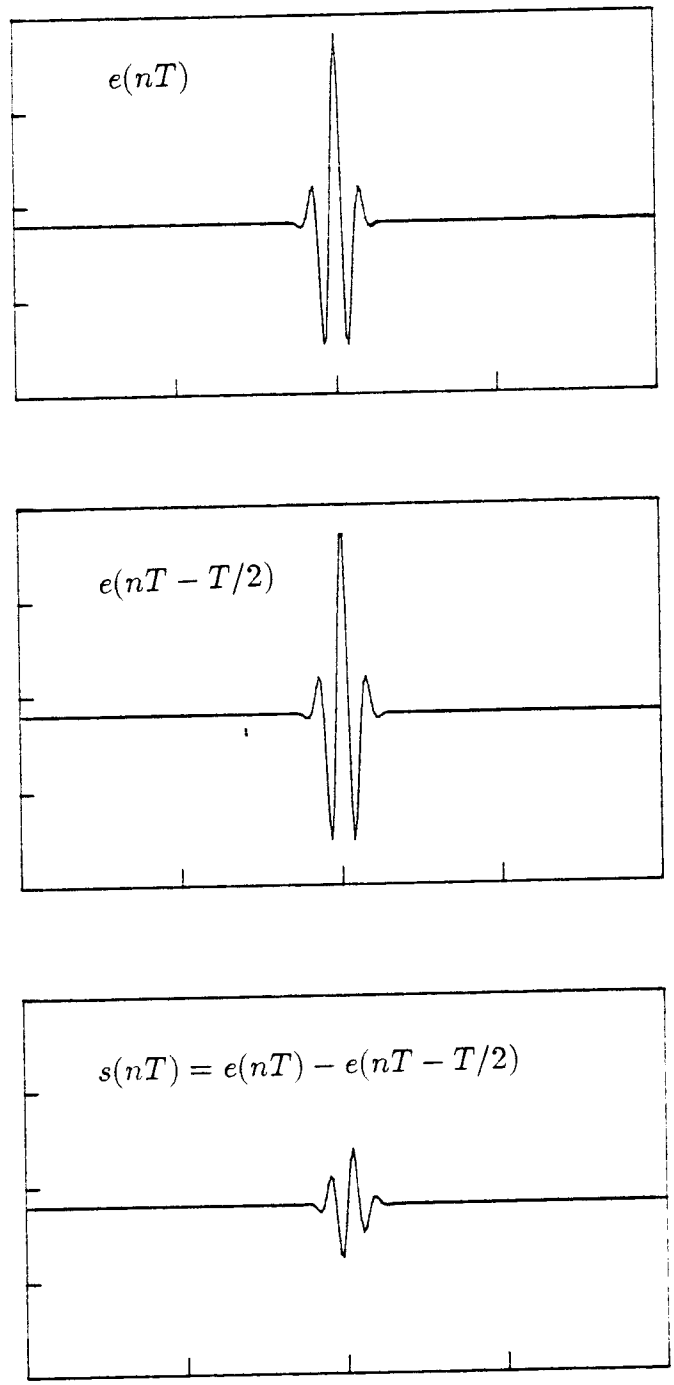

Figure 5-6. Digital subtraction of two digitized echoes (10 samples per period) separated by a time delay of one-half the sampling period.

the maximums of the two signals will not yield acceptable cancellation and further processing is required.

The synchronization of the two signals can be accomplished using time shift interpolation. The time shift, λ, is implemented by introducing a phase shift in the frequency domain given by:

$$s[(n-\lambda)T] = \frac{1}{N}\sum_{k=0}^{N-1} S(\frac{k}{NT})e^{j\frac{2\pi nk}{N}}e^{-j\frac{2\pi\lambda k}{N}} \qquad (5-1)$$

where T is the sampling period, N is the number of samples and $S(\frac{k}{NT})$ is the DFT of the signal, s(n). The time shift, λ, ranges from $-1/2$ to $1/2$. In order to synchronize the signals independently of each other, the signals are shifted such that the largest peak of the sampled signal is maximized in the interpolated signal.

To find the proper phase shift, a search procedure, shown in Figure 5-7, iteratively finds the relative maximum around a given sample point. In the first iteration, the signal is shifted an initial delay (usually $\lambda = 1/2$) in both directions, comparing the maximums and making the appropriate shift. The same procedure follows for the next iteration, except that the time shift used is one-half of the previous shift. This total time shift (phase shift) can be thought of as a summation of infinite series given by:

$$\lambda = \sum_{i=0}^{\infty}(\frac{1}{2})^i a_i \quad \text{where} \quad a_i = \begin{cases} 1 \text{ positive shift} \\ 0 \text{ no shift} \\ -1 \text{ negative shift} \end{cases} \qquad (5-2)$$

This series will always converge since the infinite series $\sum_{i=0}^{\infty}(1/2)^i$ converges, which is greater than or equal to the absolute value applied to each of the terms of the infinite series in Equation 5-2. Generally, a good estimate of the shift can be found in ten iterations. This will guarantee that the maximum peak is with 10^{-3} of the sampled point which will significantly reduce the error observed in Figure 5-6.

As for the problem of background noise, a method for reducing the digitized noise in the system is to perform coherent averaging. The procedure will replace

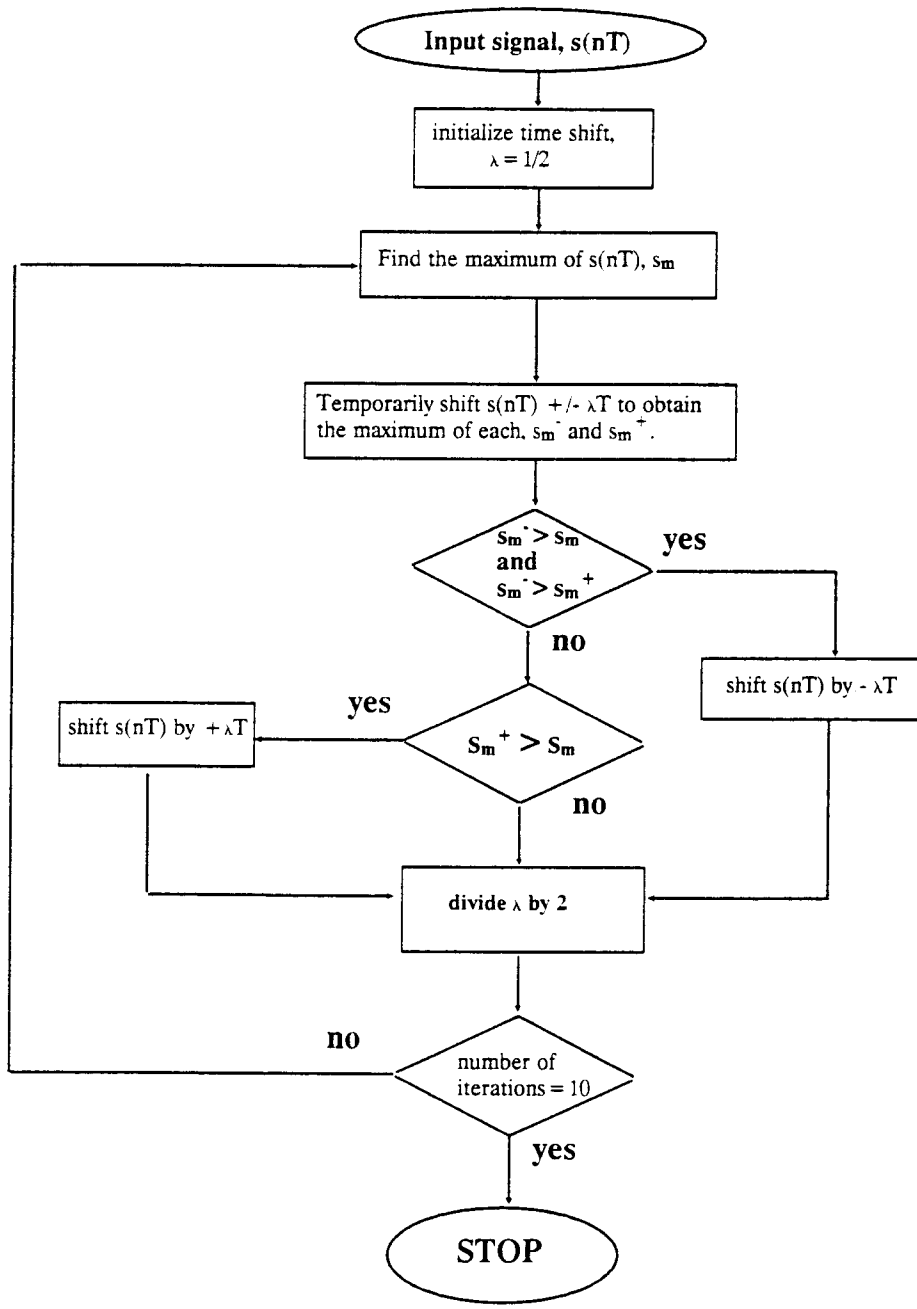

Figure 5-7. Time shift search algorithm

the noise by its expected value (a constant), assuming the process is stationary with respect to time. In our studies, the signals were averaged 256 times.

The cumulative effect of both these techniques on the cancellation signal is shown in Figure 5-8d, which is the cancellation of two different measurements of reverberant echoes shown in Figure 5-8a and b. In Figure 5-8c, the cancellation results from two signals that have not been interpolated but were averaged. These results show that the error signal is comparable to the analog results of the previous section. The resultant signal using interpolated and averaged signals given in Figure 5-8d shows that the error has been reduced to the point were it can be considered negligible.

For the case where the physical dimensions of the tube/support structure vary the 'a' echoes, the determination of a reference signal is more difficult. Creating an 'a' echo signal knowing the thickness of the tube wall would be the easiest method, except it would also require a priori knowlege of the impulse response of the system and also the reflective properties of the tube wall. Another alternative involves using a library of given reference signals of different tube thicknesses. This solution would require performing numerous subtraction results and accepting the one with the smallest error.

Experimental results shown in Figure 5-9 display echo cancellation of reference 'a' echoes with a tube/support plate measurement. The tube measurement came from the same tube in the tube/support plate structure. Thus, matching the physical parameters of the tube was not critical in this instance. The cancellation of the two signals is shown in Figure 5-9c, where the 'b' echoes envelope is clearly discernable although noise is still present, primarily due to the tubular geometry of the target.

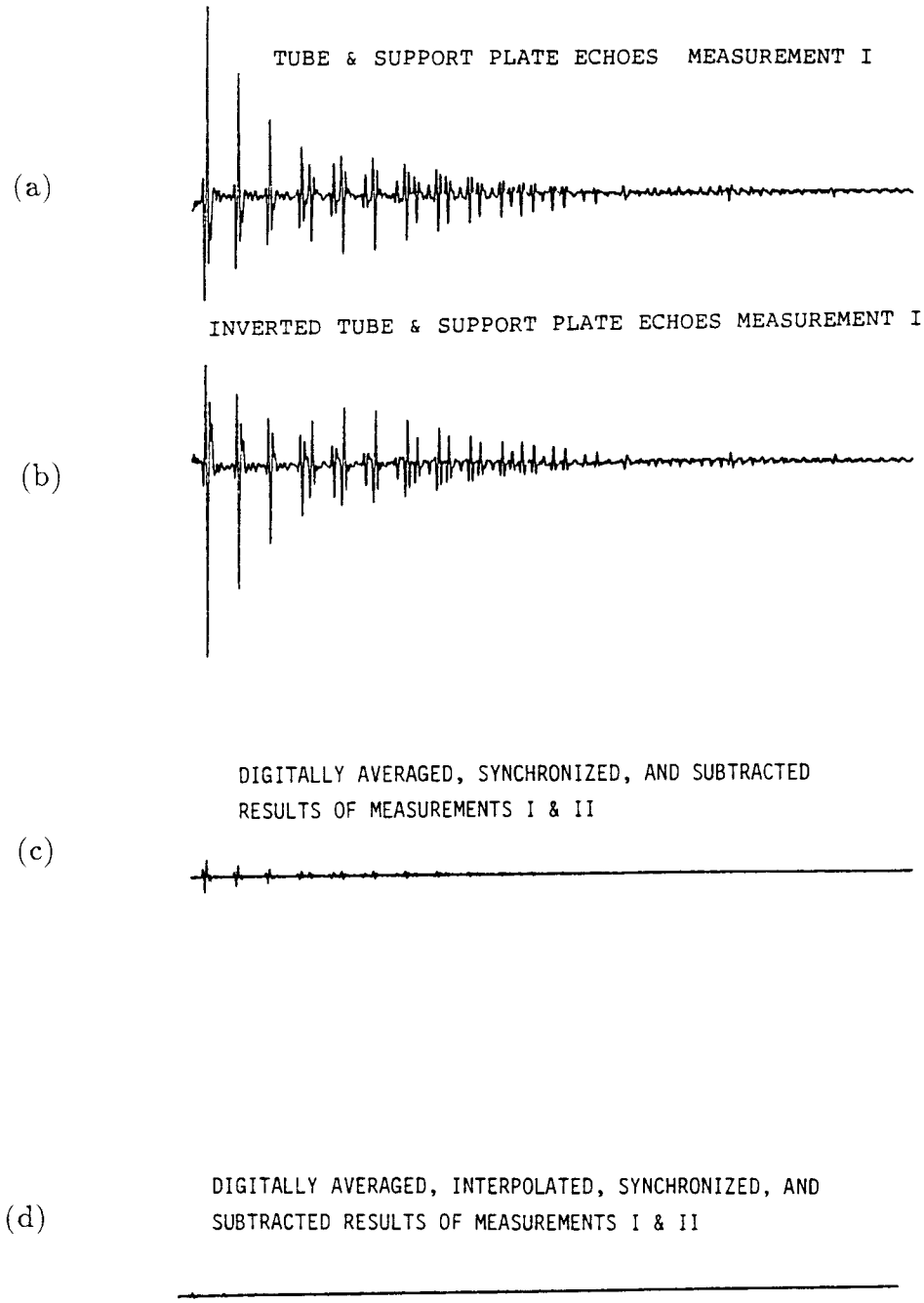

Figure 5-8. Digital echo cancellation of the two separate measurements of (a) and (b), where results are given in (c) in which no interpolation was applied and (d) in which interpolation was applied

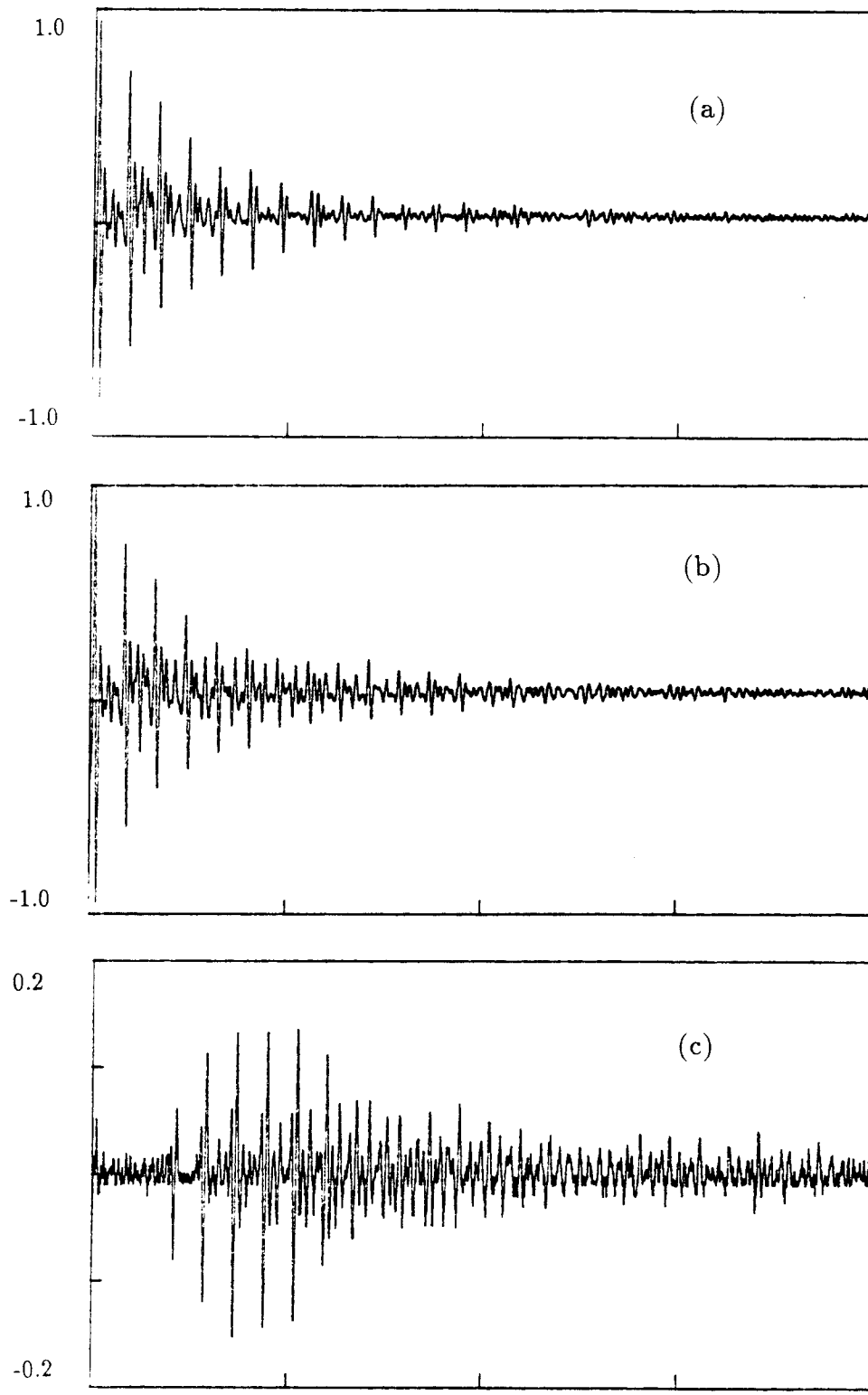

Figure 5-9. Digital echo cancellation of the tube measurement (a) and the the tube/support plate measurement (b) resulting in the support plate echoes (c)

CHAPTER VI

ANALYSIS AND CLASSIFICATION OF DETERIORATED SAMPLES

Introduction

The detection of corrosion and/or flaws in the tube/support structure of steam generators is essential in the prevention of tube wall denting. The detection process is difficult to generalize since many unique patterns may be observed in samples that reflect similar states of deterioration. The reflective boundaries of deteriorated samples usually scatter the incident wave in a random fashion. To characterize these samples, some known scenarios will help dictate patterns with different feature parameters and enable general classifications to be made. Since these scenarios are interrelated, the decision rule will be governed by some hierarchical structure to give priority to specific scenarios. This chapter contains a general overview of the corrosion problem and experimental results that illustrate different corrosion scenarios from which a classification procedure is derived.

Background

Corrosion of steam generator tube structures was discovered to be a problem in the early seventies, and much research has been done since then on the corrosion process itself [Eco84]. The basic equation for the chemical reaction is:

$$3Fe + 4H_2O \rightarrow Fe_3O_4 + 4H_2 \qquad (6-1)$$

where oxidation has occurred in the steel support structure. This process usually occurs in environments which contain a high concentration of acidic chloride.

The formed corrosion compound is about twice the volume of parent base metal. This type of corrosion is referred to as Nonprotective Magnetite (NPM). An example of this can be seen in Figure 6-1. This Figure shows the presence of a protective inner layer and nonprotective outer layer. The inner layer corresponds

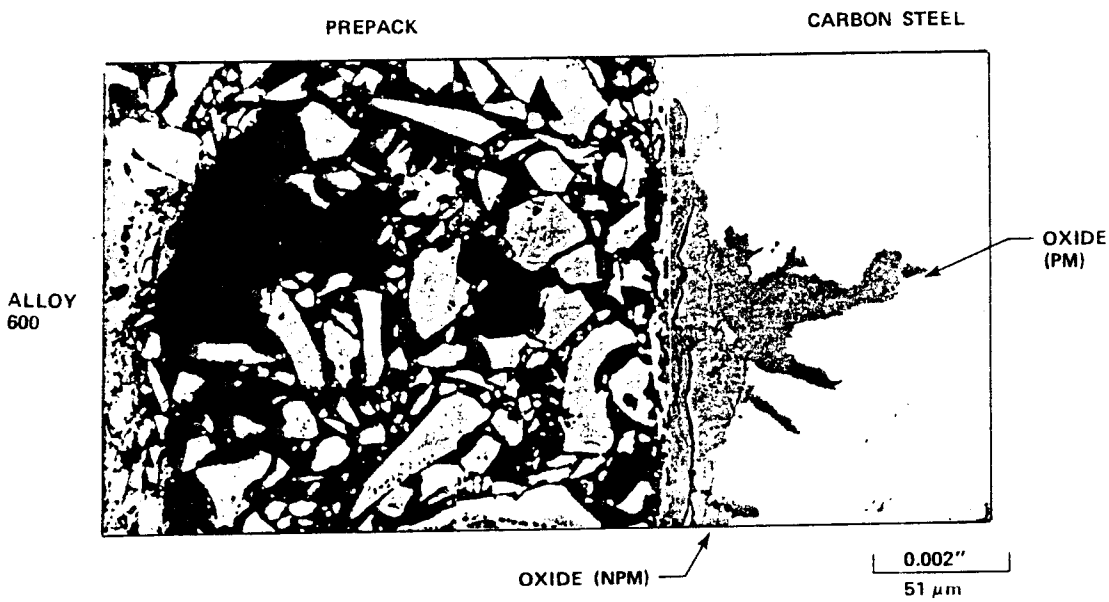

Figure 6-1. Example of corrosion present in the tube/support structure (taken from [deS84])

to Protective Magnetite (PM), which is composed of fine grain textured magnetite, and the outer layer of Nonprotective Magnetite is composed of very large grained magnetite. Protective magnetite has little effect on the tube/support structure, whereas nonprotective magnetite will fill the water gap and cause pressure on the tube wall if allowed to continue unchecked.

The nonprotective magnetite will fill the water gap, as illustrated in the micrographs of Figure 6-2, where Figure 6-2a shows the tube/support structure with large amounts of corrosion and Figure 6-2b shows the tube/support structure without significant corrosion build-up. The growth of corrosion has been found to increase with temperature and grow linearly during the fill in period of the water gap. After the water gap has been filled, the process proceeds much slower due to lack of accessibility of the oxidizing agents with the steel structure. Also, minerals in the water can be trapped or absorbed in the corrosion process, such as Ni, Na, Cl, Ti, Fe, and Si; thus, the composition of the NPM in the water gap may vary.

Some of the methods of controlling corrosion rely on additives to the water, purification of water, and/or removal of corroded tubes. With the use of additives, the corrosion process is either stopped before or after build-up has occurred. The method of inhibiting the reaction of Equation 6-1 is called nonvolatile treatment, in which oxdizing agents and choloric ions are neutralized. Such a treatment thus far has not been developed to effectively stop corrosion growth. The removal of corrosion also presents a problem since in most instances it results in erosion and fretting of the tube wall, giving rise to tube cracks or fractures. Also, purification of the input water is a typical method of preventing corrosion growth in which the detection of chemicals associated with corrosion (i.e. HCl, $CuCl_2$, $FeCl_2$, etc.) determines the purification procedure.

Since these protective methods are far from being perfected, the general procedure for detecting the presence of denting and corrosion is to use strain measurement and/or flow measurement devices which are sensitive to alterations in the tube structure. When detection occurs, the next step is the plugging of the corroded tube, making it inoperative and isolating it from the rest of the system. This testing procedure does not have the ablity to forewarn the user about the developement and the degree of corrosion, thus, further research is warranted.

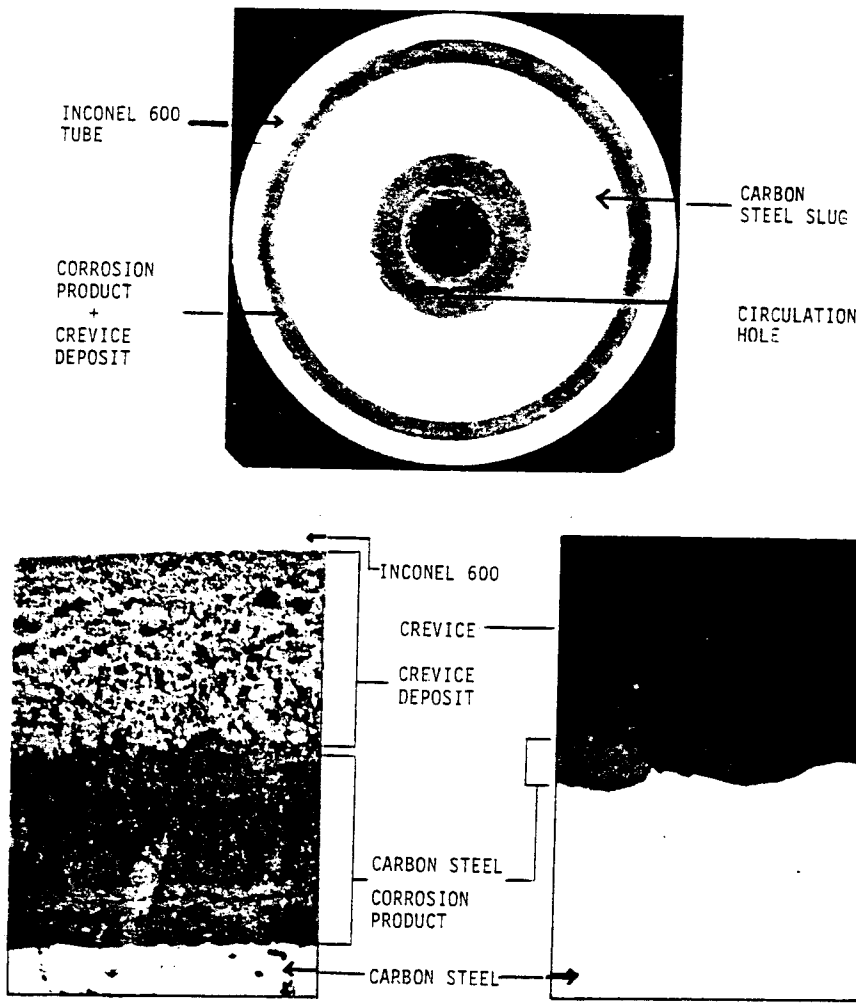

(a) (b)

Figure 6-2. (a) Tube/support structure exhibiting significant corrosion growth, and (b) is a tube/support structure with minimal corrosion growth (taken from [deS84])

Ultrasonic imaging as shown earlier has the capability of determining the status of water gap and support plate where corrosion growth emanates from. Although poor signal-to-noise ratio of the 'b' echoes will hamper this technique somewhat, the incorporation of earlier discussed processing techniques will give further opportunity to characterize the support plate echoes. From Figure 6-1, it can be seen that the corroded support plate is a rough uneven surface and one would expect a great deal of scattering in the backsacttered signal. The net result is a greatly attenuated support plate signal, which is good in the sense that it insures the detection of corrosion. The random nature of corrosion growth results in complicating the determination of gap size or corrosion growth. The next section shows experimental results that will characterize several corrosion scenarios and their effect on 'a' and 'b' echoes.

Experimental Results

The ultrasonic evaluation of the integrity of tube/support structures in the presence of inhomogenuities (i.e., corrosion and/or flaws) becomes very difficult and requires a high performance measuring system. For all data acquisitions presented in this section, a 20 MHz focused transducer with a 3-dB bandwidth of 10 MHz was used which provided resolution of about 20 microns (1 mil) in water. The resolution of the transducer cannot be increased without increasing the frequency, but in doing so, the energy of the backscattered signal will decrease significantly due to absorption and scattering caused by the granular characteristics of the material. Another important feature of this transducer is its focussing capabilities, since the tubular geometry of the target is a source of distortion as the traveling time of the echoes varies with position. Proper focussing decreases the spreading of the incident beam, and, consequently, limits the amount of distortion introduced to the signal. Thus, the resolution, focussing characteristics and sensitivity of the transducer do play a significant role in its performance as discussed in Chapter 3.

Several measurements were taken to display predictable experimental results corresponding to different deterioration scenarios of the tube/support structure. These scenarios are concerned with the detection of flaws within the tube wall or

corrosion growth stemming from the support plate. This structural deterioration will cause a reduction in the energy of the backscattered signal, although the effects on the class 'a' and class 'b' echoes differ with each scenario.

The deterioration of the tube wall in terms of flaws and erosion results in significant attenuation of the 'a' echoes caused by scattering. To illustrate the effect flaws have on the reverberant patterns, two tube samples have been altered by drilling a tapered notch in depths of 100 (5mils) and 200 (10mils) microns. The resulting backscattered signals can be seen in Figure 6-3. where the signal intensity suffers and, as expected, is dependent on the size of the notch. For the 100 micron notch shown in Figure 6-3b, the signal intensity drops 6 dB compared to the reference signal shown in Figure 6-3a, and in Figure 6-3c the 200 micron notch causes the signal to decay an additional 3 dB. This confirms the reliability of examining 'a' echoes to evaluate the overall condition of the tube wall in which inhomogenuities of relatively small size can be characterized. Thus, the evaluation of the tube wall can be obtained from a mapping of these patterns which provide information of location and depth of the dents or flaws.

To simulate the effects of tube erosion, the surface of a sample has been tapered as shown in Figure 6-4a. The smallest thickness of the tapered tube is 37.5 mils, which might be greater than would occur in general, but is done to emphasize its effect on the received signal. Results of the radial scanning of the tapered tube can be seen in Figure 6-4b, containing nine measurements referred to as Traces 1-9. In comparison to Trace 1 (the reference signal), Trace 2 reveals rejection of the signal similar to that seen in the oblique angle analysis where a majority of the backscattered signal is directed out of the detection field of the transducer. This creates another practical application of OAS in which the search for reflectors oriented at some angle can describe the degree of erosion present. Traces 3-5 show progressive improvements in the received signal since the outer surface of the tube wall becomes more parallel to the inner wall and, thus, a greater amount of energy is directed back towards the transducer. The reproducibility of these measurements can be seen in Traces 6-9, where little variations are discernable from the geometry of the opposing traces. Also, as the tube wall thickness reduces,

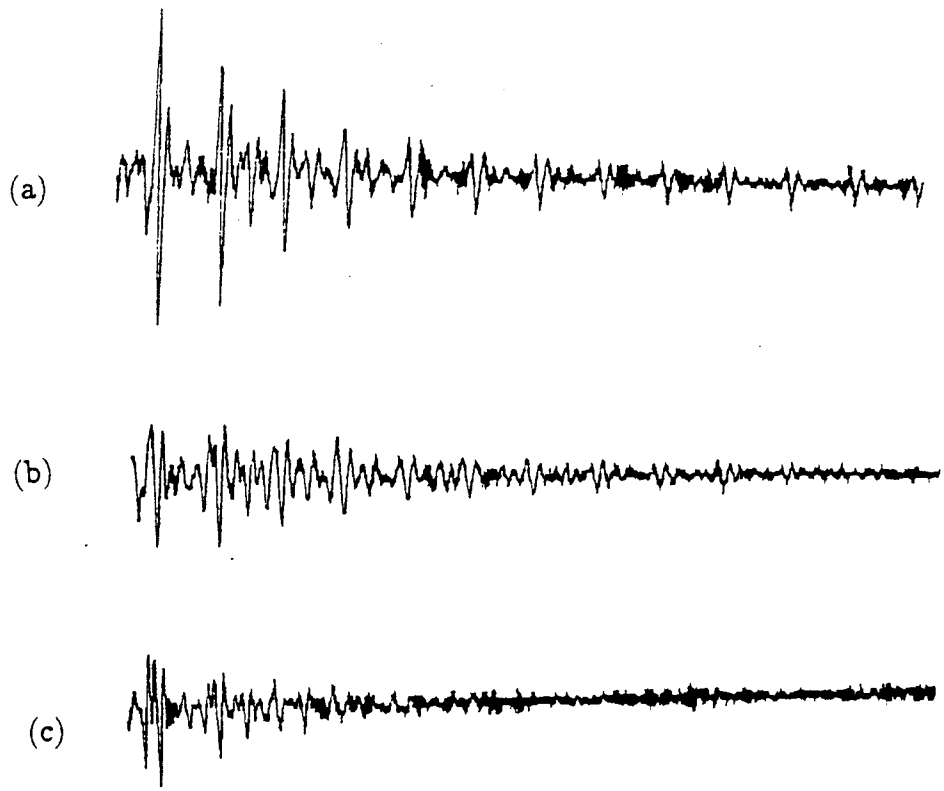

Figure 6-3. The reverberant patterns derived from tube samples with tapered dents, where (a) is the reference signal with no dent, and the the depth of the taper dent in the other signals is (b) 100 microns and (c) 200 microns

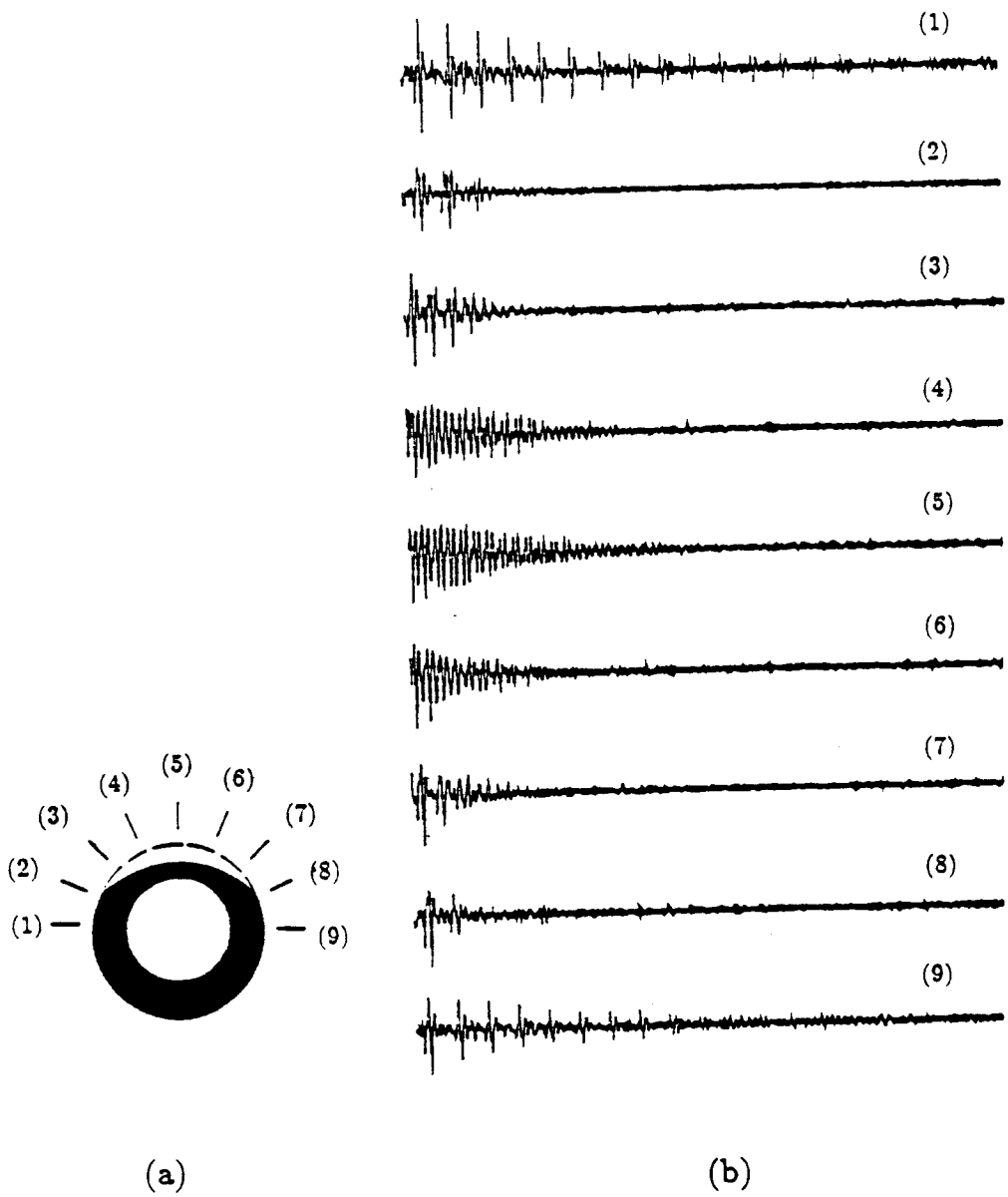

Figure 6-4. Tube erosion study, in which (a) is the schematic of the altered tube, and (b) Traces 1-9 are the radial scanned measurements of the eroded tube

the distance between 'a' echoes decreases, which is evident when comparing Traces 1 and 5.

In examining the corrosion growth stemming from the support plate, several deteriorated samples were examined which illustrate common patterns associated with different degrees of corrosion. The first sample corresponds to the case where corrosion is significant but has not completely filled the water gap between the tube wall and support plate. The radial scan of the sample can be seen in Figure 6-5, where each trace was taken at 45^o intervals. In all traces, the presence of 'b' echoes is practically nonexistent. This is expected due to the poor reflective properties of the support plate resulting from the presence of corrosion. Also, Traces 4 and 7 display signs of disruption in the tube wall since the 'a' echoes are less reverberant than in the other traces. This effect can be seen more clearly in later reverberations of the 'a' echoes since the decay of the reflection coefficient of the outer tube wall boundary, α_{32}, will attenuate the signal in an exponential fashion, as described in Equation 2-9. Thus, observations of later reverberations will be conducive for detecting significant deterioration in the 'a' and 'b' echoes due to corrosion growth.

In cases where severe corrosion growth affects the tube wall, several patterns can be anticipated. A high degree of corrosion alters the tube wall upon contact, which scatters and distorts both the 'a' and 'b' echoes. Figure 6-6 shows the radial scan of a corroded and dented sample where scattering effects are apparent in reverberation patterns. Slight resemblance to tube echoes can be seen from these figures, although the patterns are very sporadic and random in nature. Another possible effect of severe corrosion is displayed in Figure 6-7, where large pulses appear after some delay not corresponding to the expected reverberant patterns. This is a direct result of the corrosion diffusing into the tube wall. This alters the previous multilayered structure because that reverberation exists mainly between the inner surface of the tube wall and the support plate, although in Traces 3-5 it can be seen that diffusion is not complete and reverberations still exist within the tube wall as well. This diffusion information provides another scenario which must be taken into account in characterizing the tube/support structure.

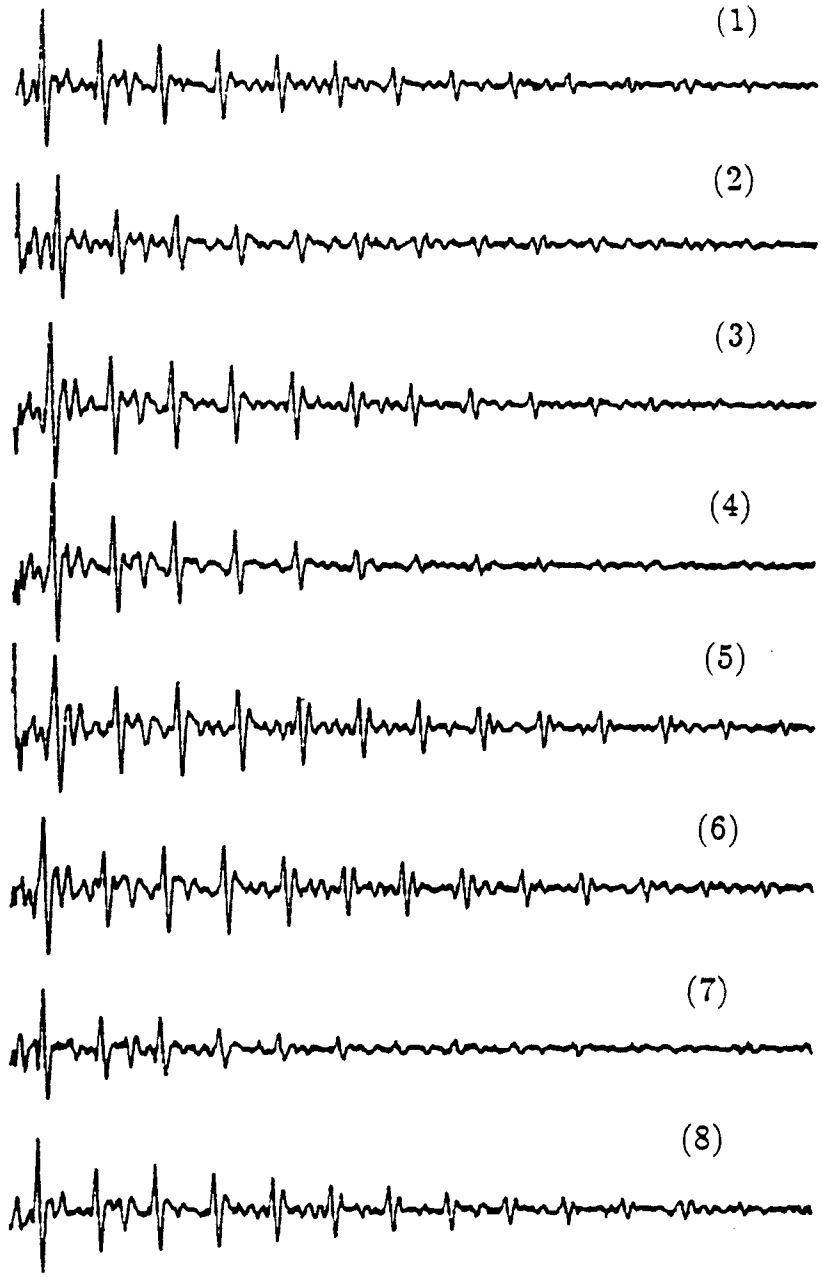

Figure 6-5. The A-scan of the corroded tube/support structure, where the radial measurements are shown in Traces 1-8

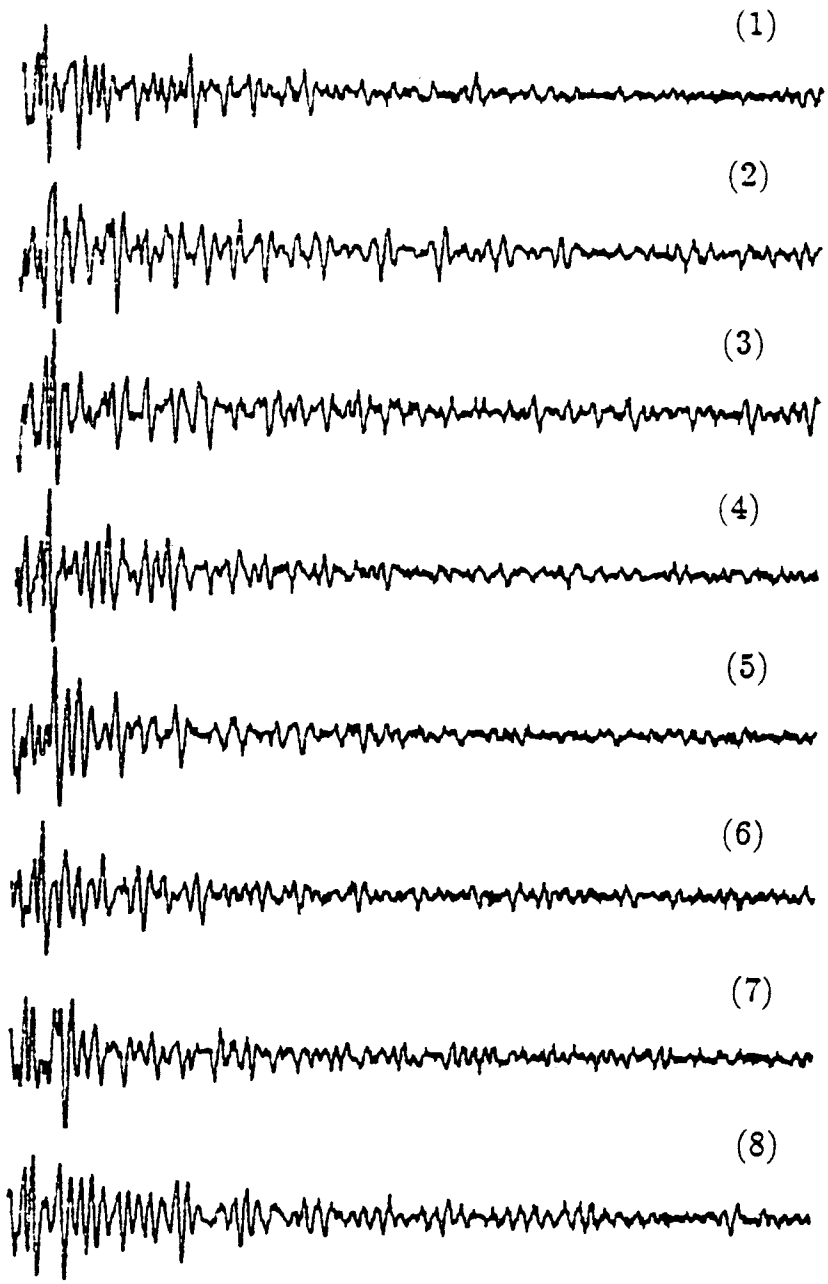

Figure 6-6. Reverberant patterns displaying severe corrosion characteristics of the tube/support structure

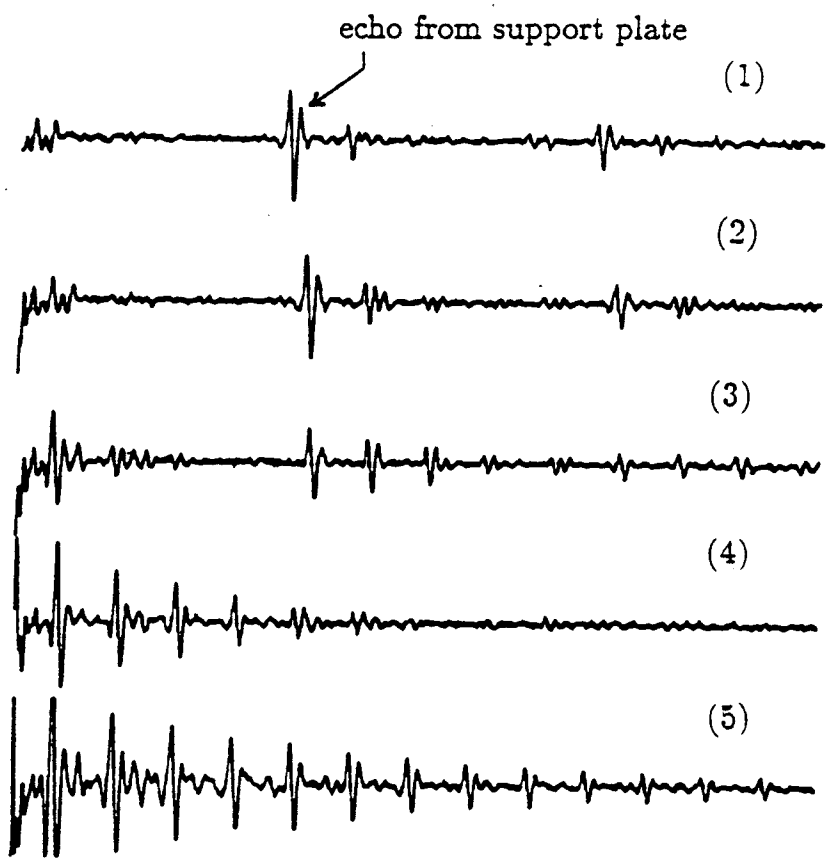

Figure 6-7. Reverberant patterns showing different scenarios which may be present in the case of severe corrosion

Hierarchical Classification of Tube/Support Structure

Classification of tube/support plate integrity is difficult to accomplish in a direct fashion because of the variations that exist from sample to sample. Also, all the types of decay presented previously can occur simultaneously; therefore a procedure to systematically check these alarm signs (features) is needed. Given the effect these scenarios can have on the 'a' and 'b' echoes and the sequence in which they occur, a hierarchical classification procedure was developed and is shown in Figure 6-8 in block diagram form. The methodology and classification procedure will be explained with each branch.

On initiation of this classification procedure, the presence of 'a' echoes is determined. The 'a' echoes determine the integrity of the tube wall which has the highest priority in terms of importance. Also, the presence of 'a' echoes is neccessary prerequisite before examining subsequent layers since it constitutes a propagation path to the support plate. The determination of this condition can easily be accomplished by observing the power over a segment of time shortly after the first large echo. This duration of this segment should last only a few reverberations, as shown Figure 6-9(a), since large echoes can appear later in reverberation sequence, as shown in the diffusion case. A threshold can be determined experimentally using unaltered tube samples. Since the intensity of the tube echoes are consistent for most measurements, the threshold can be set relatively high near 70% of reference. The failure of the threshold will indicate alterations in the tube wall; otherwise, more information concerning the tube wall is required for further evaluation.

The size of the tube wall will indicate the degree of erosion or wear within the tube wall and will also aid in further classification. Tube fracturing can also occur due to deficiencies within the tube itself , such as tube thinning or internal flaws due to erosion or corrosion within the tube wall. For this case, the 'a' echoes must be analyzed to determine the integrity of the tube wall, though the energy alone will not give a complete description of the status of the tube wall thinning in which the periodicity of the 'a' echoes must be examined. As stated in Chapter 2, the distance between the peaks of reverberant echoes describes the tube wall

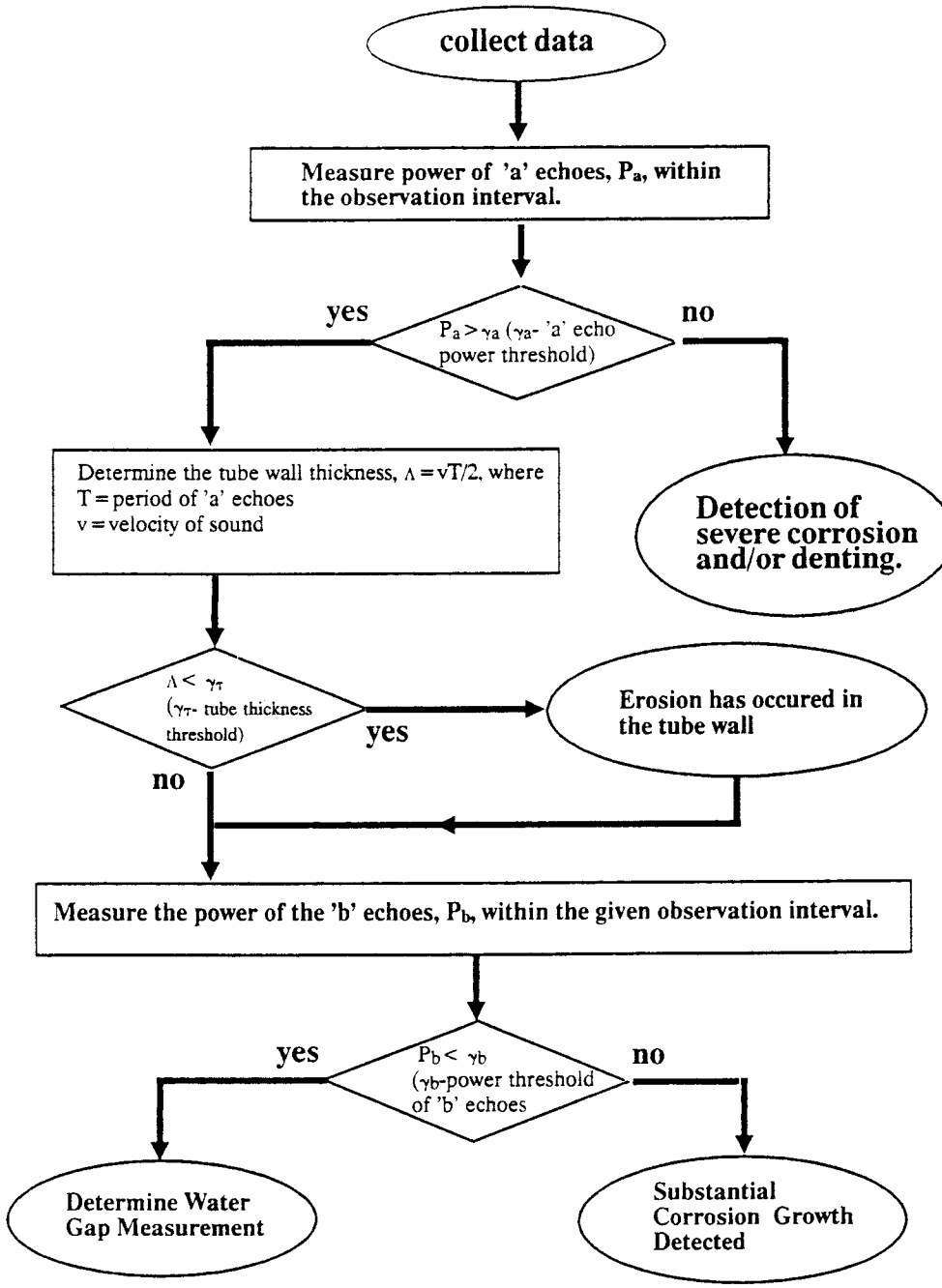

Figure 6-8. Block diagram outlining the general classification procedure for tube support structures

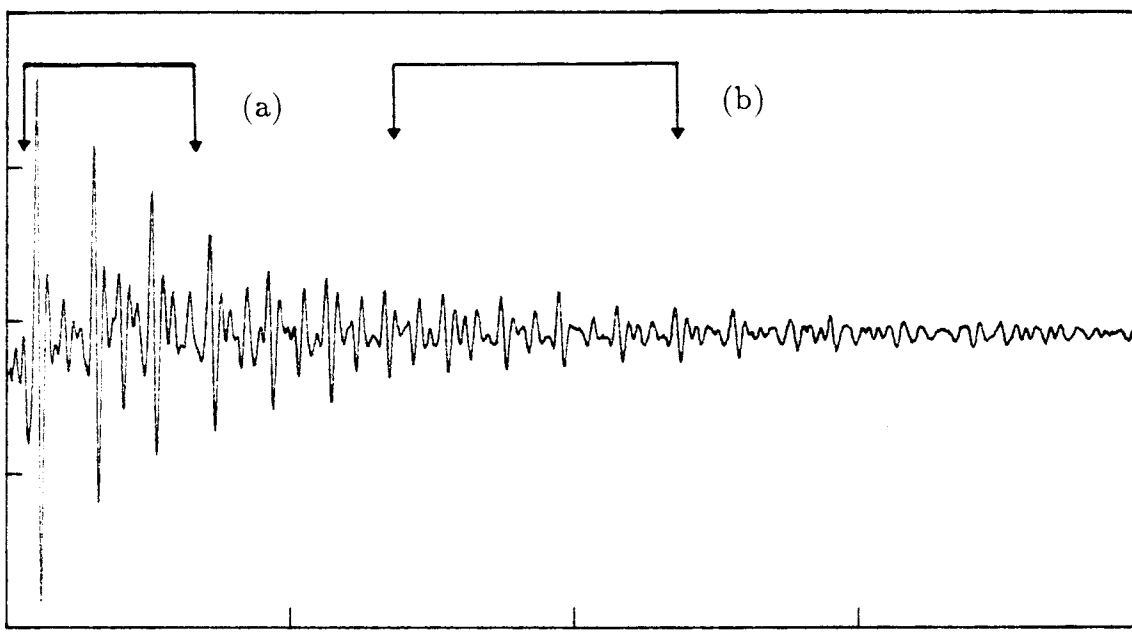

Figure 6-9. (a) Observation interval for the evaluation of tube echoes, and (b) is the observation interval for the evaluation of the support plate echoes

thickness. This can be accomplished using a peak detector combined with some delay device. Once a value for the tube thickness is determined. the region of inspection of the 'b' echoes can also be determined since the sufficient decay of the 'a' echoes can generally improve the visibility of the 'b' echoes.

In Chapter II, the eighth reverberation was calculated to give 'a' echoes which are comparable to the 'b' echoes. In addition, cancellation techniques introduced in Chapter 5 should be employed to simplify the classification procedure. The resulting examination of the power of a segment of about five reverberations in length (shown in Figure 6-9b) will provide sufficient information indicating the presence of support plate echoes. In this case, the threshold is more sensitive to environmental conditions and is best to determine experimentally through many similar samples. In lieu of insufficient power in the 'b' echo signal, oblique angle scanning may be employed as a viable technique for characterizing corrosion growth under these circumstances.

For the case where the 'b' echoes have adequate signal power, the power measurement is an effective and simple classification technique yet yields no information about the gap size. If the received power is significant enough, the reverberation number of the 'b' echo can be determined by the following relation:

$$\frac{b_{k+1}}{b_k} = (\frac{k+1}{k})\frac{a_{j+1}}{a_j} \qquad (6-2)$$

where a_k and b_k are the kth reverberations of 'a' and 'b' echoes, respectively, and k and j are any arbitrary reverberation numbers (note: i and j are not neccessarily equivalent). This is a simple manipulation of Equations 2-9 and 2-10 in which the amplitudes of these echoes are assumed to be attainable and will give an appropiate reverberation number,k, to the observed 'b' echo. The solution for k is:

$$k = \frac{a_{j+1}}{a_j}(\frac{b_{k+1}}{b_k} - \frac{a_{j+1}}{a_j})^{-1} \qquad (6-3)$$

From the given reverberation number of the 'a' echoes, j, and the above calculated reverberation number of the 'b' echoes, the gap distance, Δ, can be determined:

$$\Delta = \frac{v}{2}[(\tau_k - \tau_j) - (k-j)T] \qquad (6-4)$$

where τ_k and τ_j are the observation time of the corresponding reverberant echoes, T is the period of the 'a' echoes, and v is the velocity of sound in water. The problem with this method is that it assumes a high SNR and that the peaks of the 'b' echoes can be found. The peaks corresponding to the 'b' echoes usually can not be discerned in a corroded environment due to the scattering characteristics of corrosion. The only alternative in characterizing these environments in more detail is to use some type of statistical pattern recognition techniques, which would require a large number of corroded samples in order to describe the random parameters of the system.

CHAPTER VII

CONCLUSIONS

In the analysis of ultrasonic imaging of multilayered reverberant targets, the classification of the reverberant echoes is essential in the characterization of the tube/support structure. To improve the visibility of these classes of echoes several techniques were analyzed such as focussing, oblique angle scanning, and echo cancellation (analog or digital). These techniques make ultrasonic imaging of the tube/support an effective technique for corrosion characterization. This chapter includes disccusion of the optimal usage of each technique and possible improvements that can be made upon them.

The use of proper focussing of the ultrasonic beam provides the neccesary regional characterization and provides the added feature of signal-to-noise ratio enhancement. Since the target is tubular in nature, focussing will reduce the distortion present in the backscattered plane wave. Also focussing increases the energy penetrating into the target allowing for larger reverberatons in the received signal. Several focussing mechanisms were presented, although only the plane reflector was practical in our present research. The characteristics of the other reflectors have unique focussing properties (i.e. aperature, focal length, etc.), which may be exploited in further research.

Oblique angle scanning provides the automatic rejection of the 'a' echoes thus improving the visibilty of the backscattered signal from the support plate. The cancellation of the 'a' echoes using OAS at small angles is very effective and makes it a more viable imaging technique. The reflections of the support plate will infer discountinuities in the support plate which can correspond to flaws or corrosion growth in the structure.

Echo cancellation is another method of decomposing the 'a' and 'b' echoes that can be implemented using either digital or analog signals. The digital echo cancellation scheme provides great flexibility at the expense of time and involved equipment. Though through adaptive filtering techniques, the cancellation system

can be made to adjust for varying measurement environments, such as uneven tube wall thicknesses. The convergence of these algorithms can be very slow and impractical in many instances, thus improvements are needed in this area.

The analog echo cancellation scheme was demonstrated effective in limited experimental results. The optimization of the matching of the reference signal with the 'a' echoes of the measured signal is difficult since several parameters are involved. The echo cancellation scheme if optimized is more generally applicable than oblique angle scanning and more reliable.

A part of characterization of the integrity of the tube/support structure is the ability to determine different degrees of corrrosion from the deteriorated 'a' and/or 'b' echoes. This would require the development of an archive of corrosion signatures which can be used in classifying the different scattering charcteristics of the corroded samples. This mapping of scattering characteristics falls under the catagory of feature extraction. The implementation of pattern recognition techniques requires a large spectrum of samples to accurately classify the different degrees of deterioration in the tube/support structure which is presently unavailable.

BIBLIOGRAPHY

[Bre80] L.M. Brekhovskikh, *Waves in Layered Media*, Translated and Edited by T. Beyer, Academic Press, New York, NY (1980).

[Cha80] H.H. Chaakelis and A.V. Clark, "Ultrasonic Nondestructive Bond Evaluation: An Analysis of the Problem," *Materials Evaluation*, Vol. 38, pp. 20-38 (1980).

[Dav78] T.J. Davis, "Multifrequency Eddy Current Inspection with Continuous Wave Methods," *Materials Evaluation*, Jan. (1980) pp. 62-68.

[deS84] S.G. deSilva, C.R. Wolfe, *Causes of Denting*, Vol. 3, Plant Chemistry Correlations, Final Report May 1984. EPRI NP-3275 Research Report Center, Electric Power Research Institute Palo Alto, CA.

[Eco84] G. Economy, C.R. Wolfe, *Causes of Denting*, Volume I, Summary Report May 1984. EPRI NP-3275, Research Report Center, Electric Power Research Institute, Palo Alto, CA.

[Ewi57] W.M. Ewing, W.S. Jardetzky, F. Press, *Elastic Waves in Layered Media*, McGraw Hill, New York, NY (1957).

[Jon83] J.A. Jones Applied Research Co., *Eddy-Current NDE for Intergranular Attack*, Final Report Febuary 1983. EPRI NP-2862, Research Report Center, Electric Power Research Institute, Palo Alto, CA.

[Kra75] J. Krautkramer, *Ultrasonic Testing of Materials*, Springer-Verlag, New York (1975).

[Kup82] D.S. Kupperman M.J. Caines, and A. Winieki, " Assessment of Ultrasonic NDE Methods for Ceramic Heat-Exchanger Tubes," *Materials Evaluation*, Vol. 40, pp. 774-782 (1982).

[Lee71] S. Lees, "Ultrasonic Measurement of Thin Layers," *IEEE Trans. Sonics and Ultrasonics*, Vol. SU-18, No. 2, pp. 81-88 (1971).

[Maz86] J.L. Izbicki, J. Ripoche, A. Nagl, H. Uberall, and K.B. Yoo, "Transient acoustic scattering from layers and plates," *Journal of the Acoustical Society of America*, Vol. 80, pp. 295-301 (1986).

[Ros74] J.L. Rose and P.A. Meyer, "Ultrasonic Signal Processing Concepts for Measuring the Thickness of Thin Layers," *Materials Evaluation*, Vol. 32, pp. 249-255 (1974).

[San81] J. Saniie, "Ultrasonic Signal Processing: System Identification and Parameter Estimation of Reverberant and Inhomogeneous Targets," Ph.D. Thesis, Purdue University (1981).

[San82] J. Saniie, E.S. Furgason, and V.L. Newhouse, "Ultrasonic Imaging Through Highly Reverberant Thin Layers-Theoretical Considerations," *Materials Evaluation*, Vol. 40, pp. 115-121 (1982).

[San84] J. Saniie, "Resolution and Visibility Enhancement of Ultrasonic Echoes Reflected from Hidden by Highly Reverberant Layers," *IEEE Utrasonics Proceedings*, pp. 903-907 (1984).

[San86] J. Saniie, "Advanced Ultrasonic Techniques for Steam Generator Tube In-Service Inspection," *Nondestructive Evaluation Program: Progress in 1986* Special Report July 1987. EPRI NP-4902-SR Research Report Center, Electric Power Research Institute Palo Alto, CA.

[San87] J.Saniie and D.T. Nagle, "On the Imaging of Tube/Support Structures of Power Plant Steam Generators," *Review of Progress in Quantitative NDE,* Eds: D.O. Thompson and D.E. Chimenti, Plemnum Press, Vol. 6a, pp. 519-525 (1987).

[Wel69] P.N.T. Wells, *Physical Principles of Ultrasonic Diagnosis*, Academic Press, New York, NY 1969.